Electronic Structure Modelling of Singlet Fission in Organic Photovoltaics

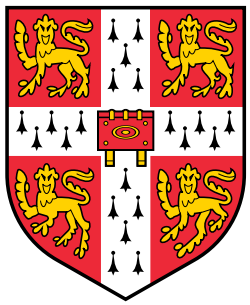

David Herbert Philipp Turban

Fitzwilliam College

University of Cambridge

This dissertation is submitted for the degree of

Doctor of Philosophy

November 2017

Electronic Structure Modelling of Singlet Fission in Organic Photovoltaics

David Herbert Philipp Turban

Singlet fission is a multiple-exciton-generation process found in organic materials that could help to enhance the efficiency of future photovoltaic devices, by overcoming the Shockley-Queisser limit. In spite of considerable experimental and theoretical attention, different aspects of the process are still not fully understood. The main reason for this is that singlet fission is characterised by a complex interplay of electronic states, vibrational modes and electrostatic screening effects.

In this thesis we employ *ab initio* electronic structure techniques to study the excitations involved in fission in molecular crystals and dimers, using the well-studied pentacene molecule as a reference system.

Linear-scaling density functional theory (LS-DFT) is used to model the influence of the crystal environment on charge-transfer (CT) configurations in the pentacene molecular crystal. We derive a general dipole correction scheme that allows us to eliminate finite-size effects from the calculations. We find that CT energies are significantly lowered by the response of the crystal environment, bringing them close to the energies of local excitations. This result lends support to the idea that the photoexcited precursor state to fission has significant CT character, and emphasises the role played by CT configurations in fission in the crystal.

Furthermore, we use DFT to parametrise a linear vibronic coupling Hamiltonian of a covalent dimer of pentacene, forming the basis for many-body quantum dynamics calculations of the interplay between electronic and vibrational degrees of freedom. This reveals an interesting role for symmetry in fission in such dimers. Due to their high symmetry, couplings that could enable fission are precluded at the ground-state geometry. However, dynamic symmetry breaking by vibrational modes opens up an efficient pathway for fission, via an avoided crossing mediated by virtual CT configurations.

Finally, we explore the influence of different side-groups and solvent environments on fission in pentacene dimers. To this end, we employ DFT with both implicit and explicit solvent models, combined with large-scale calculations to achieve sufficient sampling of solvent-solute configurations.

In memory of my mother

1949 – 2016

Preface

This dissertation is the result of my own work, and includes nothing which is the outcome of work done in collaboration except where specifically stated in the text. It has not, either in whole or in part, been submitted for another degree, diploma or any other qualification at this or any other university. This document does not exceed the 60,000 word limit prescribed by the Physics and Chemistry Degree Committee at the University of Cambridge.

David Herbert Philipp Turban
Cambridge, November 2017

Contents

Chapter 1

Introduction

In recent years, the field of organic electronics has attracted increasing interest from the scientific community, and has turned into a dynamic area of research that shows great promise for the future [1]. Organic materials have the potential to provide an alternative to traditional inorganic semiconductors for important applications such as photovoltaics (PVs), with the advantages of much reduced cost and less energy-intense production.

However, progress in this field is hampered by relatively poor theoretical understanding of electronic processes in organic materials. One reason for this is that the 'band' picture of weakly interacting electrons and holes, that is so successful for inorganic semiconductors, breaks down. Instead, electrons and holes in organics form tightly bound quasiparticles, called excitons. This is a consequence of the fact that organic materials have relatively small dielectric constants. In addition, disorder is much more prevalent due to the complex molecular structures encountered in organic materials, strongly affecting the dynamics and energetic alignment of excitons.

Organic solar cells have emerged as a potential alternative to the established silicon cells, promising much lower manufacturing cost and a lot more versatility with regards to form factor. The basic principle of operation of an organic solar cell is illustrated in Fig. 1.1. An electron donor material absorbs light, creating excitons. The excitons are electrostatically bound electron-hole pairs which diffuse through the material and can dissociate when they meet the donor-acceptor interface. In order for dissociation to be energetically favourable, the conduction band edge of the acceptor has to be lower than the conduction band edge of the donor. Dissociation creates free electron-hole pairs, building up a voltage across the device. A current disadvantage of organic PVs is their relatively low efficiencies compared to inorganics, of up to about 13% [2]. This is in part due to higher recombination resulting from stronger binding of electron-hole pairs, compared to inorganic semiconductors.

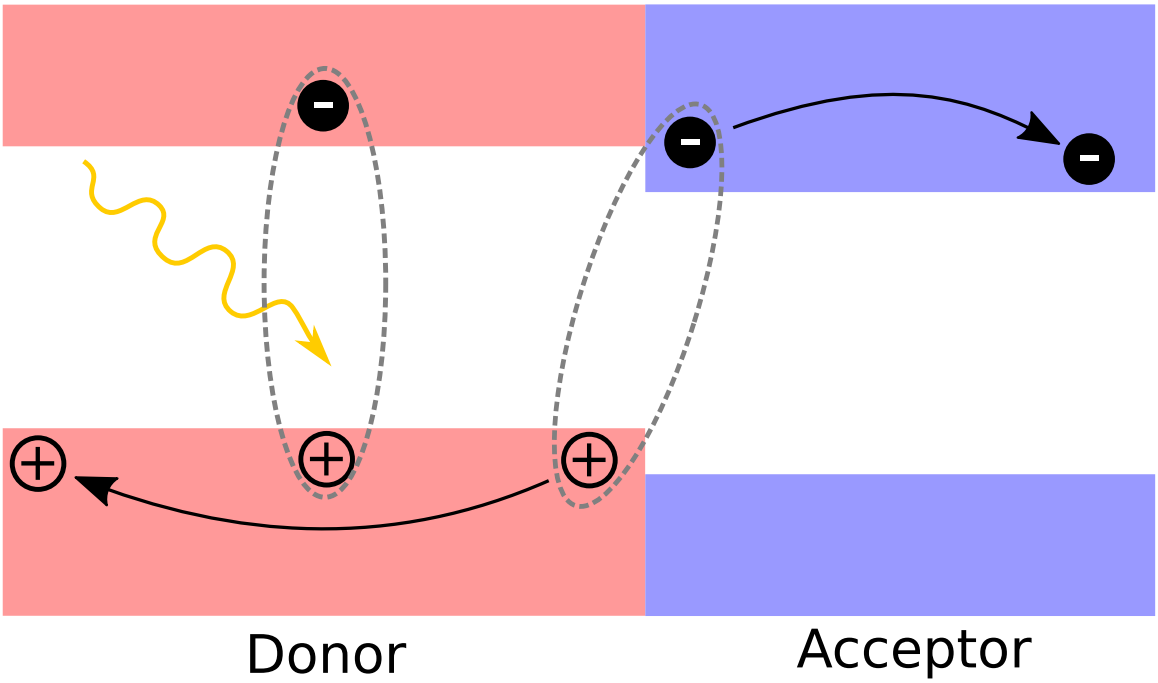

Figure 1.1: The basic working principle of an organic solar cell: light absorption in the donor creates excitons which dissociate at the donor-acceptor interface, creating free charge carries.

Another factor imposing a bound on efficiencies of PVs (organic and inorganic) made from a single absorbing material is known as the Shockley-Queisser limit [3]. Given a single absorber with a certain band gap, only photons from the solar spectrum that match the band gap in energy can be converted efficiently into charge carriers (Fig. 1.2). Photons with energies below the band gap simply cannot be absorbed and hence fail to create electron-hole pairs. While high-energy photons can be absorbed, their excess energy above the band gap is also wasted. This is because excited electrons above the conduction band edge thermalise their excess energy very quickly and fall back to the band edge. Given the solar spectrum this means that an ideal solar cell with a single absorber can achieve a maximum efficiency of around 34%.

One approach to circumvent the Shockley-Queisser limit is to construct solar cells with multiple absorbing materials with different band gaps, giving better coverage of the solar spectrum [4]. While such multi-junction solar cells achieve high efficiencies, this is at the expense of much higher manufacturing complexity and cost. Building a multi-junction cell requires the layering of a range of different materials, effectively connecting several PV interfaces in series. Because of the electrical connection in series, the band gaps have to be chosen carefully such as to ensure that the currents across each interface are matched, given the solar spectrum.

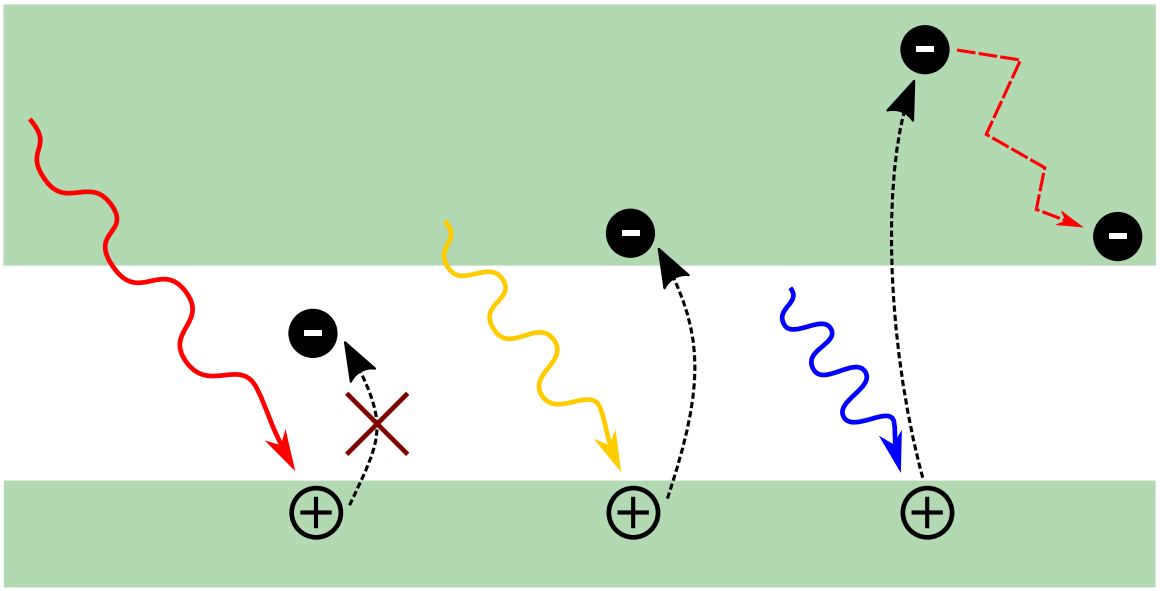

Figure 1.2: Illustration of the Shockley-Queisser limit. Low-energy sub-band-gap photons cannot be absorbed. Electrons promoted above the conduction band edge by high-energy photons quickly thermalise their excess energy and fall back to the band edge.

Multiple exciton generation (MEG) [5] provides an alternative way of tackling the problem. The basic idea is simple: thermalisation losses due to relaxation of electrons to the conduction band edge would be avoided if high-energy photons could be converted into multiple excitons (each with lower energy, close to the band edge). This process is known to occur in quantum dots made from inorganic semiconductors [6].

A particularly interesting type of MEG has been observed in organic materials such as pentacene, called singlet exciton fission or singlet fission for short [7, 8]. In singlet fission, photoexcited singlet excitons rapidly and spontaneously convert into pairs of triplet excitons with about half the energy each. The process can occur very efficiently since it is spin-allowed: the triplet excitons are correlated in such a way that the overall spin-wavefunction is still a singlet. Giving a satisfactory account of singlet fission has been a challenging problem for theory. There is ongoing debate in the literature about which electronic states are involved in the process, and how sufficiently strong coupling is established between these states. The difficulty for theoretical modelling lies in the involvement of different electronic states with distinct characters that couple strongly to both the vibrational and electrostatic environment.

In this thesis we aim address some of these challenges by investigating singlet fission in pentacene using *ab initio* techniques. To capture the disorder and environment interactions which are so important in organics, accurate electronic structure methods are required that

scale favourably to large system sizes. Linear-scaling density functional theory [9] is such a method, and it has become available only relatively recently. It holds a lot of promise to elucidate a range of phenomena that arise in organics due to the complex electron-hole interactions, and which are largely absent in inorganics. We also use density functional theory to parametrise effective models of the interaction between electronic and vibrational degrees of freedom, forming the basis for sophisticated quantum many-body simulations of singlet fission.

This thesis is structured as follows:

- Chapter 2 reviews the theoretical underpinnings of our primary computational tool, density functional theory (DFT). In addition to the ground state case, we also review two excited-state methods, constrained DFT and (linear-response) time-dependent DFT. The rest of the chapter introduces the concept of linear-scaling DFT in the context of its implementation in the ONETEP code.
- Chapter 3 lays out the basics of electronic excitations in organic semiconductors, as well as the basics of the singlet fission process and its potential relevance for photovoltaics. We elaborate these concepts for the case of pentacene and discuss prior experimental and theoretical work on the mechanism of singlet fission in pentacene.
- Chapter 4 details our work on using constrained DFT to obtain bulk-converged energies of intermolecular charge-transfer states in the pentacene crystal. We devise an electrostatic correction scheme that allows us to obtain energies in the infinite-crystal limit from a range of supercell DFT calculations.
- Chapter 5 discusses work on modelling the dynamics of singlet fission in a molecular pentacene dimer. We employ DFT to parametrise a simplified vibronic coupling Hamiltonian for this system. Quantum dynamics calculations allow us to trace the time evolution of electronic states during singlet fission, elucidating the crucial role of vibrational modes in the process.
- Chapter 6 continues our investigation of molecular pentacene dimers, now focusing on how fission is affected by side-group engineering and solvent environments. We perform large-scale time-dependent DFT calculations on dimers, embedded in solvent shells sampled from empirical-potential molecular dynamics, to model environmental effects. We relate our results to experimental studies of fission in pentacene dimers with different side-groups in a range of solvents.
- Chapter 7 provides a summary of the findings and an outlook.

Chapter 2

Density functional theory

The starting point for all theory of electronic structure is the Hamiltonian describing a systems of electrons and nuclei,

$$\begin{aligned}\hat{H} &= -\sum_i \frac{\hbar^2}{2m_e}\nabla_i^2 + \frac{1}{2}\sum_{i\neq j}\frac{e^2}{4\pi\epsilon_0|\mathbf{r}_i-\mathbf{r}_j|} - \sum_{i,I}\frac{Z_I e^2}{4\pi\epsilon_0|\mathbf{r}_i-\mathbf{R}_I|} \\ &\quad -\sum_I \frac{\hbar^2}{2M_I}\nabla_I^2 + \frac{1}{2}\sum_{I\neq J}\frac{Z_I Z_J e^2}{4\pi\epsilon_0|\mathbf{R}_I-\mathbf{R}_J|},\end{aligned} \tag{2.1}$$

where lower/upper case indices refer to electrons/nuclei. The Hamiltonian is composed of kinetic terms for electrons and nuclei (1st and 4th term), electron-electron Coulomb interaction (2nd term), potential energy of electrons due to nuclei (3rd term), and nucleus-nucleus interaction (5th term).

We adopt the Born-Oppenheimer or adiabatic approximation [10], which separates electron and nuclear dynamics. This is justified due to the separation of mass scales, i.e. $m_e \ll M_I$, which means that the timescale of electron dynamics is much shorter than the timescale of nuclear dynamics. Thus the nuclei act as a quasi-stationary background for the electrons, and restricting the analysis to electrons only is a good approximation. We will drop this simplified assumption in chapter 5 where we discuss the interaction of electronic and nuclear degrees of freedom in the context of singlet fission.

Disregarding nuclear motion, the fundamental Hamiltonian of electronic structure reads

$$\hat{H} = \hat{T} + \hat{V}_{\text{int}} + \hat{V}_{\text{ext}} + E_{II}, \tag{2.2}$$

with (electronic) kinetic energy operator $\hat{T}$, electron-electron interaction $\hat{V}_{\text{int}}$, external potential due to nuclei $\hat{V}_{\text{ext}}$, and Coulomb interaction of nuclei E_{II}. Within the Born-Oppenheimer approximation E_{II} is a constant that does not affect electron dynamics, and can be ignored in

most contexts. For the sake of notation we use Hartree atomic units $\hbar = m_e = e = 4\pi\epsilon_0 = 1$ in the following.

Essentially, electronic structure comes down to finding eigenenergies and eigenstates of the fundamental Hamiltonian. However, attacking this problem directly is completely impractical for all but the simplest of cases. The reason for this is the exponential explosion of the Hilbert space with the number of degrees of freedom. This chapter is dedicated to density functional theory, a reformulation of the problem that allows the development of approximate computational schemes with much more favourable scaling than the direct approach.

2.1 Fundamentals of density functional theory

In the following we review the theoretical basis of density functional theory (or DFT for short), constituted by the Hohenberg-Kohn theorems, stating that the problem of electronic structure can be reduced to considering functionals of the electronic density only. Furthermore, we discuss the Kohn-Sham approach which is need to make DFT a useful tool for practical electronic structure calculations. Our exposition of the fundamentals of DFT largely follows Ref. [11].

2.1.1 The Hohenberg-Kohn theorems

The Hohenberg-Kohn (HK) theorems [12] lie at the heart of density functional theory. The first theorem states that for a many-electron system in an arbitrary external potential $V_{\text{ext}}(\mathbf{r})$, this very potential $V_{\text{ext}}(\mathbf{r})$ is determined up to an additive constant by the ground state electron density $n_0(\mathbf{r})$. Hence, $n_0(\mathbf{r})$ fixes the system Hamiltonian (up to a constant) and thereby the whole energy spectrum of the system including the associated wave functions. This means that all system properties are fully determined by the ground state electron density $n_0(\mathbf{r})$ alone.

The statement of the second HK theorem is that one can define an energy functional $E[n]$ of the electron density $n(\mathbf{r})$ for any external potential $V_{\text{ext}}(\mathbf{r})$, given by

$$E[n] = F[n] + \int \mathrm{d}^3 r V_{\text{ext}}(\mathbf{r}) n(\mathbf{r}), \tag{2.3}$$

where $F[n]$ is a universal functional (independent of the potential), such that the ground state energy E_0 of the system with external potential $V_{\text{ext}}(\mathbf{r})$ is the global minimum of $E[n]$. The density $n(\mathbf{r})$ for which this global minimum is attained is precisely the ground state density $n_0(\mathbf{r})$, i.e. $E_0 = E[n_0]$.

Proof of the Hohenberg-Kohn theorems

The proof of the first theorem proceeds by contradiction. We suppose there existed two external potentials $V_{\text{ext}}^{(1)}(\mathbf{r})$ and $V_{\text{ext}}^{(2)}(\mathbf{r})$, differing by more than a constant, which give rise to the same ground state density $n_0(\mathbf{r})$. The two potentials lead to different Hamiltonian operators $\hat{H}^{(1)}$, $\hat{H}^{(2)}$, and different ground state wave functions $\left|\Psi^{(1)}\right\rangle$ and $\left|\Psi^{(2)}\right\rangle$ which we assume to have the same density $n_0(\mathbf{r})$. Since the ground state wave function minimises the energy expectation value of its respective Hamiltonian according to the variational principle, we have the inequalities

$$E^{(1)} = \left\langle \Psi^{(1)} \middle| \hat{H}^{(1)} \middle| \Psi^{(1)} \right\rangle < \left\langle \Psi^{(2)} \middle| \hat{H}^{(1)} \middle| \Psi^{(2)} \right\rangle, \tag{2.4}$$

and

$$E^{(2)} = \left\langle \Psi^{(2)} \middle| \hat{H}^{(2)} \middle| \Psi^{(2)} \right\rangle < \left\langle \Psi^{(1)} \middle| \hat{H}^{(2)} \middle| \Psi^{(1)} \right\rangle. \tag{2.5}$$

The strict inequalities assume that the ground state is non-degenerate. The theorem also holds in the degenerate case as will be shown in the discussion of the constrained search picture. The right hand side of inequality (2.4) can be rewritten with reference to the external potentials:

$$\begin{aligned} \left\langle \Psi^{(2)} \middle| \hat{H}^{(1)} \middle| \Psi^{(2)} \right\rangle &= \left\langle \Psi^{(2)} \middle| \hat{H}^{(2)} \middle| \Psi^{(2)} \right\rangle + \left\langle \Psi^{(2)} \middle| \hat{H}^{(1)} - \hat{H}^{(2)} \middle| \Psi^{(2)} \right\rangle \\ &= E^{(2)} + \int \mathrm{d}^3 r \left[V_{\text{ext}}^{(1)}(\mathbf{r}) - V_{\text{ext}}^{(2)}(\mathbf{r}) \right] n_0(\mathbf{r}). \end{aligned}$$

The Hamiltonians only differ in the external potential part since the kinetic and interaction terms are universal for all many-electron systems. Combining this with Eq. (2.4) one obtains

$$E^{(1)} < E^{(2)} + \int \mathrm{d}^3 r \left[V_{\text{ext}}^{(1)}(\mathbf{r}) - V_{\text{ext}}^{(2)}(\mathbf{r}) \right] n_0(\mathbf{r}). \tag{2.6}$$

An analogous inequality follows from Eq. (2.5), i.e.

$$E^{(2)} < E^{(1)} + \int \mathrm{d}^3 r \left[V_{\text{ext}}^{(2)}(\mathbf{r}) - V_{\text{ext}}^{(1)}(\mathbf{r}) \right] n_0(\mathbf{r}). \tag{2.7}$$

Adding inequalities (2.6) and (2.7) together leads to the contradictory statement

$$E^{(1)} + E^{(2)} < E^{(1)} + E^{(2)}.$$

Hence, the initial assumption must have been false and there cannot exist two different external potentials that lead to the same ground state density. Reversing the statement, this means that the ground state density uniquely determines the external potential (up to a constant). Therefore, the ground state density fixes the Hamiltonian of the system, from which all physical properties follow, in particular the excitation energy spectrum and the associated wave functions.

To prove the second theorem we note that since the density determines all properties of the system including the ground state energy, one can write down the total energy functional

$$E[n] = F[n] + \int \mathrm{d}^3 r V_{\mathrm{ext}}(\mathbf{r}) n(\mathbf{r}). \tag{2.8}$$

The functional $F[n]$ includes kinetic and interaction energy of the electrons:

$$F[n] = T[n] + E_{\mathrm{int}}[n]. \tag{2.9}$$

It is by construction a universal functional which applies to all many-electron systems, independent of the external potential $V_{\mathrm{ext}}(\mathbf{r})$. Given some system with ground state density $n^{(1)}(\mathbf{r})$ and associated external potential $V_{\mathrm{ext}}^{(1)}(\mathbf{r})$, the total energy functional yields the ground state energy, equal to the expectation value of the Hamiltonian in the ground state:

$$E^{(1)} = E[n^{(1)}] = \left\langle \Psi^{(1)} \middle| \hat{H}^{(1)} \middle| \Psi^{(1)} \right\rangle. \tag{2.10}$$

A different density $n^{(2)}(\mathbf{r})$ must correspond to a different wave function $\left|\Psi^{(2)}\right\rangle$ which is therefore distinct from the ground state wave function. Due to the variational principle this means that the corresponding energy $E^{(2)}$ must satisfy

$$E^{(1)} = \left\langle \Psi^{(1)} \middle| \hat{H}^{(1)} \middle| \Psi^{(1)} \right\rangle < \left\langle \Psi^{(2)} \middle| \hat{H}^{(1)} \middle| \Psi^{(2)} \right\rangle = E^{(2)}, \tag{2.11}$$

demonstrating that the functional $E[n]$ attains its global minimum for the density $n^{(1)}(\mathbf{r})$, i.e. precisely for the ground state density of the system.

Constrained search picture of DFT

The proofs of the Hohenberg-Kohn theorems as shown are not constructive. They merely demonstrate the existence of a universal density functional but provide no prescription whatsoever for how this functional might be evaluated. Here, the constrained search picture of DFT due to Levy and Lieb [13–15] provides an alternative perspective and gives an explicit (though computationally impractical) definition of $E[n]$.

For any wave function $|\Psi\rangle$, the energy is just the expectation value of the Hamiltonian operator, namely

$$E = \langle \Psi | \hat{H} | \Psi \rangle = \langle \Psi | \hat{T} | \Psi \rangle + \langle \Psi | \hat{V}_{\mathrm{int}} | \Psi \rangle + \int \mathrm{d}^3 r V_{\mathrm{ext}}(\mathbf{r}) n(\mathbf{r}), \tag{2.12}$$

where the expression has been broken down into kinetic energy, interaction energy, and potential energy due to $V_{\mathrm{ext}}(\mathbf{r})$. The ground state of this system can in principle be found by minimising the energy expectation value over all possible (normalised) wave functions, i.e.

$$E_0 = \min_{|\Psi\rangle} \langle \Psi | \hat{H} | \Psi \rangle \tag{2.13}$$

Now, the idea is to interpret this minimisation as a two-step process, first minimising over all wave functions consistent with a given density $n(\mathbf{r})$, and then minimising this object over all possible densities:

$$E_0 = \min_{n(\mathbf{r})} \left[\min_{|\Psi\rangle \to n(\mathbf{r})} \langle \Psi | \hat{H} | \Psi \rangle \right] \equiv \min_{n(\mathbf{r})} E[n]. \tag{2.14}$$

One can split $E[n]$ into the kinetic and interaction energy of electrons which is independent of the external potential, and the potential energy:

$$E[n] = \min_{|\Psi\rangle \to n(\mathbf{r})} \left[\langle \Psi | \hat{T} | \Psi \rangle + \langle \Psi | \hat{V}_{\text{int}} | \Psi \rangle \right] + \int \mathrm{d}^3 r V_{\text{ext}}(\mathbf{r}) n(\mathbf{r}). \tag{2.15}$$

This provides an explicit definition of the universal density functional:

$$F[n] = \min_{|\Psi\rangle \to n(\mathbf{r})} \left[\langle \Psi | \hat{T} | \Psi \rangle + \langle \Psi | \hat{V}_{\text{int}} | \Psi \rangle \right]. \tag{2.16}$$

2.1.2 Making DFT practical: The Kohn-Sham system

In principle, the Hohenberg-Kohn theorems state that it is possible to reduce the problem of electronic structure theory to only considering the density and a universal functional of it. However, it turns out that this alone is of very limited use in practice since the relationship between density and system properties is extremely subtle. For example, it is generally not known how to infer even general system features - like whether a material is a metal or an insulator - from the electron density. The crux is that density functional theory in its pure form gives no prescription for a computationally feasible construction of the density functional.

The idea of Kohn-Sham (KS) theory [16] is to replace the real, interacting electron system with a fictitious, non-interacting system (the Kohn-Sham system). The basic assumption is that the exact ground state density $n_0(\mathbf{r})$ can be represented by the density of the non-interacting auxiliary system. The Hamiltonian consists of the usual kinetic energy operator $\hat{T} = -\frac{1}{2}\sum_i \nabla_i^2$ plus an effective potential $V_{\text{eff}}(\mathbf{r})$ which includes the external potential and in principle all many-body effects:

$$\hat{H}_{\text{aux}} = \hat{T} + V_{\text{eff}}(\mathbf{r}). \tag{2.17}$$

Because now we are dealing with a (formally) non-interacting system, the wave-function can be represented by a single Slater determinant of spin-orbitals ψ_i^σ. The density is then simply given by a sum of the squared moduli of the spin-orbitals:

$$n(\mathbf{r}) = \sum_{\sigma,i} |\psi_i^\sigma(\mathbf{r})|^2 . \tag{2.18}$$

Similarly, one can easily evaluate the kinetic energy T_s of the non-interacting system in terms of the spin-orbitals:

$$T_s = \frac{1}{2}\sum_{\sigma,i}\int \mathrm{d}^3r\,|\nabla\psi_i^\sigma(\mathbf{r})|^2\,. \tag{2.19}$$

Now we are in a position to state the Kohn-Sham form of the ground state energy functional (Eq. (2.8)). It is given by

$$E_{\mathrm{KS}}[n] = \underbrace{T_s[n] + E_{\mathrm{Hartree}}[n] + E_{\mathrm{xc}}[n]}_{F[n]} + \int \mathrm{d}^3r V_{\mathrm{ext}}(\mathbf{r})n(\mathbf{r}), \tag{2.20}$$

where the Hartree energy is defined as the self-interaction energy of a classical charge distribution with density $n(\mathbf{r})$ due to Coulomb repulsion:

$$E_{\mathrm{Hartree}}[n] = \frac{1}{2}\int \mathrm{d}^3r \int \mathrm{d}^3r' \frac{n(\mathbf{r})n(\mathbf{r}')}{|\mathbf{r}-\mathbf{r}'|}. \tag{2.21}$$

The exchange and correlation energy E_{xc} formally takes care of all the contributions due to many-body exchange and correlation effects not accounted for by the other terms. In particular, both effects will tend to keep the electrons apart, thereby lowering the Coulomb (and hence total) energy of the system. This can be interpreted as the binding energy of each electron with a positive exchange-correlation hole that it creates in the surrounding charge distribution.

Still, $E_{\mathrm{xc}}[n]$ is an unknown functional since it contains all the subtle many-body effects. However, the Kohn-Sham approach brings the advantage that the exchange-correlation energy is only a relatively small component of the total energy, and it can be approximated to a good degree as a (semi-)local functional of the density. Given some approximation for the xc-functional we would like to minimise Eq. (2.20) with respect to the spin-orbitals representing the density. This is a variational problem leading to an effective Schrödinger equation with Hamiltonian

$$\hat{H}_{\mathrm{KS}} = \hat{T} + V_{\mathrm{KS}}(\mathbf{r}), \tag{2.22}$$

with

$$\begin{aligned} V_{\mathrm{KS}}(\mathbf{r}) &= \frac{\delta E_{\mathrm{Hartree}}}{\delta n(\mathbf{r})} + \frac{\delta E_{\mathrm{xc}}}{\delta n(\mathbf{r})} + V_{\mathrm{ext}}(\mathbf{r}) \\ &= V_{\mathrm{Hartree}}(\mathbf{r}) + V_{\mathrm{xc}}(\mathbf{r}) + V_{\mathrm{ext}}(\mathbf{r}). \end{aligned} \tag{2.23}$$

The eigenvalue equations for the orbitals resulting from the Hamiltonian Eq. (2.22) are known as the Kohn-Sham equations. They are independent-particle equations with a potential that depends on the density. Hence, a solution must be found self-consistently since the orbitals determine the density via Eq. (2.18). In practice, this problem is usually tackled in an iterative manner, i.e. starting from some initial guess the density is updated based on

the orbitals found in the last iteration, leading to a new potential and new orbitals obtained from solving the Kohn-Sham equations using this new potential. This procedure is repeated until the change of the density/orbitals becomes smaller than some specified convergence goal.

2.1.3 Exchange-correlation functionals

Finding an exact expression for the exchange-correlation functional $E_{\mathrm{xc}}[n]$ is as unrealistic as finding an exact form of the universal energy functional $F[n]$. However, because of the separation of independent-particle kinetic energy and long-range Coulomb interaction from $E_{\mathrm{xc}}[n]$ in the Kohn-Sham formulation, it is possible to find reasonable approximations which are local or at least semi-local in the density. Here, we will give a short overview of the most important and widely used approximations for $E_{\mathrm{xc}}[n]$.

The local density approximation

The local (spin) density approximation or L(S)DA starts from the observation that the valence electron density of many condensed matter systems of interest (e.g. metals) is reasonably close to that of a homogeneous electron gas. For a system close to that limit it is known that exchange and correlation effects are local in nature, and thus independent of the electron density at a distance. This warrants the following *Ansatz* for the exchange-correlation functional:

$$E_{\mathrm{xc}}^{\mathrm{LDA}}[n] = \int \mathrm{d}^3 r n(\mathbf{r}) \epsilon_{\mathrm{xc}}^{\mathrm{hom}}(n(\mathbf{r})), \tag{2.24}$$

where $\epsilon_{\mathrm{xc}}^{\mathrm{hom}}(n)$ is the xc energy per particle of a uniform (and unpolarised) electron gas with density n. The exchange part of this energy can be calculated analytically from the Hartree-Fock theory of the uniform electron gas, one obtains

$$\epsilon_{\mathrm{x}}^{\mathrm{hom}}(n) = -\frac{3}{4}\left(\frac{3}{\pi}\right)^{1/3} \cdot n^{1/3}. \tag{2.25}$$

If spin polarisation plays a role, i.e. $n^{\uparrow}(\mathbf{r}) \neq n^{\downarrow}(\mathbf{r})$, one has to consider the more general form $\epsilon_{\mathrm{xc}}^{\mathrm{hom}} = \epsilon_{\mathrm{xc}}^{\mathrm{hom}}(n^{\uparrow}, n^{\downarrow})$. The correlation energy of the homogeneous electron gas cannot be calculated analytically, except for limiting cases which can be treated perturbatively (i.e. the high-density limit). However, it is possible to obtain this energy numerically to high accuracy employing Monte Carlo methods [17]. Empirical fits to these results are usually used in practical DFT calculations.

Because LDA treats the effects of exchange in a purely local manner, it suffers from self-interaction errors which are especially pronounced in very confined systems (e.g. atoms).

Still, the approximation gives decent results for a wide range of systems. This is due to the fact that LDA obeys a range of certain conditions or sum rules that have to be satisfied by the exact xc-functional $E_{\mathrm{xc}}[n]$ since the approximation is exact in the homogeneous case [18]. Also, its low computational cost makes it an attractive choice in practice, especially when treating large systems.

Generalised-gradient approximations

There is a wide variety of approximate functionals that go beyond the LDA. As a first refinement one can formulate functionals that not only depend on the local density but also its gradient (and higher derivatives), known as generalised-gradient approximations (GGAs) [16, 19, 20]. A GGA functional has the general form (including spin)

$$E_{\mathrm{xc}}^{\mathrm{GGA}}[n^{\uparrow}, n^{\downarrow}] = \int \mathrm{d}^3 r n(\mathbf{r}) \epsilon_{\mathrm{xc}}(n^{\uparrow}, n^{\downarrow}, |\nabla n^{\uparrow}|, |\nabla n^{\downarrow}|, \ldots). \tag{2.26}$$

This method amounts to a low-order expansion of exchange and correlation energies in derivatives of the density. The coefficients of this expansion can be calculated analytically. However, this approach does not result in a systematic improvement compared to LDA. The problem is that GGA functionals violate exact conditions satisfied by LDA, and the low-order expansion often breaks down due to the rapidly changing densities in real materials.

Examples of popular choices of GGAs are the PBE functional proposed by Perdew, Burke and Enzerhof [21], and the BLYP functional combining an exchange term proposed by Becke [22] and a correlation term proposed by Lee, Yang and Parr [23].

Hybrid functionals

A host of more refined functionals have been developed that go beyond LDA and GGA by including more non-locality. One can abandon the notion of explicit density functionals and reference the KS orbitals directly (as in the definition of T_s). This makes it possible to define functionals that include Hartree-Fock exchange between the KS orbitals. Such functionals are known as hybrid functionals. This approach can be motivated with the idea of *adiabatic connection*. Starting with non-interacting electrons, one can imagine the Coulomb interaction between the electrons being turned on slowly until it reaches its physical value. For the non-interacting system Hartree-Fock exchange is exact, whereas the exchange-correlation of the fully interacting system can be approximated with a (semi-)local functional. This suggests taking some weighted average of the two to define a functional. An example of a widely used hybrid functional is B3LYP [24]:

$$E_{\mathrm{xc}}^{\mathrm{B3LYP}} = E_{\mathrm{x}}^{\mathrm{LDA}} + a_0(E_{\mathrm{x}}^{\mathrm{HF}} - E_{\mathrm{x}}^{\mathrm{LDA}}) + a_x(E_{\mathrm{x}}^{\mathrm{GGA}} - E_{\mathrm{x}}^{\mathrm{LDA}}) + a_c(E_{\mathrm{c}}^{\mathrm{GGA}} - E_{\mathrm{c}}^{\mathrm{LDA}}), \tag{2.27}$$

where $a_0 = 0.20$, $a_x = 0.72$, and $a_c = 0.81$. Hybrid functionals overcome some of the errors inherent in the (semi-)local functionals, but significantly increase the computational cost of calculations.

Range-separated hybrid functionals

While hybrids constitute an improvement over LDA/GGA, they still have significant shortcomings in scenarios where long-range exchange is important, such as charge-transfer and dissociation curves. Because they only contain a fraction of Hartree-Fock exchange the exchange potential asymptotically behaves as $-a_0/r$, where a_0 is the fraction of Hartree-Fock exchange ($a_0 = 0.20$ for B3LYP), instead of the exact $-1/r$ behaviour. One can correct the long-range behaviour while retaining the functional at short ranges by splitting the Coulomb interaction into short and long-range parts [25]:

$$\frac{1}{r} = \frac{1 - \mathrm{erf}(\mu r)}{r} + \frac{\mathrm{erf}(\mu r)}{r}, \tag{2.28}$$

where erf is the error function and μ is a parameter controlling the separation between short and long ranges. Now, the LDA/GGA contribution to exchange is calculated using the short-range Coulomb interaction, while the long-range part is used in the evaluation of Hartree-Fock exchange. This procedure is referred to as long-range-correction (LC). Given a (semi-)local starting functional, such as BLYP, one obtains a long-range-corrected version of the functional, in this case LC-BLYP.

2.2 Time-dependent density functional theory

Kohn-Sham DFT as described in the previous section is a ground state theory. As such it is therefore not directly suited to treat excitations of a system. The energy eigenvalues of the Kohn-Sham orbitals in ground state DFT generally do not have physical meaning, except for the eigenvalue of the highest occupied orbital which corresponds to the negative of the first ionization energy (by virtue of Koopmans' theorem [26]). In particular, eigenvalues of unoccupied orbitals cannot be interpreted as excitation energies. In order to make progress it is necessary to go beyond ground state DFT by including time dependence. This time-dependent version of DFT (TDDFT) is capable of describing excitations from the ground state and the associated energies. The central object of this approach is the time-dependent density $n(\mathbf{r}, t)$ which bears essentially a one-to-one relationship with the time-dependent external potential $V_{\mathrm{ext}}(\mathbf{r}, t)$, established by the Runge-Gross theorem [27]. In a manner similar to ground state DFT, one can construct a time-dependent Kohn-Sham system. In the TDDFT framework, the excitations and their energies manifest themselves in the response

of this Kohn-Sham system to time-dependent perturbations of the external potential. The brief review of the TDDFT method we present here mostly follows Ref. [28].

2.2.1 The Runge-Gross theorem

The general time-dependent many-electron problem is governed by the time-dependent Schrödinger equation:

$$\mathrm{i}\partial_t \left|\Psi(t)\right\rangle = \hat{H}\left|\Psi(t)\right\rangle \equiv \left[\hat{T} + \hat{V}_{\mathrm{int}} + \hat{V}_{\mathrm{ext}}(t)\right]\left|\Psi(t)\right\rangle, \tag{2.29}$$

where $\hat{V}_{\mathrm{ext}}(t)$ is the operator corresponding to the time-dependent external potential $V_{\mathrm{ext}}(\mathbf{r},t)$. The Runge-Gross theorem is the time-dependent analogue of the Hohenberg-Kohn theorems in the time-independent theory. It states that there exists a one-to-one correspondence between the time-dependent density $n(\mathbf{r},t)$ and the external potential $V_{\mathrm{ext}}(\mathbf{r},t)$, given that the time evolution starts from a fixed initial state $\left|\Psi(0)\right\rangle \equiv \left|\Psi_0\right\rangle$ [27]. By considering the equations of motion for the current density $\mathbf{j}(\mathbf{r},t)$, the proof of the theorem demonstrates that densities evolving from the initial wave function $\left|\Psi_0\right\rangle$ in different time-dependent potentials $V_{\mathrm{ext}}(\mathbf{r},t)$ are necessarily different. This assumes that the potentials are analytic in time around the initial time. In addition, the solutions of the time-dependent Schrödinger equation are known to be unique, hence the one-to-one correspondence is established. As a consequence, the time-dependent density (together with the initial state) uniquely determines the wave function up to a phase. This means that the expectation value of any observable is a functional of the density and the initial state.

2.2.2 Time-dependent Kohn-Sham system

As in the ground state theory, finding explicit functionals of the density which are practically useful is a hard problem. Again, switching to a non-interacting (but now time-dependent) Kohn-Sham system is the way forward. The non-interacting wave function must reproduce the density found in the interacting case. The question of whether this is possible in general is known as the (non-interacting) V-representability problem [29]. The answer to this question turns out to be positive under a range of reasonable assumptions about the density [30].

The time-dependent KS equations describe the time evolution of the KS orbitals:

$$\mathrm{i}\partial_t \psi_j^\sigma(\mathbf{r},t) = \left[-\frac{1}{2}\nabla^2 + V_{\mathrm{KS}}[n](\mathbf{r},t)\right]\psi_j^\sigma(\mathbf{r},t), \tag{2.30}$$

with a KS potential that splits into Hartree, exchange-correlation, and external potential contributions as in the ground state case, i.e.

$$V_{\mathrm{KS}}[n](\mathbf{r},t) = \int \mathrm{d}^3 r' \frac{n(\mathbf{r}',t)}{|\mathbf{r}-\mathbf{r}'|} + V_{\mathrm{xc}}[n](\mathbf{r},t) + V_{\mathrm{ext}}[n](\mathbf{r},t). \tag{2.31}$$

Strictly, the functionals not only depend on the density but also on the initial states of the interacting and non-interacting systems. However, if these states are non-degenerate ground states (which is the case for a wide range of systems) then all potentials are functionals of the density alone.

2.2.3 Linear-response formalism for TDDFT

In principle, one could now start in the ground state and then integrate the time-dependent KS system with a perturbation of the external potential. The (time-domain) Fourier transform of the density response would then give access to the excitation spectrum. A more practical approach that works directly in the frequency domain is based on a linear-response formalism which considers the first order response of the density to a perturbation of the external potential [31, 32]. Poles of the response function in the frequency domain correspond to resonant driving, i.e. excited eigenstates of the system. This approach is known as linear-response TDDFT (LR-TDDFT).

We consider a system that is in its ground state initially. At time $t = 0$ a perturbation of the external potential is switched on (e.g. electromagnetic wave). We write the potential as

$$V_{\text{ext}}(\mathbf{r}, t) = V_{\text{ext},0}(\mathbf{r}) + \delta V_{\text{ext}}(\mathbf{r}, t), \tag{2.32}$$

with $\delta V_{\text{ext}}(\mathbf{r}, t) \equiv 0$ for $t \leq 0$. We now define the linear density response function χ as

$$\chi(\mathbf{r}, t; \mathbf{r}', t') = \left.\frac{\delta n(\mathbf{r}, t)}{\delta V_{\text{ext}}(\mathbf{r}', t')}\right|_{V_{\text{ext},0}}. \tag{2.33}$$

In terms of χ the first order density response n_1 to the perturbation δV_{ext} is given by

$$n_1(\mathbf{r}, t) = \int_0^\infty \mathrm{d}t' \int \mathrm{d}^3 r' \chi(\mathbf{r}, t; \mathbf{r}', t') \delta V_{\text{ext}}(\mathbf{r}', t'). \tag{2.34}$$

Using time-dependent perturbation theory, the response function can be evaluated in terms of the full spectrum $|\Psi_j\rangle$, Ω_j, yielding the spectral representation:

$$\chi(\mathbf{r}, \mathbf{r}', \omega) = \sum_j \left[\frac{\langle\Psi_0|\,\hat{n}(\mathbf{r})\,|\Psi_j\rangle\,\langle\Psi_j|\,\hat{n}(\mathbf{r}')\,|\Psi_0\rangle}{\omega - \Omega_j + \mathrm{i}0^+} - \frac{\langle\Psi_0|\,\hat{n}(\mathbf{r}')\,|\Psi_j\rangle\,\langle\Psi_j|\,\hat{n}(\mathbf{r})\,|\Psi_0\rangle}{\omega + \Omega_j + \mathrm{i}0^+} \right], \tag{2.35}$$

where $\hat{n}(\mathbf{r}) = \sum_i \delta(\mathbf{r} - \hat{\mathbf{r}}_i)$ is the density operator, $|\Psi_0\rangle$ denotes the (unperturbed) ground state, and a Fourier transform from the time difference $t - t'$ to the frequency ω has been applied (exploiting time-translational invariance). As such, this expression is not helpful if applied to the full interacting system since its evaluation already requires full knowledge of the spectrum. The idea of LR-TDDFT is to calculate the response χ_{KS} of the non-interacting KS system using Eq. (2.35), and then relate χ_{KS} to the "real" response function χ.

In order to evaluate the response of the KS system one has to enumerate all its states. They are simply given by all possible Slater determinants of the KS spin-orbitals ψ_k^σ. Plugging those into Eq. (2.35) yields

$$\chi_{\mathrm{KS}}(\mathbf{r},\mathbf{r}',\omega) = \sum_{k,l}\sum_{\sigma} (f_k^\sigma - f_l^\sigma)\, \frac{\psi_k^\sigma(\mathbf{r})^*\psi_l^\sigma(\mathbf{r})\psi_l^\sigma(\mathbf{r}')^*\psi_k^\sigma(\mathbf{r}')}{\omega - \left(\epsilon_l^\sigma - \epsilon_k^\sigma\right) + \mathrm{i}0^+}, \tag{2.36}$$

where the ϵ_i^σ denote KS eigenvalues and the f_i^σ are the occupation numbers of the KS spin-orbitals in the ground state. To relate the KS response χ_{KS} to the "real" response χ we essentially employ the chain rule for functional derivatives, i.e.

$$\begin{aligned}
\chi(\mathbf{r},t;\mathbf{r}',t') &= \left.\frac{\delta n(\mathbf{r},t)}{\delta V_{\mathrm{ext}}(\mathbf{r}',t')}\right|_{V_{\mathrm{ext},0}} \\
&= \int \mathrm{d}t'' \int \mathrm{d}^3r'' \left.\frac{\delta n(\mathbf{r},t)}{\delta V_{\mathrm{KS}}(\mathbf{r}'',t'')}\right|_{V_{\mathrm{KS}}[n_0]} \cdot \left.\frac{\delta V_{\mathrm{KS}}(\mathbf{r}'',t'')}{\delta V_{\mathrm{ext}}(\mathbf{r}',t')}\right|_{V_{\mathrm{ext},0}} \\
&= \int \mathrm{d}t'' \int \mathrm{d}^3r'' \chi_{\mathrm{KS}}(\mathbf{r},t;\mathbf{r}'',t'') \cdot \left.\frac{\delta V_{\mathrm{KS}}(\mathbf{r}'',t'')}{\delta V_{\mathrm{ext}}(\mathbf{r}',t')}\right|_{V_{\mathrm{ext},0}}
\end{aligned}$$

The remaining derivative in the expression can be rewritten using the definition of the KS potential Eq. (2.31):

$$\begin{aligned}
\left.\frac{\delta V_{\mathrm{KS}}(\mathbf{r}'',t'')}{\delta V_{\mathrm{ext}}(\mathbf{r}',t')}\right|_{V_{\mathrm{ext},0}} &= \int \mathrm{d}^3r''' \left[\frac{1}{|\mathbf{r}''-\mathbf{r}'''|} + f_{\mathrm{xc}}[n](\mathbf{r}'',t'';\mathbf{r}''',t''')\right] \chi(\mathbf{r}''',t'';\mathbf{r}',t') \\
&\quad + \delta(\mathbf{r}''-\mathbf{r}')\delta(t''-t')
\end{aligned}$$

The exchange-correlation kernel f_{xc} is defined as

$$f_{\mathrm{xc}}(\mathbf{r},t;\mathbf{r}',t') = \left.\frac{\delta V_{\mathrm{xc}}[n](\mathbf{r},t)}{\delta n(\mathbf{r}',t')}\right|_{n_0}. \tag{2.37}$$

We now put everything together and perform a Fourier transform with respect to $t-t'$. The convolution theorem takes care of the remaining time variables t'', t''', and we obtain

$$\begin{aligned}
\chi(\mathbf{r},\mathbf{r}',\omega) &= \chi_{\mathrm{KS}}(\mathbf{r},\mathbf{r}',\omega) \\
&\quad + \int \mathrm{d}^3r'' \int \mathrm{d}^3r''' \chi_{\mathrm{KS}}(\mathbf{r},\mathbf{r}'',\omega) f_{\mathrm{Hxc}}(\mathbf{r}'',\mathbf{r}''',\omega)\chi(\mathbf{r}''',\mathbf{r}',\omega),
\end{aligned} \tag{2.38}$$

with the Hartree-xc kernel f_{Hxc} given by

$$f_{\mathrm{Hxc}}(\mathbf{r},\mathbf{r}',\omega) = \frac{1}{|\mathbf{r}-\mathbf{r}'|} + f_{\mathrm{xc}}(\mathbf{r},\mathbf{r}',\omega). \tag{2.39}$$

To simplify notation we can interpret the functions in Eq. (2.38) as infinite-dimensional matrices with entries labelled by position coordinates, and write

$$\chi(\omega) = \chi_{\mathrm{KS}}(\omega) + \chi_{\mathrm{KS}}(\omega)\cdot f_{\mathrm{Hxc}}(\omega)\cdot\chi(\omega). \tag{2.40}$$

Rearranging gives

$$[1 - \chi_{\mathrm{KS}}(\omega) \cdot f_{\mathrm{Hxc}}(\omega)] \cdot \chi(\omega) = \chi_{\mathrm{KS}}(\omega). \tag{2.41}$$

Now, while χ has poles at the true excitation energies, the poles of χ_{KS} occur at the different excitation energies of the KS system. Therefore, for the equation to hold the matrix described by the expression in square brackets must have vanishing eigenvalues for the true excitation energies (such that it can cancel the poles). Put a different way, for the eigenvalue equation

$$\chi_{\mathrm{KS}}(\omega) \cdot f_{\mathrm{Hxc}}(\omega) \cdot \xi(\omega) = \lambda(\omega)\xi(\omega), \tag{2.42}$$

with eigenvalues $\lambda(\omega)$ and eigenvectors $\xi(\omega)$ we necessarily have $\lambda(\Omega_j) = 1$ at the true excitation energies Ω_j. For the purpose of practical use in calculations this equation is recast into a form first introduced by Casida [33], namely an eigenvalue equation for the true excitation energies:

$$\sum_{q'} \left[M_{qq'}(\Omega) + \omega_q \delta_{qq'} \right] \beta_{q'} = \Omega \beta_q. \tag{2.43}$$

The expression uses double-indices $q = (i, a)$ labelling transitions of the KS system from orbital i to a with energy $\omega_q = \epsilon_a - \epsilon_i$. β_q is a vector describing the excitation in terms of these KS transitions labelled by q. The matrix M is given by

$$M_{qq'}(\omega) = \alpha_{q'} \int \mathrm{d}^3 r \int \mathrm{d}^3 r' \Phi_q^*(\mathbf{r}) f_{\mathrm{Hxc}}(\mathbf{r}, \mathbf{r}', \omega) \Phi_{q'}(\mathbf{r}'), \tag{2.44}$$

with $\alpha_{q'} = \pm 2$ depending on whether the transition q' is from occupied to unoccupied (positive sign) or vice versa, and the transition density defined as

$$\Phi_q(\mathbf{r}) = \psi_i^*(\mathbf{r}) \psi_a(\mathbf{r}). \tag{2.45}$$

Eq. (2.43) contains infinitely many KS transitions and must therefore be truncated in practice. Also, it is often a good approximation to only include transitions from occupied to unoccupied KS orbitals. This so-called Tamm-Dancoff approximation [34] is justified for systems where the KS orbitals provide a reasonably accurate description of the fully interacting ground state. Another approximation that is widely employed is the adiabatic approximation, i.e. making the exchange-correlation kernel independent of frequency. This assumes that the exchange-correlation potential depends essentially only on the instantaneous density, and has no memory of the history of n. This makes M independent of ω, hence the problem of solving Eq. (2.43) becomes much more tractable.

2.3 Constrained density functional theory

An alternative way to go beyond a pure ground state theory is constrained density functional theory (cDFT). As the name suggests, the idea is to impose constraints on the system,

specifically on the electron density. The states described by such constraints are generally not energy eigenstates (as in TDDFT) but so-called diabatic states. As properties of the systems of interest are changed (such as geometry) diabatic states defined by charge density constraints retain their electronic character (e.g. being of charge-transfer type). At the same time, the character of (adiabatic) eigenstates is generally significantly altered as the system parameters change. In order to obtain eigenstates from cDFT it is necessary to identify and construct a relevant subspace of the Hilbert space with appropriate constraints, and calculate couplings between the states in this subspace. A diagonalisation of the subspace Hamiltonian then yields approximate eigenstates.

A main advantage of constrained DFT over the previously described LR-TDDFT with local functionals and the adiabatic approximation is its accuracy in predicting energies of charge-transfer states (i.e. states with significant spatial charge separation) [35,36]. Also, while the adiabatic approximation in TDDFT precludes the successful description of multi-excited states, such excitations are accessible for cDFT providing appropriate constraints can be formulated [37,38].

Mathematically, the problem of constrained DFT can be formulated using an extended energy functional. It consists of the familiar total energy functional $E[n]$ augmented with a set of Lagrange multiplier terms which impose a chosen set of constraints on the density:

$$W[n,(V_k)] = E[n] + \sum_k V_k \left(\int \mathrm{d}^3 r \sum_\sigma w_k^\sigma(\mathbf{r}) n^\sigma(\mathbf{r}) - N_k \right), \tag{2.46}$$

where the V_k are constraining potentials (Lagrange multipliers), the w_k^σ are spin-dependent weight functions, and the N_k are target populations. The role of the weight functions w_k^σ is to select designated regions of the spin-density to integrate over. By adjusting the constraining potentials self-consistently these integrated electron populations are to be matched with the chosen target populations N_k, while minimising the total energy with respect to the density. The result of this procedure is a total energy and density such that the density is consistent with the chosen constraints and the total energy is minimal. With reference to the newly introduced functional $W[n,(V_k)]$ one can reformulate the problem as a minimax optimisation, i.e.

$$\begin{aligned} E &= \min_n \max_{V_k} W[n,(V_k)] \\ &= \min_n \max_{V_k} \left[E[n] + \sum_k V_k \left(\int \mathrm{d}^3 r \sum_\sigma w_k^\sigma(\mathbf{r}) n^\sigma(\mathbf{r}) - N_k \right) \right]. \end{aligned} \tag{2.47}$$

As long as at least one of the constraints is not satisfied some of the expression in round brackets are non-zero. This means that the inner maximisation over the constraining potentials V_k can make the value of the functional arbitrarily large. Hence, the outer minimisation

over n can only be successful on the submanifold that is consistent with all the constraints. On this submanifold in turn $W[n] \equiv E[n]$ holds since all the terms in round brackets vanish. Therefore, for the density n_0 which solves the optimisation problem Eq. (2.47), we also have $W[n_0] = E[n_0]$.

We defined populations to be targeted by the cDFT procedure through explicit integration of the spin-density with weight functions. In practice, there exists a certain arbitrariness in how the weight functions are chosen. This is especially the case if the spatial regions to be constrained are not well separated, but belong to a single molecule or molecules with significantly overlapping orbitals. The linear-scaling methods which are subject of the next section represent the electronic state in terms of a density operator expanded in local, non-orthogonal basis functions. Here, it is natural to refer to the local basis functions to define subspaces and calculate populations. However, finding the right prescription for projecting out subspace populations using a non-orthogonal basis set turns out to be quite a subtle issue, which is briefly touched upon in section 2.4.4, and then covered in more detail in chapter 4.

2.4 Linear-scaling DFT with ONETEP

Traditional implementations of DFT construct the non-interacting KS system with an approximate xc functional as was outlined above, and then explicitly solve the KS equations iteratively until self-consistency is reached. Since computing resources are limited, it is necessary to expand all the functions in a finite basis set. Most commonly, plane waves commensurate with the simulation cell with an adjustable short-wavelength cutoff are used, in combination with appropriate pseudopotentials. A plane wave basis set makes it especially easy to apply the kinetic energy operator, and switching between basis and real-space representations can be done with efficient fast Fourier transforms. However, the approach comes with an inherent cubic scaling of the method with system size. The reason is that solving the KS equations amounts to a matrix diagonalisation which scales cubically. Some methods (especially suited for larger systems) employ an iterative scheme rather than direct diagonalisation of the KS system. Still, enforcing the orthonormality requirement on the set of KS orbitals is an operation that scales cubically. Even though this scaling behaviour is quite moderate compared to higher-level methods, it still limits calculations to systems with hundreds to a few thousands of atoms on high-performance hardware.

The ONETEP code [39, 40] is an example for a range of approaches that aim to enable DFT calculations which scale linearly with system size. In order to achieve this goal, it is necessary to do away with explicit references to a plane wave basis set and to the KS

equations/orbitals. These concepts are replaced with a density matrix expanded in a set of non-orthogonal, local orbitals centred on the atoms. A distinctive feature of ONETEP is that even though it does not use plane waves directly, its basis set of localised functions is equivalent to plane waves. This greatly facilitates comparisons with traditional DFT codes. A further requirement for achieving linear scaling is to exploit the fact that systems with a band gap are 'nearsighted', i.e. the local density does not depend on the potential beyond a certain range.

2.4.1 Density matrix formulation of DFT with localised orbitals

In the ONETEP method the concept of Kohn-Sham orbitals is replaced with an equivalent description in terms of the (single-particle) density matrix $\rho(\mathbf{r}, \mathbf{r}')$ given by

$$\rho(\mathbf{r}, \mathbf{r}') = \sum_k f_k \psi_k^*(\mathbf{r}) \psi_k(\mathbf{r}'), \tag{2.48}$$

where the ψ_k are KS orbitals and the f_k are occupation factors. For the sake of simplicity we disregard spin-dependence of the orbitals in this discussion. For the class of systems with a band gap all orbitals up to the Fermi level are doubly occupied with spin up and spin down electrons ($f_k = 1$), while all higher orbitals are empty ($f_k = 0$). As a result of this binary occupation scheme and the fact that the KS orbitals are orthonormal it follows that the density matrix is idempotent, i.e. $\rho^2 = \rho$. The local electron density can be recovered from the diagonal elements of the density matrix, since

$$n(\mathbf{r}) = 2 \sum_k f_k \psi_k^*(\mathbf{r}) \psi_k(\mathbf{r}) = 2\rho(\mathbf{r}, \mathbf{r}), \tag{2.49}$$

where the factor of 2 accounts for the double occupation of the orbitals due to spin-degeneracy. In the density matrix framework the total energy is obtain by tracing the associated operator with the Hamiltonian, namely

$$E = 2 \cdot \mathrm{tr}\left(\hat{\rho}\hat{H}_{\mathrm{KS}}\right) - E_{\mathrm{DC}}[n], \tag{2.50}$$

where E_{DC} accounts for double counting in the Hartree and xc terms. This form of the energy suggests an alternative approach to DFT that does not reference the KS orbitals explicitly, i.e. to minimise the energy given by the trace formula with respect to the density matrix. During this minimisation it has to be ensured that the total number of electrons N is conserved. This is achieved by constraining the trace of the density matrix:

$$2 \int \mathrm{d}^3 r \rho(\mathbf{r}, \mathbf{r}) = N. \tag{2.51}$$

In addition, the density matrix must satisfy the idempotency constraint such that the system obeys Fermi statistics:

$$\rho^2(\mathbf{r},\mathbf{r}') = \int \mathrm{d}^3 r'' \rho(\mathbf{r},\mathbf{r}'')\rho(\mathbf{r}'',\mathbf{r}') = \rho(\mathbf{r},\mathbf{r}'). \tag{2.52}$$

At this point, it is important to note that even though we have abandoned direct references to KS orbitals, the density matrix still has order N^2 entries. This means that without further approximations, key steps of the calculation like evaluating the total energy (Eq. (2.50)) do not scale linearly. Here, the concept of 'nearsightedness' that was alluded to earlier comes in. It has been shown that for a system with a band gap the density matrix decays exponentially with separation [41–43], i.e.

$$\rho(\mathbf{r},\mathbf{r}') \sim e^{-\gamma|\mathbf{r}-\mathbf{r}'|}, \tag{2.53}$$

at large separations $|\mathbf{r}-\mathbf{r}'|$. This property makes it possible to truncate the density matrix at large separations, making it sparse, and thereby reducing the scaling to order N. However, in order to exploit this kind of locality it is necessary to use a set of local functions to represent the density matrix. Expanded in functions which span the whole system (like KS orbitals or plane waves) ρ would still appear fully dense. Therefore, ONETEP uses so-called non-orthogonal generalised Wannier functions (NGWFs) as its basis set [44]. These functions which we denote by $\phi_\alpha(\mathbf{r})$ are centred on the atoms and are each confined within a cutoff radius R_α (ensuring locality). Expanding the density matrix in terms of the NGWFs (using operator notation for simplicity) yields

$$\begin{aligned}
\rho(\mathbf{r},\mathbf{r}') = \langle \mathbf{r}|\,\hat{\rho}\,|\mathbf{r}'\rangle &= \sum_{\alpha,\beta} \langle \mathbf{r}|\phi_\alpha\rangle\langle\phi^\alpha|\hat{\rho}|\phi^\beta\rangle\langle\phi_\beta|\mathbf{r}'\rangle \\
&= \sum_{\alpha,\beta} \phi_\alpha(\mathbf{r})\langle\phi^\alpha|\hat{\rho}|\phi^\beta\rangle\phi^*_\beta(\mathbf{r}') \\
&\equiv \sum_{\alpha,\beta} \phi_\alpha(\mathbf{r}) K^{\alpha\beta}\phi^*_\beta(\mathbf{r}'),
\end{aligned} \tag{2.54}$$

where the last line introduces the density kernel $K^{\alpha\beta}$ and the functions with upstairs indices denote duals of the NGWFs, satisfying $\langle\phi_\beta|\phi^\alpha\rangle = \delta^\alpha_\beta$. Since the NGWFs are not chosen to be orthogonal the duals are not simply equal to the NGWFs themselves but rather result from a transformation of the basis with the inverse of the NGWF overlap. Because the NGWFs form a set of localised basis functions it is possible to exploit the exponential decay of the density matrix by discarding entries of the density kernel corresponding to NGWFs further apart than some cutoff radius R_K. This makes $K^{\alpha\beta}$ a sparse matrix which can be processed with a computational effort that scales order N. The resulting approximation is controlled both by R_K and the NGWF cutoff radii R_α. Linear-scaling calculations with kernel truncation should be converged with respect to these parameters.

2.4.2 Optimisation procedure

The approach to minimising the energy taken by ONETEP involves both optimising the (density) kernel and the NGWFs. In principle, one could keep the basis fixed and only optimise the kernel. This has the disadvantage of requiring a large basis set to accurately represent the density matrix. The philosophy of ONETEP is to use a minimal basis set of NGWFs which are optimised in situ in conjunction with the kernel.

To ensure idempotency, the method uses a combination of purification transformations and penalty functionals [45–47]. A purification transformation is a polynomial operation on the density matrix which is designed to push its eigenvalues (i.e. the occupation numbers f_k) towards 0 or 1. Purification only works as long as the eigenvalues are within certain bounds, so an additional method is needed (especially early in the calculation). This is the penalty functional method which adds a functional $P[\rho]$ to the energy to enforce impotency.

The NGWF optimisation requires the NGWFs to be represented as a linear combination of functional primitives, such that the optimisation can be performed by adjusting the expansion coefficients. The ONETEP method uses so-called psinc functions for this purpose. They can be defined as linear superpositions of plane waves on a finite grid, and each psinc is non-zero on exactly one grid point only. In addition, they have the convenient property of being mutually orthogonal. Because of the definition of the psinc functions in terms of plane waves it follows that the NGWFs are also related to plane waves. Hence, switching between plane waves and a real space representation on the finite grid (needed to evaluate the energy) can be efficiently implemented using fast Fourier transforms (FFTs). If the FFTs were performed globally on the whole simulation cell, however, this would lead to a scaling worse than order N. Global FFTs are actually not needed since each NGWF has a strict cutoff and is non-zero only in some small part of the simulation cell. Therefore, the so-called FFT box technique is employed which associates a smaller FFT box with each NGWF [48]. It is centred on this NGWF and contains it together with its overlapping neighbours which is necessary for consistency. With the FFT box technique, ONETEP is able to retain order N scaling for all parts of the evaluation of the density and the Hamiltonian.

2.4.3 LR-TDDFT in ONETEP

The linear-response formalism for TDDFT is also implemented in ONETEP [49]. A number of modifications are necessary to obtain a method that is linear-scaling. These are very much in the spirit of previously described approaches, i.e. avoiding explicit matrix diagonalisations and using a description in terms of density matrices instead of KS orbitals.

Since the minimal set of NGWFs is optimised specifically to represent the occupied space, it will generally only poorly represent the manifold of excited states. To overcome this problem, a second set of NGWFs χ_α is generated to represent the space of low-lying excited states [50]. This is done in a second optimisation procedure after the ground state calculation. The NGWFs ϕ_α representing the occupied states are used in the Hamiltonian to project out the valence manifold and shift it to higher energies. The energy of this conduction Hamiltonian is then minimised with respect to a conduction density kernel and the conduction NGWFs χ_α. A limitation of the method is that the localised conduction NGWFs do not provide a natural basis for higher energy delocalised or even unbound conduction states.

The central object of the linear-scaling approach to LR-TDDFT is the response density matrix

$$\tilde{\rho}(\mathbf{r},\mathbf{r}') = \sum_{\alpha,\beta} \chi_\alpha(\mathbf{r}) R^{\alpha\beta} \phi^*_\beta(\mathbf{r}'), \tag{2.55}$$

with a representation in terms of valence and conduction NGWFs given by the response kernel $R^{\alpha\beta}$. The response density matrix describes a (single-particle) excitation of the non-interacting system as a superposition of transitions from valence to conduction NGWFs. To avoid having to construct the TDDFT matrix appearing in Casida's equation (Eq. (2.43)) out of KS orbitals the problem of finding the low-lying eigenvalues can be rebranded as a minimisation [49]. To perform the minimisation it is necessary to evaluate the action of the TDDFT matrix on the response density matrix. If all components of the Hamiltonian are represented in the set of valence/conduction NGWFs, all references to KS orbitals disappear. In addition, the locality of the basis set means that sparse matrices are obtained in this representation. Hence, it is possible to evaluate the action of the TDDFT matrix with sparse algebra, provided that the response and conduction density matrices can be truncated as well. For many systems this truncation appears to be a reasonable approximation, at least for obtaining low-lying excitations [51, 52], even though a general argument to justify this approach is lacking.

2.4.4 cDFT in ONETEP

The cDFT implementation in ONETEP uses local functions centred on the atoms as projectors to define populations of constrained subspaces. Possible choices for the local functions are pseudo-atomic orbitals or the self-consistently optimised NGWFs themselves. A complication arises from the fact that the local functions are non-orthogonal. It is then necessary to have an appropriate definition of projector duals. Here, an ambiguity arises regarding the question over which function space the duals should be constructed. Possible choices are duals local to each atom, global duals, or duals that are local to each of the constrained

subregions of the given cDFT calculation. The two extreme positions suffer from significant overcounting, and highly non-local behaviour of the population analysis, respectively. A good compromise is the third option, it can also be shown to be 'tensorial', i.e. it ensures that the population analysis is independent of the choice of local basis functions [53]. We have implemented this prescription in ONETEP and employ it for our cDFT calculations on the pentacene system presented in chapter 4. There we also provide a more detailed description of this approach.

Chapter 3

Excitations in organic materials and singlet fission

3.1 Excitons: bound excitations

Electronic excitations in materials with a band gap result from the promotion of electrons out of the ground state into the manifold of states above the band gap. Each electron that is promoted to an excited state leaves a positively charged hole in the ground state manifold. In inorganic semiconductors, such as Si or GaAs, the dielectric constant is fairly large due to the presence of a population of high-mobility charge carriers created by thermal excitation at non-zero temperatures. These screen the Coulomb interaction between electrons and holes very effectively and warrant a description in terms of non-interacting quasiparticles. The quasiparticles essentially behave like free charges, such that the electronic properties of the material can be described in terms of a band structure comprised of single-particle states.

In contrast, organic materials are characterised by a much smaller dielectric constant. As a result, the Coulomb interaction is screened less effectively, and an independent-particle description of excitations is no longer valid. Rather than behaving like free charges, the electron and hole created in an excitation event form a coulombically bound state, called an exciton. Typical binding energies are in the range of a few tenths of an eV. The Coulomb attraction between electron and hole in conjunction with inevitable disorder in most organic materials lead to localisation of the excitons. According to the relative localisation of electron and hole, a distinction is drawn between so-called Frenkel and charge-transfer excitons (details below).

3.1.1 Frenkel excitons

Localised Frenkel excitons have as their defining property that electron and hole essentially occupy the same space, and no significant charge separation (compared to the ground state) is present. In organic molecular crystals this usually means that the exciton is mostly confined to just a single molecular unit. The proximity of the quasiparticles means that the exchange interaction is significant. Hence, relative spin alignment has a marked effect on the energy of Frenkel excitons. To see this we look at a very simplified model which only considers the two electrons in the highest occupied molecular orbital (HOMO) in the ground state configuration. Also, we restrict the Hilbert space to only the HOMO and the lowest unoccupied molecular orbital (LUMO), denoted by $\phi_{\mathrm{H}}(\mathbf{r})$ and $\phi_{\mathrm{L}}(\mathbf{r})$, respectively. A single-particle excitation is then approximated as the promotion of one electron from the HOMO to the LUMO. If the excitation is a spin-singlet with total spin 0 and antisymmetric spin wave function, then, in order to obey Fermi statistics, the spatial part of the two-particle wave function is necessarily symmetric, i.e.

$$\psi_{\mathrm{S}}(\mathbf{r},\mathbf{r}') = [\phi_{\mathrm{H}}(\mathbf{r})\phi_{\mathrm{L}}(\mathbf{r}') + \phi_{\mathrm{L}}(\mathbf{r})\phi_{\mathrm{H}}(\mathbf{r}')]/\sqrt{2}. \tag{3.1}$$

On the other hand, for triplet excitations with total spin 1 and symmetric spin wave functions, we require an antisymmetric spatial wave function

$$\psi_{\mathrm{T}}(\mathbf{r},\mathbf{r}') = [\phi_{\mathrm{H}}(\mathbf{r})\phi_{\mathrm{L}}(\mathbf{r}') - \phi_{\mathrm{L}}(\mathbf{r})\phi_{\mathrm{H}}(\mathbf{r}')]/\sqrt{2}. \tag{3.2}$$

For a spin-independent Hamiltonian the energy difference $E_{\mathrm{S}} - E_{\mathrm{T}}$ is twice the exchange energy J, where

$$J = \int \mathrm{d}^3 r \int \mathrm{d}^3 r' \phi_{\mathrm{H}}^*(\mathbf{r})\phi_{\mathrm{L}}^*(\mathbf{r}')\frac{1}{|\mathbf{r}-\mathbf{r}'|}\phi_{\mathrm{L}}(\mathbf{r})\phi_{\mathrm{H}}(\mathbf{r}'). \tag{3.3}$$

This describes the self-interaction energy of a 'charge distribution' given by the HOMO-LUMO overlap. For localised Frenkel excitons this will be significant, resulting in a large singlet-triplet gap. The energy difference exhibits a downwards trend with increasing size of the molecular units: if HOMO and LUMO are delocalised over a large molecule, the "charge distribution" is more delocalised as well, resulting in a smaller self-interaction energy. For a linear molecule with length ℓ, wave function normalisation requires $\phi_{\mathrm{H}}, \phi_{\mathrm{L}} \sim \ell^{-1/2}$, hence the exchange interaction scales $J \sim \ell^{-1}$ by dimensional analysis.

3.1.2 Charge-transfer excitons

Charge-transfer (CT) excitons are characterised by a spatial separation of electron and hole. One can draw a distinction between intra- and intermolecular CT states according to the localisation of the quasiparticles on the same molecular unit or different units. The overlap

of initial and final orbital of the transition is much smaller for CT excitons due to spatial separation. This means that the exchange energy J and the singlet-triplet gap are usually negligible, especially in the intermolecular case. Using a classical point-charge model the energy of a CT exciton is determined approximately by the band gap E_{gap} and the screened Coulomb interaction of electron and hole [54]:

$$E_{\text{CT}} = E_{\text{gap}} - \frac{1}{\epsilon_r r_{\text{CT}}}, \tag{3.4}$$

with relative dielectric constant ϵ_r and electron-hole separation r_{CT}.

In contrast to the case of Frenkel-like excitations, LR-TDDFT with local functionals tends to perform poorly on CT-like excitations. In particular, energies of CT states are often grossly underestimated [35, 36]. Here, cDFT provides a much more successful alternative, provided it is feasible to formulate an appropriate set of constraints to describe the desired state. It should be kept in mind that the states obtained from cDFT are diabatic states rather than eigenstates in general.

3.2 Singlet fission

Singlet fission (SF) is a process by which a singlet exciton is transformed into two triplet excitons. It has been observed in a range of organic materials [7,8]. SF is an example of multi-exciton generation, since in a material supporting SF, an optical absorption (initially creating one singlet exciton) can yield more than one triplet excitation. The process is of great interest for photovoltaics as it could be employed to build photovoltaic devices that overcome the Shockley-Queisser limit to the efficiency of solar cells with a single junction [55–57].

3.2.1 Basic concept

SF has been observed in organic materials such as polyacenes, carotenoids, and polymers, all of which have photoexcitable sites known as chromophores [7, 8]. In some materials, SF takes place on very rapid timescales, on the order of picoseconds or less, with the fastest rates encountered in molecular crystals.

For the following discussion we denote the ground state of a chromophore with S_0 (closed-shell singlet state), the first excited singlet state with S_1, and the lowest-energy triplet state with T_1. SF does not occur in isolated small-molecule chromophores, it either requires aggregation of small molecules (such as in molecular crystals) or larger molecules with more than one excitation site. A possible rationalisation of this observation is that the two triplets resulting from a SF event have to be accommodated by at least two excitation sites. This

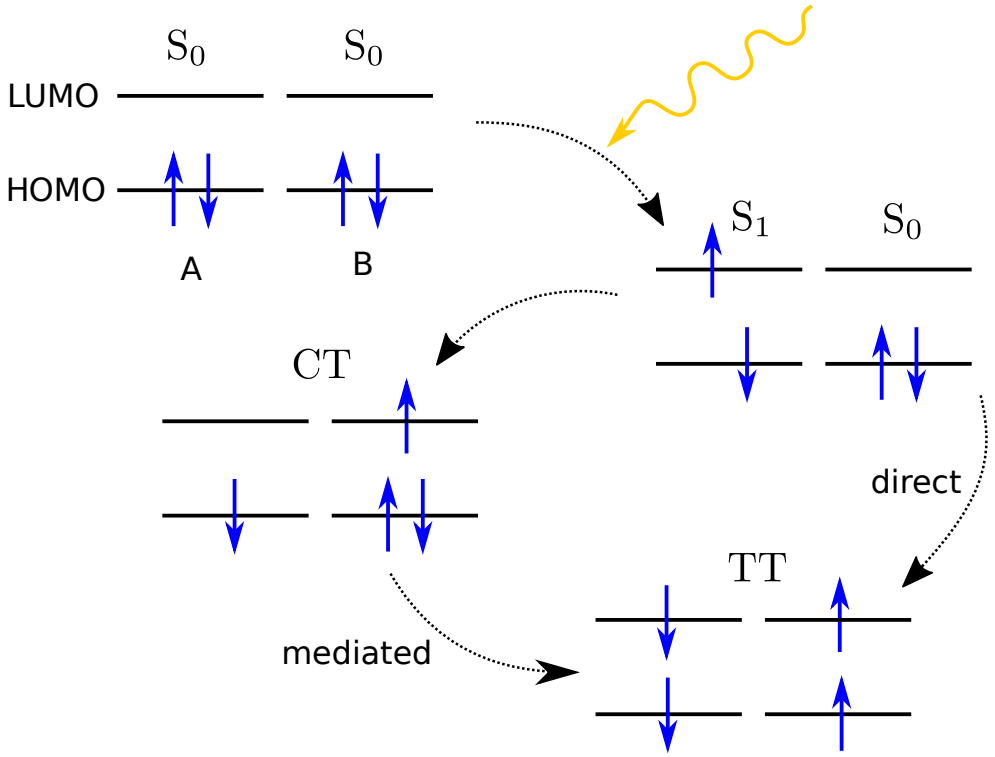

Figure 3.1: Cartoon picture of singlet fission mechanisms using a simplified two-chromophore model.

property of relying not just on a single chromophore, together with the fact that SF is a multi-exciton process, exacerbates the difficulty of theoretical modelling considerably. A very simplified picture can be obtained by just considering two weakly coupled chromophores (Fig. 3.1). We assume that one of the chromophores has been excited to the S_1 state (assumed to be of Frenkel type), while the other one remains in the ground state S_0. The basic SF process is then expressed as a rate equation, namely

$$S_0 + S_1 \overset{k_1}{\rightarrow} {}^1(TT) \overset{k_2}{\rightarrow} T_1 + T_1, \tag{3.5}$$

where k_1, k_2 are rate constants and ${}^1(TT)$ denotes two correlated triplets forming an overall singlet. The latter is required for conservation of spin. Processes which do not conserve spin are strongly suppressed in organic materials without heavy elements that could give rise to significant spin-orbit coupling. The actual SF process corresponds to the first arrow, whereas the second arrow describes a subsequent dissociation of the correlated triplets, resulting in two independent triplet excitons. In general, the reverse process, known as triplet fusion or triplet-triplet annihilation, is also possible. However, when uncorrelated triplets meet, spin statistics tells us that they will only form an overall singlet in a quarter of cases (1 singlet vs 3 triplets). The requirement for favourable energetics is that the energy of the singlet

excited state is at least twice the triplet energy, i.e.

$$E(\mathrm{S}_1) \geq 2E(\mathrm{T}_1). \tag{3.6}$$

If this is the case, then SF does not require additional activation energy (e.g. thermal) in order to occur. The singlet-triplet gap is given by two times the exchange interaction (Eq. (3.3)), as was discussed earlier. Plugging this into Eq. (3.6) yields the condition

$$4J \geq E(\mathrm{S}_1), \tag{3.7}$$

requiring a large exchange energy in relation to the energy of the first singlet state. Both J and $E(\mathrm{S}_1)$ become smaller with increasing size of the chromophore, with $E(\mathrm{S}_1)$ having a stronger dependence on size: J scales like ℓ^{-1} for linear molecules of length ℓ, while a simplistic particle-in-a-box model gives $E(\mathrm{S}_1) \sim \ell^{-2}$. Therefore, it is often possible to achieve more favourable energetics by choosing a larger chromophore. A good example is the singlet-triplet alignment of tetracene versus pentacene. Whereas SF is slightly endothermic for tetracene, it becomes exothermic for the pentacene molecule which has one additional acene unit [7].

Efficient SF also requires that the correlated triplet state $^1(\mathrm{TT})$ is only weakly bound, otherwise dissociation into free triplets would be hampered, and triplet fusion with a subsequent loss of the excitation could become more likely [7]. Since the triplets are thought to reside on different chromophores, they usually are weakly coupled, so this condition is met relatively easily and thus is less restrictive than Eq. (3.6).

At this point it should be stressed that this outline of the SF process relied on a minimal model with a dimer of chromophores. There is increasing evidence that the molecular environment of this dimer can have a very significant impact on the energetics and dynamics of SF. This aspect will be explored further in the discussion of pentacene in this as well as the next chapter.

Relevance to photovoltaics

A SF event following absorption of a photon constitutes multi-exciton generation (MEG), as was mentioned before. This makes SF an interesting candidate process for overcoming the Shockley-Queisser (SQ) limit to the efficiency of photovoltaic cells with a single junction [3]. A single-junction cell has one absorbing material with a fixed band gap. The result is that photons with energies below the band gap cannot be absorbed. Photons with higher energies can be absorbed, though any additional energy above the band gap is quickly dissipated and does not contribute to the output voltage. As a consequence, the efficiency of photovoltaic cells with a single absorbing material exposed to the solar spectrum is limited to about 34%.

This limit could be overcome if it were possible to generate more than one charge pair from high-energy photons, and as we have seen SF enables just that. For a practical implementation of this idea a SF material could be combined with a conventional sensitiser that absorbs low-energy photons. Even though this approach relies on more than one sensitiser material, no current-matching is necessary, unlike in a conventional multi-junction cell. In addition, converting photons into triplet rather than singlet excitons bears the advantage of much longer lifetime of the excitations. This is because radiative decay of triplets is spin-forbidden and therefore slow in organic materials lacking heavy elements. This means that longer diffusion lengths are possible, and radiative losses are reduced [58,59].

3.2.2 Proposed mechanisms

So far, to our knowledge, no theoretical mechanism has been proposed that has been able to fully explain the entire range of experimental observations relating to SF. The reasons for these theoretical difficulties are several: SF occurs in quite different materials, on timescales spanning some orders of magnitude, it is a multi-exciton process, and it relies on aggregation of chromophores. Most experimental techniques that have been applied to the investigation of SF are based on optical absorption and emission. As a consequence, intermediate states that may be involved in the process but are optically dark (like CT states), are not directly observable. This is a major impediment to progress in understanding since the debate mainly revolves around the relevance and characteristics of intermediate states.

We now briefly outline the two main mechanisms that have been suggested to contribute to SF. A more in-depth discussion of the matter for pentacene follows in the next section. For the sake of clarity, we stick to the minimal dimer picture considering only a pair of chromophores (cf. Fig. 3.1).

Direct fission

We consider the dimer of chromophores (labelled A and B) to be in the ground state S_0S_0 initially. Now, photoabsorbtion promotes chromophore A to the optically bright singlet state S_1, yielding S_1S_0. The rate of direct (i.e. first order) transitions from this photoexcited state to the correlated triplet pair is then determined by the matrix element $\langle {}^1(\mathrm{TT})|\hat{H}|S_1S_0\rangle$. A transition rate can be obtained from Fermi's golden rule, yielding

$$w(\mathrm{SF}) = \frac{2\pi}{\hbar}|\langle {}^1(\mathrm{TT})|\hat{H}|S_1S_0\rangle|^2\rho(E), \tag{3.8}$$

with the density of final states factor $\rho(E)$ implicitly accounting for the Franck-Condon weighting of vibrational transitions. This rate tends to be relatively small since the matrix

element contains overlap densities of orbitals mostly localised on different chromophores [7]. An intuitive interpretation of the direct fission process would be to imagine that the excited electron from the chromophore A is transferred to chromophore B, with a simultaneous backtransfer of an electron from B to A, and spins of the transferred electrons chosen such that the correlated triplet is the result.

CT-mediated fission

Eq. (3.8) only takes the first-order coupling of initial and final states into account. In principle, intermediate states can significantly contribute to the transition rate. In the minimal dimer model there are two more states which can be expected to contribute to SF by virtue of their energetic alignment: the lowest two intermolecular CT states. Starting in the ground state of the chromophore pair, they result from the transfer of one electron from chromophore A to B or vice versa. Taking CT states into account, additional contributions to the transition amplitude of the form $\langle {}^1(\mathrm{TT})|\hat{H}|\mathrm{CT}\rangle\langle \mathrm{CT}|\hat{H}|\mathrm{S_1S_0}\rangle/\Delta E$ enter at the second order of perturbation theory. The denominator ΔE denotes the energy difference between CT states and initial/final states. In the picture of the intuitive interpretation given for direct fission, the process is now split into two virtual transitions: first the excited chromophore donates an electron, creating a CT state, and subsequently an electron with different spin is transferred back. In contrast to direct fission, each step in the process involves the transfer of a single electron only, meaning that the total contribution can still be very significant compared to the direct amplitude. The relative importance of the direct and the mediated mechanism depends crucially on the energetic alignment since ΔE divides the product of matrix elements. If the CT states are sufficiently close in energy to the singlet and correlated triplet, the CT-mediated pathway can dominate the transition amplitude.

3.3 Fission in crystalline pentacene

The pentacene molecule ($C_{22}H_{14}$) belongs to the class of polyacenes. Its structure can be described as five linearly fused benzene rings (Fig. 3.2a). The molecule forms molecular crystals which appear in at least four slightly different polymorphs [61]. The crystal structures are made up of layers of roughly vertically oriented pentacene molecules in a herringbone configuration. The unit cell consists of two molecules with parallel long axes, and a rotational offset between the two pentacene units around the long axis (Fig. 3.2b). The polymorphs differ mainly in the stacking of the herringbone layers. However, experiments have shown that the physics of the excitations is only marginally dependent on the specific polymorph.

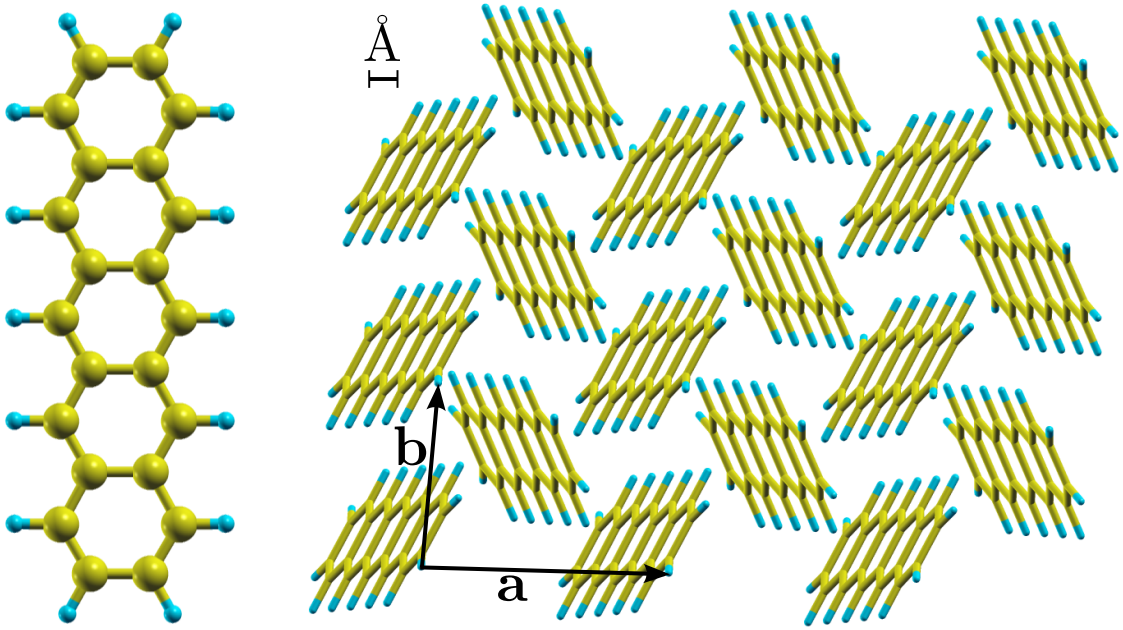

Figure 3.2: The pentacene ($C_{22}H_{14}$) single molecule and molecular crystal (S-phase [60]). The unit cell contains two molecules. The third lattice vector **c** points out of the page.

Solid pentacene has been observed to exhibit rapid SF with very high yield [57]. This, together with its simple molecular and crystal structure, makes it a very appealing material for experimental and theoretical investigations of SF. Accordingly, it has been widely studied in the literature. However, to our knowledge, no definite conclusion has been reached about the detailed mechanism by which SF occurs in pentacene. The rest of this section is dedicated to outlining the current state of the debate about various experimental findings and their theoretical interpretations.

3.3.1 Experimental investigations

Highly time-resolved photoinduced absorption measurements have observed the kinetics of singlets and triplets in bulk pentacene and thin-films. It has been established that SF in pentacene occurs on ultrafast timescales of less than 100 femtoseconds [62, 63]. The literature largely agrees on assigning an energy of approximately 1.83 eV to the excited singlet S_1 [64,65], and roughly 0.86 eV to the triplet state T_1 [66]. Hence $2E(T_1) = 1.72$ eV, fulfilling the energetic condition Eq. (3.6) with an exoergicity of about 0.1 eV. Less agreement exists regarding the energetic alignment of the intermolecular CT states. While earlier measurements put the CT states at least 0.3 eV above the excited singlet [67, 68], more recent measurements [69–71] suggest energies of $\sim$ 1.9 eV, just slightly above the singlet. These experiments are supported by high-level theoretical calculations employing many-body perturbation theory [72, 73], as well as our own results obtained with cDFT which are outlined in the next chapter.

Recent time-resolved two-photon photoemission measurements indicate that the correlated triplet pair ^{1}(TT) is energetically resonant with S_1 [63]. The method first photoexcites the sample, subsequently applies a high-energy ionization pulse, and finally analyses the energies of the resulting photoelectrons. It was found that a feature with a photoelectron energy of 0.11 eV above the signal assigned to T_1 rises essentially simultaneously with S_1 (within the 20 fs time-resolution). This feature was identified as the correlated triplet pair ^{1}(TT). The authors interpreted the data as showing that ^{1}(TT) is energetically resonant with S_1 and strongly coupled to it via an empirically derived matrix element of 330 meV.

3.3.2 Debate about CT intermediates

Knowledge about the precise alignment of the CT excitons and the singlet is crucial to determine the importance of the CT-mediated mechanism compared with the direct mechanism, as was discussed earlier. Put differently, the closer the states lie in energy, the more mixing

of the CT states into the optically excited bright state that precedes the fission event is expected. We now give a brief account of the different theoretical proposals, ordered according to the relevance they assign to CT excitons in the SF process.

CT states not involved

It has been proposed that CT-like states do not play a significant role in SF [74–78]. Rather, it has been claimed on the basis of high-level quantum chemistry calculations that single pentacene molecules can accommodate a dark state D with multi-exciton character which is close in energy to the excited singlet S_1. After photoexcitation, the excited molecule is supposed to form a temporary bound state with a neighbour (a so-called excimer). During the formation of this bound state the molecules approach each other, leading to a conical intersection of the potential energy surfaces of D and S_1, facilitating a crossover from S_1 to D. The assumption that CT states do not play a role is supported by TDDFT calculations which seem to show that the lowest bright state of a pentacene decamer does not exhibit any significant electron-hole separation [78]. This assertion runs counter to recent experimental results [69–71] and calculations based on higher-level theory than DFT [72,73]. The excimer mechanism has also been critisised on grounds of yielding insufficient coupling strengths (1-5 meV) to explain the rapid SF observed in pentacene [79].

High-lying CT states

A range of other proposals acknowledges the likely involvement of CT states in SF [79–81]. The authors calculate couplings in DFT based on overlaps of KS orbitals of the relevant states with the KS Hamiltonian. The energies are either directly taken from experiment, or adjusted to match experimental values. This includes putting the CT energy significantly above the energy of the singlet Frenkel exciton, in accordance with early experimental results. The proposals argue that the primary driver of SF is coupling mediated by these high-lying CT states, dubbed a 'super-exchange' mechanism. However, the effective coupling strength between initial and final states derived from this mechanism lie in a range of only 10-100 meV [79, 80, 82]. This is still insufficient to explain the rapid sub-20-fs coherent rise of the multi-exciton state observed in photoemssion experiments, implying a matrix element of 330 meV [63].

Low-lying CT states

Recent theoretical and experimental results challenge the notion that the CT states are significantly removed in energy. Measurements based on spectroscopic generalised ellipsometry find an electronic excitation centred at 1.887 eV [71]. From the polarisation-dependence of the excitation the authors concluded that it may have very significant intermolecular CT character. The absorption peaks seem to occur at polarisation directions that roughly coincide with connecting lines of neighbouring pentacene molecules in the herringbone lattice. This interpretation is supported by electron energy-loss spectroscopy [69, 70] and theoretical calculations of the absorption spectrum using many-body perturbation theory in the GW/BSE formalism [72, 73]. The authors of the latter results show that the calculated low-lying singlet excitations in molecular crystals of pentacene are delocalised over neighbouring molecules and exhibit significant intermolecular electron-hole separation. In the next chapter we present our own cDFT calculations of CT energies, adding even further support to this body of work. We conclude that recent results suggest that intermolecular CT energies in pentacene are significantly lower than previously assumed, challenging the notion that S_1 is predominately of Frenkel type. A crucial consequence is that the CT-mediated contribution to SF should be revised upwards, potentially closing the current gap between experiment and theory.

3.3.3 The role of vibrations

It has become increasingly apparent that the interplay between electronic states and molecular vibrations is a crucial element of a satisfactory account of the SF process. Lines of evidence include theoretical arguments that show that electronic couplings between the initial and final states of fission vanish for symmetric dimers in the ground-state geometry [7, 83]. This hints at the necessity of symmetry-breaking nuclear motion to facilitate fission. In addition, ultrafast spectroscopy experiments strongly suggest a significant role of vibrations and nuclear motion in SF dynamics [84, 85]. This has motivated theoretical work aimed at constructing joint models of electronic and vibrational degrees of freedom and their interaction [79, 81].

In chapter 5 we use DFT to parametrise the vibronic coupling Hamiltonian of a molecular dimer of pentacene. This then forms the basis for many-body wave function calculations of the electronic-vibrational dynamics, providing detailed insight into the fission process.

3.4 Fission in molecular dimers

More recently, experiments have demonstrated that fast and efficient SF occurs in several covalently-linked dimers of pentacene [86–89].

These molecules are very good systems for the exploration of SF physics, for several reasons. For one, since they are physical dimers, the dimer model is not just a crude approximation. This limits both the total number of electronic configurations that a theoretical model needs to consider, as well as the complexity of electronic structure calculation per state due to the relatively small total number of atoms to consider. In addition, the geometrical structure of covalent dimers is quite well-defined, obviating the need to potentially consider various defect structure that can arise in molecular crystals [90]. Furthermore, with covalent dimers it is possible to systematically explore the influence of the electrostatic environment by placing the dimers in different solvents. This is particularly interesting in relation to the involvement of CT states, which exhibit strong electrostatic environment interactions.

Fission in covalent dimers will be addressed in detail in chapters 5 and 6. This includes an in-depth review of experimental results which are then related to electronic structure and vibrational models.

Chapter 4

Charge-transfer in crystalline pentacene

As discussed in the previous chapter, intermolecular charge-transfer (CT) states spanning nearest-neighbour molecules are thought to play a central role in the ultrafast SF process in pentacene and similar molecules [79–81, 91]. In molecular crystals, neighbouring pairs of molecules (dimers) undergoing charge-transfer are embedded in a complex molecular environment where screening and hybridisation effects are important.

CT states are difficult to access with experimental techniques as they are optically dark, making it challenging to measure accurate excitation energies [64, 92]. They also pose a challenge to electronic structure theory, as alluded to in the previous chapter. For example, linear-response time-dependent DFT with local exchange is known to perform poorly on CT-like states, severely underestimating their energies [35]. This stems from the fact that local functionals are unable to describe the long-ranged electron-hole interaction correctly, a problem that is related to, and which compounds, the well-known band-gap error of the underlying ground-state DFT calculation. A possible remedy is the use of long-range corrected functionals with asymptotically correct exchange [25]. However, this comes at the expense of introducing additional parameters and of a greatly increased computational cost. It is thus desirable and timely to construct a low-cost method that scales well to large system sizes and complex environments, and which simultaneously describes the electrostatic and quantum mechanical features of CT states with reasonable accuracy.

Here, we make use of constrained DFT [93–96] in combination with linear-scaling DFT (ONETEP), applying it to intermolecular charge-transfer in two nearest-neighbour dimers taken from the pentacene crystal structure. The cDFT method has been applied to a wide variety of molecular systems, to date, in the context of CT excitation energies [97–100], electronic couplings [101–103], electron transfer [104–107] and molecular dynamics [108,109].

A largely unresolved issue in this context, however, is that of achieving supercell convergence of CT excitations in extended models suitable for capturing the screening and hybridisation effects encountered in realistic systems. A solution to this problem, such as the one we propose here, is then readily transferable to a range of complex systems of technological interest, not only in the context of photovoltaics, but also organic electronics [1, 110, 111] and spintronics [112].

In any implementation of cDFT a certain amount of ambiguity arises from the choice of how one defines the electron populations of groups of atoms and molecules of the constrained system. In ONETEP the atom-centred NGWFs provide a natural way of defining subspaces of the system associated with atom groups and their respective electron populations. However, subtleties arise from the non-orthogonality of the NGWFs. Our approach to the problem is presented in the following section. An alternative implementation of cDFT in the context of linear-scaling has been described in Refs. [113, 114].

We calculate CT energies for the dimers in isolation, and we subsequently include screening effects by embedding such dimers in a small cluster of neighbours, and in supercells of the crystal. Supercell calculations allow us to approach the infinite limit using a correction scheme that eliminates the spurious dipole-dipole interactions between periodic images of the simulation cell. The only inputs required for this correction are the intrinsic dipole of the CT configuration and the dielectric tensor of the crystal. The latter is obtained from a density functional perturbation theory (DFPT) calculation [115]. We find that a single parameter, fit to the results of a series of calculations on different supercells, is sufficient to correct for the overestimation of electrostatic screening as a result of the aforementioned band-gap problem of DFT. The isolated calculations facilitate a comparison of the cDFT method with higher-level theory results from the literature [116]. In addition, comparison between clusters and the infinite limit enables us to directly confirm the validity of the cluster approximation.

4.1 Subspace-consistent constrained DFT

This section deals with our approach to cDFT in the context of the ONETEP linear-scaling formulation of DFT, and the specific issues that need to be considered. First, we remind ourselves of the original definition of the cDFT problem in terms of the real-space charge density:

$$W = E_{\mathrm{DFT}} + \sum_k V_k \left(\int \mathrm{d}^3 r w_k(\mathbf{r}) n(\mathbf{r}) - N_k \right), \tag{4.1}$$

where we have left out the spin indices for simplicity. In ONETEP we have the NGWFs at our disposal, a set of atom-centred functions optimised in-situ to provide a good representation of the charge density of the system under consideration. Exploiting these functions in cDFT opens up the opportunity to avoid some of the arbitrariness otherwise inherent in the definition of the weighting functions w_k. To this end, we first have to reformulate the cDFT functional in terms of the density matrix $\hat{\rho}$, i.e.

$$W = E_{\mathrm{DFT}} + \sum_k V_k \left(\mathrm{Tr}[\hat{P}_k \hat{\rho}] - N_k \right). \tag{4.2}$$

As before, the V_k are Lagrange multipliers that enforce occupancy targets N_k on chosen constrained regions or sites in the system. However, instead of weighting functions we now have projection operators $\hat{P}_k$ acting on the density matrix which yield site occupation numbers via the trace operation. We remind the reader that $\mathrm{Tr}[\hat{\rho}] = N$, where N is the total number of electrons, i.e. we obtain the total electron number if the projector is the identity. Similarly, with an operator that projects down to a subspace (or site) we obtain a definition of the occupancy of said site. The sites in question may, generally, be atoms, groups of atoms or entire molecules. For example, if one aims to describe an intermolecular CT state, each of the two molecules involved constitutes a site. The Lagrange multipliers V_k act as artificial constraining potentials that cause charge to move around the system (cf. Fig. 4.1a). These potentials are optimised in-situ, via a further conjugate gradients algorithm nested between kernel optimisation and NGWF optimisation, and iterated until the population targets N_k for the chosen sites are met. In the case of intermolecular CT states, these targets are, respectively, one fewer charge on the donor molecule and one additional charge on the acceptor, relative to the ground state.

At this point we can naturally incorporate the optimised basis provided in ONETEP by defining the site projectors in terms of NGWFs [117]. In doing so we encounter a number of issues which stem from the non-orthogonality of the NGWF basis [118, 119]. Our aim is to formulate a definition of the site projectors that addresses these issues. To illustrate the problem, we first consider the following naive (and incorrect) definition,

$$\hat{P}_k = \sum_{\alpha \in I_k} |\phi_\alpha\rangle \langle\phi_\alpha| , \tag{4.3}$$

where I_k denotes the set of NGWF indices associated with the atoms constituting site k. Defined like this $\hat{P}_k$ is not even a projection operator since it fails to be idempotent:

$$\hat{P}_k^2 = \sum_{\alpha,\beta \in I_k} |\phi_\alpha\rangle\langle\phi_\alpha|\phi_\beta\rangle\langle\phi_\beta| = \sum_{\alpha,\beta \in I_k} |\phi_\alpha\rangle S_{\alpha\beta}\langle\phi_\beta| \neq \hat{P}_k. \tag{4.4}$$

Due to the non-orthogonality of the NGWFs, their overlap matrix $S_{\alpha\beta}$ differs from the identity, upsetting the idempotency relation. A proper definition needs to make reference

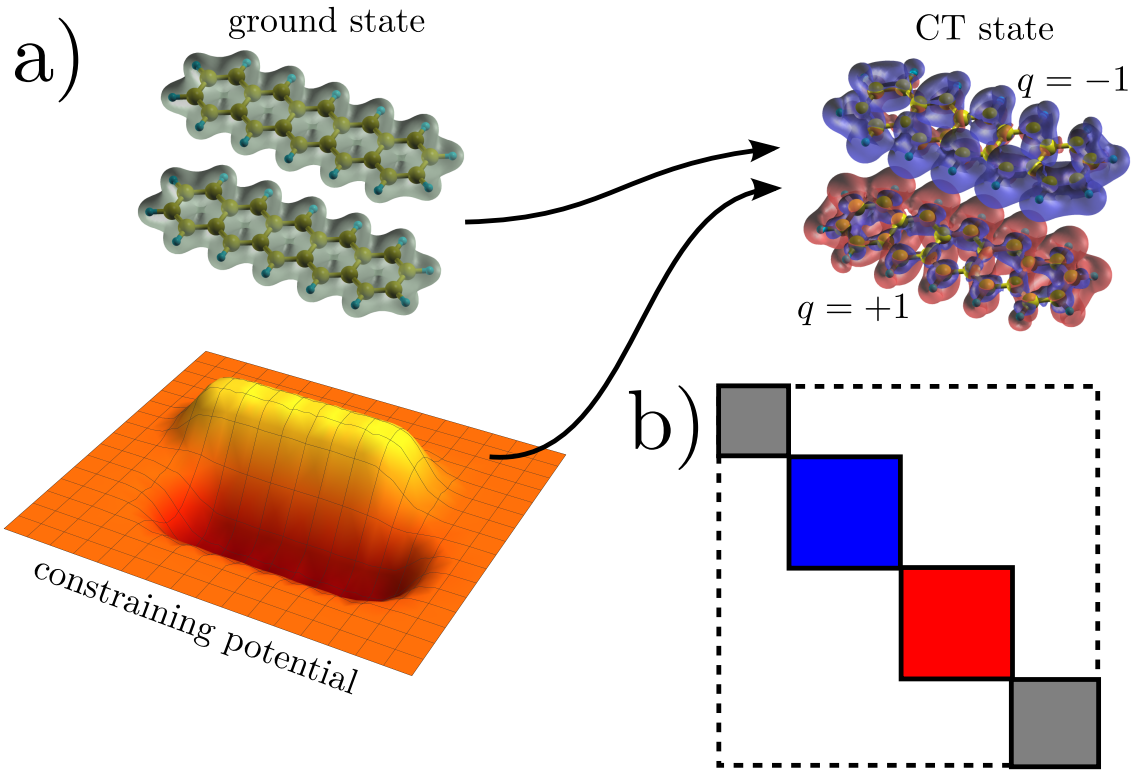

Figure 4.1: a) Schematic of the cDFT scheme used in this work: A nonlocal constraining potential (illustrated by a 2D potential energy surface) constructed from atom-centred functions is applied to the single-electron density matrix. This causes charge to redistribute to obey chosen population constraints, and allows the description of CT excitations within the framework of standard DFT. b) Block scheme of truncated NGWF overlap matrix to ensure site-localisation of contravariant duals. Blue and red denote the constrained sites, grey the remaining system.

to the contravariant duals $|\phi^\alpha\rangle$ of the NGWFs. We write them with a superscript instead of the subscript used for the standard covariant functions, and their defining relation is

$$\langle \phi^\alpha | \phi_\beta \rangle = \delta^\alpha_\beta, \tag{4.5}$$

for all indices α and β. Using the concept of duals we can attempt a more promising definition,

$$\hat{P}_k = \sum_{\alpha \in I_k} |\phi^\alpha\rangle \langle \phi_\alpha| . \tag{4.6}$$

This expression actually defines a projection operator since

$$\begin{aligned} \hat{P}_k^2 &= \sum_{\alpha,\beta \in I_k} |\phi^\alpha\rangle\langle\phi_\alpha|\phi^\beta\rangle\langle\phi_\beta| \\ &= \sum_{\alpha,\beta \in I_k} |\phi^\alpha\rangle \delta^\beta_\alpha \langle\phi_\beta| \\ &= \sum_{\alpha \in I_k} |\phi^\alpha\rangle\langle\phi_\alpha| \quad = \quad \hat{P}_k. \end{aligned} \tag{4.7}$$

If the NGWFs constituted an orthonormal basis the duals would simply be identical to the NGWFs. Due to the non-orthogonality the expansion of the duals in the original basis involves the inverse of the NGWF overlap matrix $S_{\alpha\beta}$:

$$|\phi^\alpha\rangle = \sum_\beta |\phi_\beta\rangle \left(S^{-1}\right)^{\beta\alpha}. \tag{4.8}$$

Then we have

$$\begin{aligned} \langle \phi^\alpha | \phi_\beta \rangle &= \sum_\gamma \langle \phi_\gamma | \phi_\beta \rangle (S^{-1})^{\gamma\alpha} \\ &= \sum_\gamma S_{\gamma\beta} (S^{-1})^{\gamma\alpha} \\ &= \sum_\gamma S_{\beta\gamma} (S^{-1})^{\gamma\alpha} \quad = \quad \delta^\alpha_\beta, \end{aligned} \tag{4.9}$$

where we have used the symmetry of the NGWF overlap matrix for real-valued NGWFs. Given that the overlap and inverse overlap matrices can both be made sparse by appropriately-chosen truncation, it is possible to construct the inverse in linear-scaling computational effort using a sparse matrix implementation of Hotelling's algorithm [120].

We can see from Eq. (4.8) that the duals defined in this way do not generally maintain the localisation of their corresponding NGWFs. Hence, duals of NGWFs belonging to one constrained site will in general extend beyond that same site. This presents a problem for use in cDFT since it implies that site projectors and thereby the constraining potentials act non-locally on the charge density, blurring the lines between what constitutes a donor,

acceptor or unconstrained region. This is extremely problematic when using a fixed set of projectors since the fixed projector duals do not maintain their orthogonality with the changing NGWFs during optimisation. As a result, site populations become contaminated by charge densities from other sites and/or unconstrained regions. Appropriate localisation of the duals, to the region of the system of interest for defining a site, is therefore desirable. Eq. (4.8) constitutes the case of fully delocalised duals. At the other extreme one could choose to define the duals on a per-atom basis which would ensure that the duals maintain the localisation of the NGWFs. However, this choice suffers from significant overcounting since duals of one atom have non-zero overlap with NGWFs of neighbouring atoms. Between these two extremes the third option is to define duals on a per-site basis which achieves a good compromise between localisation and accurate population counting.

This can be achieved by suitably truncating the NGWF overlap matrix before its inversion [53]. We introduce the following version of the overlap matrix with a 'site-block' scheme imposed on the sparsity,

$$O_{\alpha\beta} = \begin{cases} S_{\alpha\beta} = \langle \phi_\alpha | \phi_\beta \rangle & \text{if } k(\alpha) = k(\beta) \\ 0 & \text{otherwise} \end{cases} \tag{4.10}$$

Here the function $k(\alpha)$ maps an NGWF index to the index of the constrained site it belongs to. For the purpose of this definition the NGWFs outside any of the constrained sites constitute a single, unconstrained site, ensuring that $k(\alpha)$ is well-defined over its entire domain. The matrix $O_{\alpha\beta}$ has a block-diagonal form as illustrated in Fig. 4.1b for a constrained pentacene dimer that is part of a larger crystal. Once this matrix has been inverted, it retains the same block pattern of sparsity, meaning that subspace duals are defined as a linear combination of only those NGWFs on the same constrained site:

$$|\phi^\alpha\rangle = \sum_\beta |\phi_\beta\rangle \left(O^{-1}\right)^{\beta\alpha}. \tag{4.11}$$

When the sites are defined in self-contained manner, thereby, bi-orthogonality is unavoidably lost between NGWFs and duals localised to different sites, in the event that these sites overlap to some degree. This carries the disadvantage the sum of charges over a set of such sites, covering the system, may not equal the true total charge. For well-separated donor and acceptor regions such as in the system at hand, any overestimation of site charge due to the latter effect is insubstantial in comparison to the dramatic overestimation incurred by using delocalised duals. On the other hand, even when the donor and acceptor regions do overlap substantially, unlike methods employing fully delocalised duals our approach ensures that the constraining potentials remain fully localised to their respective regions, with a smooth, non-oscillatory transition at the boundary.

An important consideration in devising the cDFT procedure is which NGWFs the projectors should be constructed from. The choice we make here is to use a set of NGWFs from a converged ground state calculation which are kept fixed throughout the cDFT run. One could consider updating the projectors as the NGWFs change during the cDFT optimisation. Only this would guarantee that the projectors are able to pick up the full charge distribution of the cDFT configuration without any 'leakage' or double counting. However, the major drawback of this choice is that it makes the optimisation problem somewhat ill-posed. This is because the changing projectors mean that the optimisation objective does not stay fixed during cDFT, making proper convergence very difficult. Using fixed NGWFs from a converged ground state calculation has been shown to work well, provided that the projectors are well-localised to their respective sites, as we explore in the next paragraph.

In order to obtain energies of CT excitations, we first perform a ground state DFT calculation. This yields both a total energy for the ground state and a set of converged ground-state NGWFs which are subsequently used as cDFT projectors. To define the population targets for the cDFT run we simply add ± 1 to the ground state populations of the appropriate sites (acceptor: $+1$; donor: -1). The difference between the constrained total energy and the ground state energy yields the (vertical) CT excitation energy. Since we are interested in ultrafast processes like singlet fission where nuclear relaxation in the excited state is less significant, we restrict our attention to vertical excitation energies. In general, a geometry optimisation in the excited state would be required in order to correctly describe longer-lived CT states.

4.2 Computational Details

For all calculations we employ the LDA functional and norm-conserving pseudopotentials. The energy cutoff is chosen as 750 eV. We use 1 NGWF per hydrogen atom and 4 NGWFs per carbon atom. For the localisation radius of the NGWFs a value of 10 Bohr is chosen. Using these parameters, the total energy is converged to 1 meV/atom at 10 Bohr NGWF radius compared to 14 Bohr, and to around 25 meV/atom at 750 eV cutoff compared to 1250 eV. All NGWFs are initialised to pseudoatomic orbitals [121] and then optimised in-situ in terms of the underlying psinc basis. The density kernel $K^{\alpha\beta}$ is not truncated in these calculations as all systems are small enough that sparse matrix algebra is only a minor component of the total computational effort. For the later DFPT calculations, we utilise the CASTEP plane-wave DFT code [122] with the same pseudopotentials and cutoff energy. The DFPT calculations are performed with 12 k-points, corresponding to a maximum k-point spacing of 0.05 1/Å.

Configuration	our method	CASPT2/CASSCF	GW/BSE
Herringbone 1	2.04	2.22 [116]	1.92 [116]
Herringbone 2	2.72	2.55 [116]	2.60 [116]
Parallel	2.61	3.03 [116]	2.45* [116]

Table 4.1: CT energies (eV) of isolated dimers, comparing our results with higher-level theory. The authors of Ref. [116] identify the excitation marked by an asterisk as a third locally excited state dominated by transitions between the frontier orbitals of the monomers. However, in a dimer there can only be two states of this kind. Hence, we concluded that the excitation does in fact have CT character.

The S-phase molecular crystal structure considered here has two molecules per primitive cell and triclinic ($P-1$) space group symmetry. The lattice parameters are given by $a = 7.90$ Å, $b = 6.06$ Å, $c = 16.01$ Å, and $\alpha = 101.9°$, $\beta = 112.6°$, $\gamma = 85.8°$ [123]. Optimised molecular geometries are taken from Ref. [60] in order to facilitate comparison of our calculations with Ref. [116] where high-level CASPT2/CASSCF and GW/BSE calculations were performed using the same geometries.

For calculations on isolated dimers and clusters we employ open boundary conditions. This is achieved by putting the dimers in a large simulation box and truncating the Coulomb interaction at large distances to eliminate electrostatic interactions between periodic images [124]. The calculations on supercells of the pentacene crystal use periodic boundary conditions.

4.3 Dimer & cluster calculations

The molecular geometries of the 'herringbone' dimer and the 'parallel' dimer are shown in Fig. 4.2. The herringbone dimer represents the unit cell of the pentacene crystal. While the long axes of the molecules are mostly aligned, there is a rotational offset around the same long axis between the units. In particular, this means that the two units in the herringbone dimer are not related by symmetry.

In the parallel dimer, on the other hand, the pentacene molecules belong to the same sublattice of the crystal and are related by a translation along lattice vector **b** (cf. Fig. 3.2). As a result the molecular planes of the molecules are parallel. The translational correspondence together with the inversion symmetry of single pentacene molecules mean that the parallel dimer has an inversion centre, i.e. the units are symmetry-equivalent.

First, we obtain CT energies for the dimers in isolation. The results are summarised in Fig. 4.2. The most striking aspect is the significant energy gap between the two CT configurations in the herringbone dimer due to their symmetry-inequivalence, as elaborated in the

Configuration	isolated (2 mol)	4-mol cluster	10-mol cluster
Herringbone 1	2.04 (0.80)	2.16 (0.73)	2.00 (0.68)
Herringbone 2	2.72 (0.80)	2.25 (0.73)	2.04 (0.68)
Parallel	2.61 (1.13)	2.35 (0.92)	2.10 (0.87)

Table 4.2: Comparison of CT states for isolated dimers and clusters. The table quotes the excitation energy of the CT state and the HOMO-LUMO gap of the ground state configuration in brackets (in units of eV).

figure. In the parallel configuration the energies are degenerate due to inversion symmetry. The excitation energies for the herringbone configuration are within ∼0.2 eV of literature values obtained with higher-level methods (cf. Table 4.1). For the parallel configuration the discrepancy may be as large as ∼0.4 eV, depending on the method compared to.

We next perform cluster calculations where we surround the dimers with a small cluster of neighbouring molecules fixed in the geometry of the molecular crystal (Table 4.2). The 4-molecule clusters (144 atoms) only include the CT pair and the two shared nearest-neighbour molecules in the **a**-**b**-plane. In the 10-molecule clusters (360 atoms), all nearest-neighbour molecules in the **a**-**b**-plane are included. The results are summarised in Table 4.2. We observe a significant down shift of the mean energy and closing of the relative gaps as the size of the cluster increases. This is driven by a reduction of the gap due to the hybridisation and increased electrostatic screening by neighbouring molecules. It should be noted that the degeneracy of the two parallel dimer CT states is very slightly lifted in the clusters (which do not exhibit exact inversion symmetry), but only within the quoted accuracy. Therefore, we only give a single value for the CT energy.

From the presented set of calculations alone it is difficult to determine whether sufficient convergence to the infinite limit has been reached with the 10-molecule cluster.

4.4 Supercell calculations

We now consider the dimers embedded not in vacuum, but in the natural environment of the molecular crystal. This immediately raises the issue of treating a non-periodic, infinite system in DFT. In practice, one has to use supercell calculations with periodic boundary conditions in order to avoid spurious effects where molecules at the edges of the system are exposed to vacuum. However, these suffer from finite-size errors which are particularly pronounced in the case at hand, as can be seen from the large scatter of 0.1-0.3 eV of the uncorrected CT energies in Fig. 4.3 (blue bars). This is a consequence of the large dipole moments of the CT configurations, resulting in significant dipole-dipole interactions between periodic images. The problem is expected to be even more pronounced in systems with either

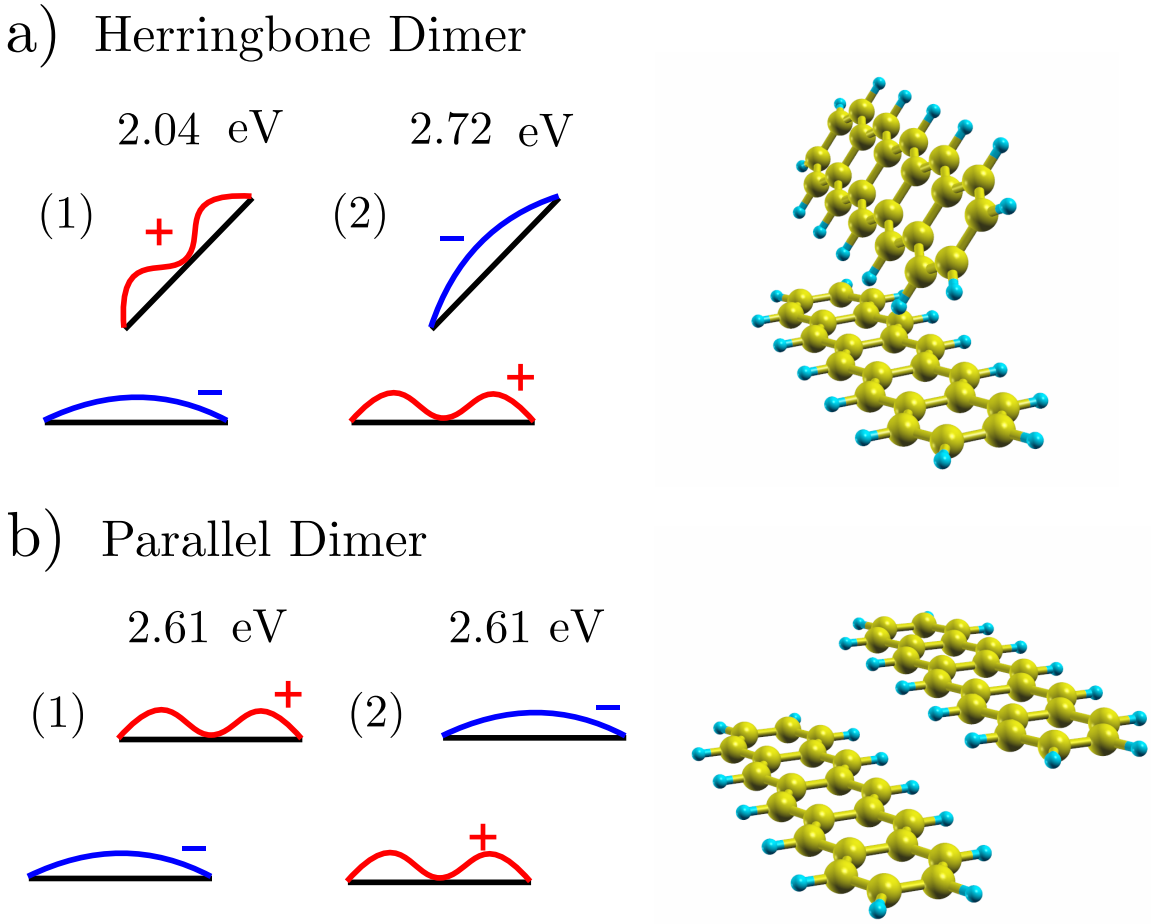

Figure 4.2: Dimer geometries and CT excitation energies from cDFT (quoted in eV). The significant energy gap between the two CT states in the herringbone dimer can be rationalised by considering the different charge distributions of electron and hole, and the geometry. The hole orbital corresponds to the pentacene HOMO which has a node on the long axis of the molecule. The electron orbital (LUMO), on the other hand, does not feature such a node. The partial alignment of the upper molecule with the dipole vector means that the bimodal charge distribution on the upper molecule has a lower Coulomb energy in configuration 1 as compared to configuration 2. In the parallel case the two CT states are related by inversion symmetry and the energies are degenerate.

larger CT-dipoles, like biological photo-reaction centres, or smaller polarisabilities (e.g. due to smaller pi-systems).

4.4.1 Dipole correction: motivation

We address this problem by deriving an energy correction that cancels the spurious interactions to leading order. This makes it possible to obtain energies with a much better degree of convergence with respect to cell size. We apply this correction to a range of calculations using supercells of varying shapes and sizes to demonstrate consistency of the method. The largest supercell considered has dimensions $3 \times 3 \times 2$, or 18 unit cells (1368 atoms).

Mathematically, the general idea can be described as follows:

$$E_{\mathrm{cor}} = E_{\mathrm{DFT}} - E_{\mathrm{dip}}. \tag{4.12}$$

Here, E_{DFT} is the energy obtained from the cDFT calculation, E_{cor} the corrected energy, and E_{dip} the correction term. In the limit of infinite cell size the correction term E_{dip} will tend to zero as the periodic images of the dipoles move further and further apart. This means that both E_{DFT} and E_{cor} converge to the same limiting value as the size of the supercell increases. However, at any finite size of the simulation cell, E_{cor} will be a much better approximation to the limiting value than E_{DFT}.

4.4.2 Makov-Payne and generalisations

Here, we give a relatively brief review of dipole corrections of increasing generality, in preparation for our results which applies to the most general case of non-cubic cells and anisotropic dielectrics. The detailed derivation of this result is then described in the following sections.

Makov & Payne [125] considered the spurious interactions that arise when a periodic calculation is applied to an isolated system. They showed that the dominant term with respect to cell size for an overall neutral system arises from dipole-dipole interactions and has the form:

$$E_{\mathrm{dip}} = -\frac{2\pi}{3V_{\mathrm{cell}}} \cdot |\mathbf{P}|^2, \tag{4.13}$$

where $\mathbf{P}$ is the total dipole moment of the simulation cell. The Makov & Payne result is only valid for cubic cells. It was further shown that after the subtraction of this correction term the energy converges to the infinite limit as $V_{\mathrm{cell}}^{-5/3}$, faster than the uncorrected convergence as V_{cell}^{-1}.

The Makov & Payne correction assumes that the system under consideration is isolated, and hence the electrostatic interactions are mostly mediated through the vacuum. This assump-

tion breaks down if the aperiodic system to be studied is embedded in a crystalline solid, as is the case with CT dimers in a pentacene molecular crystal. Here, the spurious dipole-dipole interactions are screened by polarisation of the bulk crystal. If the bulk crystal can be approximated as an isotropic dielectric, we can apply the phenomenological approach by Leslie & Gillan [126]. Here the dipole-dipole interaction is reduced by the relative permittivity of the bulk crystal, i.e.

$$E_{\text{dip}} = -\frac{2\pi}{3V_{\text{cell}}} \cdot \frac{|\mathbf{P}|^2}{\epsilon}. \tag{4.14}$$

In order to be useful for CT states in pentacene supercells it is necessary to generalise these results to arbitrary cell shapes and, crucially, anisotropic dielectrics [127–129]. To achieve the first step we can employ the following expression by Kantorovich which is valid for general periodic cells and can be obtained by evaluating the Ewald formula for a periodic lattice of point dipoles [130]:

$$E_{\text{dip}} = -\frac{2\eta^3}{3\sqrt{\pi}} \cdot |\mathbf{P}|^2 + \frac{1}{2}\sum_{\alpha,\beta} P_\alpha \psi_{\alpha\beta} P_\beta, \tag{4.15}$$

where η is Ewald's parameter, and

$$\psi_{\alpha\beta} = \frac{4\pi}{V_{\text{cell}}} \sum_{\mathbf{k}\neq\mathbf{0}} \frac{k_\alpha k_\beta}{|\mathbf{k}|^2} e^{-|\mathbf{k}|^2/4\eta^2} - \eta^3 \sum_{\mathbf{l}\neq\mathbf{0}} H_{\alpha\beta}(\eta\mathbf{l}), \tag{4.16}$$

where $\mathbf{k}$ denotes reciprocal lattice vectors, and $\mathbf{l}$ denotes direct lattice vectors. Furthermore, we have

$$H_{\alpha\beta}(\mathbf{y}) = -\delta_{\alpha\beta} h(|\mathbf{y}|) + \frac{y_\alpha y_\beta}{|\mathbf{y}|^2}\left[3h(|\mathbf{y}|) + \frac{4}{\sqrt{\pi}} e^{-|\mathbf{y}|^2}\right], \tag{4.17}$$

with

$$h(y) = \frac{2}{\sqrt{\pi}} \cdot \frac{e^{-y^2}}{y^2} + \frac{\operatorname{erfc}(y)}{y^3}. \tag{4.18}$$

Our aim is to generalise Kantorovich's results for the case of dipoles embedded in an anisotropic dielectric background medium. His derivation relies on the Ewald method which we review in the following section. This is necessary since we later need to generalise the derivation for an anisotropic dielectric background. After that, we provide a detailed derivation of Kanotrovich's correction term which is only sketched out very briefly in Ref. [130]. Finally, we generalise the Ewald method to a general dielectric medium and adapt the terms in Kantorovich's expression for the dipole correction accordingly.

4.4.3 Review of the Ewald method

In preparation for the derivation we review the Ewald summation method for the relevant case of a system of classical point charges. In our exposition we mainly follow Ref. [131].

We consider charges q_i at locations $\mathbf{r}_i$ in a supercell that is repeated on an infinite three dimensional lattice. Each of the repeated cells is associated with a direct lattice vector $\mathbf{l}$. Then the total electrostatic energy of the charges in one cell is given by

$$E = \frac{1}{2} \sum_{\mathbf{l}} \sum_{i} \sum_{j}{}' \frac{q_i q_j}{|\mathbf{r}_i - \mathbf{r}_j + \mathbf{l}|}, \tag{4.19}$$

where $'$ denotes that the sum over j excludes the index i if $\mathbf{l} = \mathbf{0}$. This eliminates spurious self interaction of the charges. The factor of $1/2$ addresses double counting. This can be re-expressed in terms of the electrostatic potential that each charge of the original cell experiences due to the other charges in this cell and all periodic image charges, as follows:

$$E = \frac{1}{2} \sum_{i} q_i \phi_{[i]}(\mathbf{r}_i), \quad \phi_{[i]}(\mathbf{r}) = \sum_{\mathbf{l}} \sum_{j}{}' \frac{q_j}{|\mathbf{r} - \mathbf{r}_j + \mathbf{l}|}. \tag{4.20}$$

The notation $\phi_{[i]}$ denotes the total potential without the contribution of charge i (in the original cell) itself, namely

$$\phi_{[i]}(\mathbf{r}) = \phi(\mathbf{r}) - \phi_i(\mathbf{r}). \tag{4.21}$$

For the next step we switch to a description of the system in terms of charge density. In our case of point charges this can be done using delta functions. The charge density of a point charge q_i is

$$\rho_i(\mathbf{r}) = q_i \delta(\mathbf{r} - \mathbf{r}_i). \tag{4.22}$$

In this description the potential of all charges excluding charge i is then given by

$$\phi_{[i]}(\mathbf{r}) = \sum_{\mathbf{l}} \sum_{j}{}' \int d^3\mathbf{r}' \frac{\rho_j(\mathbf{r}')}{|\mathbf{r} - \mathbf{r}' + \mathbf{l}|}. \tag{4.23}$$

The central issue with the expressions for energy and potential presented so far is that the sum over lattice vectors converges only slowly due to the slow polynomial decay of the Coulomb interaction. Ewald summation addresses this problem by artificially splitting the point charge density into a short-range and long-range part using a Gaussian smearing function. This is accomplished as follows:

$$\rho_i(\mathbf{r}) = \underbrace{q_i \delta(\mathbf{r} - \mathbf{r}_i) - q_i G_\eta(\mathbf{r} - \mathbf{r}_i)}_{\rho_i^S(\mathbf{r})} + \underbrace{q_i G_\eta(\mathbf{r} - \mathbf{r}_i)}_{\rho_i^L(\mathbf{r})}. \tag{4.24}$$

The Gaussian smearing function is given by

$$G_\eta(\mathbf{r}) = \left(\frac{\eta}{\sqrt{\pi}}\right)^3 \exp(-\eta^2 |\mathbf{r}|^2), \tag{4.25}$$

where the (inverse) width is controlled by η which is also known as Ewald's parameter.

In the short-range part ρ_i^S the point charge is screened by a diffuse charge of equal and opposite sign, making it immune to Coulomb interactions at ranges much longer than the width of the Gaussian. The long-range part ρ_i^L however is non-neutral and still 'sees' other charges at greater separations. Even so it turns out to be short-range in reciprocal space since the charge distribution is smooth and non-singular.

Both parts of the charge density cause respective short- and long-range potentials which in turn can be seen as inducing separate contributions to the electrostatic energy,

$$E = \underbrace{\frac{1}{2}\sum_i q_i \phi^S_{[i]}(\mathbf{r}_i)}_{E^S} + \underbrace{\frac{1}{2}\sum_i q_i \phi^L(\mathbf{r}_i)}_{E^L} - \underbrace{\frac{1}{2}\sum_i q_i \phi^L_i(\mathbf{r}_i)}_{E^{\text{self}}}. \tag{4.26}$$

Here the self-interaction energy of q_i with its own diffuse long-range part is included in E^L for later convenience. For overall consistency these additional contributions have to be subtracted from the expression which is accomplished by E^{self}.

In the next step we derive the electrostatic potentials due to the long- and short-range parts of the charge distribution. To this end we need to solve the Poisson equation for the Gaussian smearing function,

$$\boldsymbol{\nabla}^2 \phi_\eta(\mathbf{r}) = -4\pi G_\eta(\mathbf{r}). \tag{4.27}$$

Due to the spherical symmetry of the problem this can be integrated straightforwardly in spherical coordinates, yielding

$$\phi_\eta(\mathbf{r}) = \frac{1}{|\mathbf{r}|}\,\mathrm{erf}(\eta|\mathbf{r}|). \tag{4.28}$$

With this result we can directly write down the short and long-range potentials of a point charge,

$$\phi_i^S(\mathbf{r}) = \frac{q_i}{|\mathbf{r}-\mathbf{r}_i|}\,\mathrm{erfc}(\eta|\mathbf{r}-\mathbf{r}_i|), \tag{4.29}$$

with the complementary error function $\mathrm{erfc}(x) = 1 - \mathrm{erf}(x)$, and

$$\phi_i^L(\mathbf{r}) = \frac{q_i}{|\mathbf{r}-\mathbf{r}_i|}\,\mathrm{erf}(\eta|\mathbf{r}-\mathbf{r}_i|). \tag{4.30}$$

We can see that the complementary error function causes the short-range part to decay quickly to zero. In the long-range part the error function cures the pole of the potential at $\mathbf{r}_i$.

Armed with this result, we are now in a position to write down the short-range potential for the entire lattice,

$$\phi_{[i]}(\mathbf{r}) = \sum_{\mathbf{l}} \sum_j{}' \frac{q_j}{|\mathbf{r}-\mathbf{r}_j+\mathbf{l}|}\,\mathrm{erfc}(\eta|\mathbf{r}-\mathbf{r}_j+\mathbf{l}|), \tag{4.31}$$

as well as the short-range Coulomb energy

$$E^S = \frac{1}{2}\sum_i q_i \phi^S_{[i]}(\mathbf{r}_i) = \frac{1}{2}\sum_{\mathbf{l}}\sum_i{\sum_j}' \frac{q_i q_j}{|\mathbf{r}_i - \mathbf{r}_j + \mathbf{l}|}\,\mathrm{erfc}(\eta|\mathbf{r}_i - \mathbf{r}_j + \mathbf{l}|). \tag{4.32}$$

The expression we obtain is identical to the standard Coulomb energy, except for the additional factor erfc which truncates long-range interactions between charges. Therefore, E^S is efficiently calculable as a sum in real space over lattice vectors close to the origin of the periodic system.

We can also obtain the self energy from the expression for the long-range potential, using the limit $\lim_{x\to 0}\mathrm{erf}(x)/x = 2/\sqrt{\pi}$,

$$E^{\mathrm{self}} = \frac{1}{2}\sum_i q_i \phi^L_i(\mathbf{r}_i) = \frac{\eta}{\sqrt{\pi}}\sum_i q_i^2. \tag{4.33}$$

Now we turn to the long-range part of the energy. In order to sum it efficiently we have to switch to reciprocal space. The evaluation in reciprocal space is facilitated by the fact that the long-range charge distribution is a smooth mixture of Gaussians. Furthermore, by having separated out E^{self} we can obtain E^L from ϕ^L which is fully periodic since it does not exclude any charges in the original cell (as opposed to $\phi^L_{[i]}$). The periodic long-range charge distribution inducing ϕ^L is given by

$$\rho^L(\mathbf{r}) = \sum_{\mathbf{l}}\sum_i \rho^L_i(\mathbf{r}+\mathbf{l}) = \sum_{\mathbf{l}}\sum_i q_i G_\eta(\mathbf{r} - \mathbf{r}_i + \mathbf{l}). \tag{4.34}$$

This function is related to the potential ϕ^L via the Poisson equation

$$\boldsymbol{\nabla}^2\phi^L(\mathbf{r}) = -4\pi\rho^L(\mathbf{r}). \tag{4.35}$$

Transforming to reciprocal space gives

$$\mathbf{k}^2\hat{\phi}^L(\mathbf{r}) = 4\pi\hat{\rho}^L(\mathbf{r}). \tag{4.36}$$

Hence, given $\hat{\rho}^L$, the Fourier transform of ρ^L, we can trivially obtain $\hat{\phi}^L$. Then we just need to transform back to real space to obtain ϕ^L. First, we derive the Fourier transform of ρ^L, yielding

$$\hat{\rho}^L(\mathbf{r}) = \int_V d^3\mathbf{r}\rho^L(\mathbf{r})e^{-i\mathbf{k}\cdot\mathbf{r}} \tag{4.37}$$

$$= \int_V d^3\mathbf{r}\sum_{\mathbf{l}}\sum_i q_i G_\eta(\mathbf{r} - \mathbf{r}_i + \mathbf{l})e^{-i\mathbf{k}\cdot\mathbf{r}} \tag{4.38}$$

$$= \sum_i q_i \int_{\mathbf{R}^3} d^3\mathbf{r} G_\eta(\mathbf{r} - \mathbf{r}_i)e^{-i\mathbf{k}\cdot\mathbf{r}}, \tag{4.39}$$

where we have combined the integration over the cell volume and the sum over lattice vectors into an integral over all of space. This is possible because the reciprocal lattice vectors are commensurate with the direct lattice vectors, i.e. $e^{-i\mathbf{k}\cdot\mathbf{l}} = 1$. At this point we can employ the well-known result that the Fourier transform of a Gaussian is another Gaussian with the inverse standard deviation. The offsets $\mathbf{r}_i$ of the Gaussians from the origin simply add phase factors. We obtain

$$\hat{\rho}^L(\mathbf{r}) = \sum_i q_i e^{-i\mathbf{k}\cdot\mathbf{r}_i} e^{-\mathbf{k}^2/4\eta^2}. \tag{4.40}$$

Now, the long-range potential in reciprocal space follows straightforwardly,

$$\hat{\phi}^L(\mathbf{r}) = 4\pi \sum_i q_i e^{-i\mathbf{k}\cdot\mathbf{r}_i} \frac{e^{-\mathbf{k}^2/4\eta^2}}{\mathbf{k}^2}. \tag{4.41}$$

To get the potential in real space we apply the inverse Fourier transform,

$$\phi^L(\mathbf{r}) = \frac{1}{V} \sum_{\mathbf{k}} \hat{\phi}^L(\mathbf{r}) e^{i\mathbf{k}\cdot\mathbf{r}} \tag{4.42}$$

$$= \frac{4\pi}{V} \sum_{\mathbf{k}\neq\mathbf{0}} \sum_i q_i e^{i\mathbf{k}\cdot(\mathbf{r}-\mathbf{r}_i)} \frac{e^{-\mathbf{k}^2/4\eta^2}}{\mathbf{k}^2}. \tag{4.43}$$

Note that the we have excluded the $\mathbf{k} = \mathbf{0}$ term from the sum. This term is singular in general. However, if the cell has neutral charge the term vanishes and we obtain a finite long-range potential. In this case we can also observe that the sum over reciprocal space converges quickly since contributions from vectors $\mathbf{k}$ with large norm are exponentially suppressed. The long-range Coulomb energy follows directly:

$$E^L = \frac{1}{2} \sum_i q_i \phi^L(\mathbf{r}_i) \tag{4.44}$$

$$= \frac{2\pi}{V} \sum_{\mathbf{k}\neq\mathbf{0}} \sum_{i,j} q_i q_j e^{i\mathbf{k}\cdot(\mathbf{r}_i-\mathbf{r}_j)} \frac{e^{-\mathbf{k}^2/4\eta^2}}{\mathbf{k}^2}. \tag{4.45}$$

We have now evaluated all the terms contributing to E and can combine the results into a final expression,

$$E = E^S + E^L - E^{\text{self}} \tag{4.46}$$

$$= \frac{1}{2} \sum_{\mathbf{l}} \sum_i \sum_j{}' \frac{q_i q_j}{|\mathbf{r}_i - \mathbf{r}_j + \mathbf{l}|} \operatorname{erfc}(\eta|\mathbf{r}_i - \mathbf{r}_j + \mathbf{l}|) \tag{4.47}$$

$$+ \frac{2\pi}{V} \sum_{\mathbf{k}\neq\mathbf{0}} \sum_{i,j} q_i q_j e^{i\mathbf{k}\cdot(\mathbf{r}_i-\mathbf{r}_j)} \frac{e^{-\mathbf{k}^2/4\eta^2}}{\mathbf{k}^2}. \tag{4.48}$$

$$- \frac{\eta}{\sqrt{\pi}} \sum_i q_i^2. \tag{4.49}$$

4.4.4 Ewald summation of a lattice of dipoles

As a next step, we provide the derivation of Kantorovich's result for the dipole correction arising for a general cell shape. The details of this derivation are not given in Ref. [130], but are crucial for deriving the generalised result for anisotropic dielectrics. The strategy is to evaluate the Ewald formula for a lattice of point dipoles. This is achieved by considering a cell with two point charges $q_\pm = \pm P/d$ at positions $\mathbf{X}_\pm = \mathbf{X} \pm \frac{1}{2}\mathbf{d}$, where $d = |\mathbf{d}|$. Then we take the limit $d \to 0$, resulting in an expression for the electrostatic interaction energy of a periodic lattice of point dipoles with dipole moment $\mathbf{P} = (P/d) \cdot \mathbf{d}$. We will see that the absolute position $\mathbf{X}$ of the dipole in the original cell is irrelevant.

First, we evaluate the self-energy contribution:

$$E^{\text{self}} = \frac{\eta}{\sqrt{\pi}} \sum_i q_i^2 = \frac{2\eta}{\sqrt{\pi}} \cdot \frac{P^2}{d^2}. \tag{4.50}$$

This term diverges as we send d to zero, however we will see that it is exactly cancelled by another term that contributes to the short-range part of the energy.

The long-range part can also be evaluated easily, by substituting charges and positions into the inner sum of the expression (4.48),

$$\begin{aligned}
\sum_{i,j} q_i q_j e^{i\mathbf{k}\cdot(\mathbf{r}_i - \mathbf{r}_j)} &= \frac{P^2}{d^2}\left(2 - e^{i\mathbf{k}\cdot\mathbf{d}} - e^{-i\mathbf{k}\cdot\mathbf{d}}\right) \\
&= \frac{2P^2}{d^2}\left[1 - \cos(\mathbf{k}\cdot\mathbf{d})\right] \\
&= \frac{2P^2}{d^2}\left[\frac{1}{2}(\mathbf{k}\cdot\mathbf{d})^2 + \mathcal{O}(d^4)\right] \\
&= (\mathbf{k}\cdot\mathbf{P})^2 + \mathcal{O}(d^2) \quad \overset{d\to 0}{\longrightarrow} \quad (\mathbf{k}\cdot\mathbf{P})^2.
\end{aligned} \tag{4.51}$$

Thus we obtain the following expression for the long-range contribution to the energy:

$$E^L = \frac{2\pi}{V} \sum_{\mathbf{k}\neq\mathbf{0}} (\mathbf{k}\cdot\mathbf{P})^2 \frac{e^{-\mathbf{k}^2/4\eta^2}}{\mathbf{k}^2}, \tag{4.52}$$

which is identical to the first term in Eq. (4.16) if rewritten in tensor notation.

Most of the complications arise in the short-range Coulomb energy. We start by considering the case $\mathbf{l} = \mathbf{0}$, where the inner sum over i and j is restricted to values satisfying $i \neq j$:

$$\begin{aligned}
E^S_{\mathbf{l}=\mathbf{0}} &= \frac{1}{2} \sum_{i\neq j} \frac{q_i q_j}{|\mathbf{r}_i - \mathbf{r}_j|} \operatorname{erfc}(\eta|\mathbf{r}_i - \mathbf{r}_j|) \\
&= -\frac{P^2}{2d^2}\left[\frac{1}{|\mathbf{d}|}\operatorname{erfc}(\eta|\mathbf{d}|) + \frac{1}{|-\mathbf{d}|}\operatorname{erfc}(\eta|-\mathbf{d}|)\right] \\
&= -\frac{P^2}{d^3}\operatorname{erfc}(\eta d).
\end{aligned} \tag{4.53}$$

Next, we Taylor expand the complementary error function, yielding

$$\begin{aligned} E^S_{\mathbf{l}=\mathbf{0}} &= -\frac{P^2}{d^3}\left[1 - \frac{2\eta}{\sqrt{\pi}}d + \frac{2\eta^3}{3\sqrt{\pi}}d^3 + \mathcal{O}(d^5)\right] \\ &= -\frac{P^2}{d^3} + \frac{2\eta}{\sqrt{\pi}}\cdot\frac{P^2}{d^2} - \frac{2\eta^3}{3\sqrt{\pi}}P^2 + \mathcal{O}(d^2). \end{aligned}$$

The first term describes the direct in-cell Coulomb interaction of the charges constituting the dipole, and is therefore irrelevant for the dipole correction. The second one exactly cancels the self-energy (Eq. (4.50)). The third term corresponds to the first contribution in Kantorovich's expression Eq. (4.15). The rest vanishes as we take the limit $d \to 0$.

Having dealt with the special case $\mathbf{l} = \mathbf{0}$, we turn our attention to the terms that arise from $\mathbf{l} \neq \mathbf{0}$. Now, the sum over i and j is unrestricted and, starting with the terms where $i = j$, we obtain

$$E^S_{\mathbf{l}\neq\mathbf{0},i=j} = \frac{1}{2}\sum_{\mathbf{l}\neq\mathbf{0}}\frac{2P^2}{d^2}\frac{1}{|\mathbf{l}|}\operatorname{erfc}(\eta|\mathbf{l}|) = \frac{P^2}{d^2}\sum_{\mathbf{l}\neq\mathbf{0}}\frac{1}{l}\operatorname{erfc}(\eta l), \tag{4.54}$$

with $l = |\mathbf{l}|$. Again, this diverges as $d \to 0$. However, it is cancelled exactly by the lowest-order term of the contribution for $i \neq j$:

$$E^S_{\mathbf{l}\neq\mathbf{0},i\neq j} = -\frac{1}{2}\sum_{\mathbf{l}\neq\mathbf{0}}\frac{P^2}{d^2}\left[\frac{1}{|\mathbf{l}+\mathbf{d}|}\operatorname{erfc}(\eta|\mathbf{l}+\mathbf{d}|) + \frac{1}{|\mathbf{l}-\mathbf{d}|}\operatorname{erfc}(\eta|\mathbf{l}-\mathbf{d}|)\right] \tag{4.55}$$

$$= -\frac{1}{2}\sum_{\mathbf{l}\neq\mathbf{0}}\frac{P^2}{d^2}\left[\frac{2}{|\mathbf{l}|}\operatorname{erfc}(\eta|\mathbf{l}|) + \mathcal{O}(d^2)\right]. \tag{4.56}$$

There is no term first-order in d since the expression in brackets is invariant under changing the sign of $\mathbf{d}$. All terms higher than second order will vanish as well as we take d to zero. Hence, our strategy is to evaluate the second order term in the expansion of $\operatorname{erfc}(\eta|\mathbf{l}+\mathbf{d}|)/|\mathbf{l}+\mathbf{d}|$. By symmetry the total contribution in the bracket is then twice that. To obtain a power series in d for the denominator we employ the dipole expansion (with η inserted for later convenience),

$$\begin{aligned} \frac{1}{\eta|\mathbf{l}+\mathbf{d}|} &= \frac{1}{\eta}\left[\frac{1}{l} - \frac{\mathbf{l}\cdot\mathbf{d}}{l^3} + \frac{1}{2}\cdot\frac{3(\mathbf{l}\cdot\mathbf{d})^2 - l^2d^2}{l^5} + \mathcal{O}(d^3)\right] \\ &= \frac{1}{y} - \eta\frac{\mathbf{y}\cdot\mathbf{d}}{y^3} + \frac{\eta^2}{2}\cdot\frac{3(\mathbf{y}\cdot\mathbf{d})^2 - y^2d^2}{y^5} + \mathcal{O}(d^3), \end{aligned} \tag{4.57}$$

where we introduce the notation $\mathbf{y} = \eta\mathbf{l}$ and $y = \eta l$. In a similar fashion we expand $\eta|\mathbf{l}+\mathbf{d}|$,

the argument of erfc:

$$\eta|\mathbf{l}+\mathbf{d}| = \eta\frac{|\mathbf{l}+\mathbf{d}|^2}{|\mathbf{l}+\mathbf{d}|} = \eta\frac{l^2+2\mathbf{l}\cdot\mathbf{d}+d^2}{|\mathbf{l}+\mathbf{d}|} \tag{4.58}$$

$$= \eta\left[l - \frac{\mathbf{l}\cdot\mathbf{d}}{l} + \frac{1}{2}\cdot\frac{-(\mathbf{l}\cdot\mathbf{d})^2+l^2d^2}{l^3} + \mathcal{O}(d^3)\right] \tag{4.59}$$

$$= y\underbrace{-\eta\frac{\mathbf{y}\cdot\mathbf{d}}{y} + \frac{\eta^2}{2}\cdot\frac{-(\mathbf{y}\cdot\mathbf{d})^2+y^2d^2}{y^3} + \mathcal{O}(d^3)}_{x}, \tag{4.60}$$

Next, we write down the Taylor expansion of erfc around y with expansion parameter x,

$$\mathrm{erfc}(y+x) = \mathrm{erfc}(y) - \frac{2}{\sqrt{\pi}}e^{-y^2}x + \frac{2y}{\sqrt{\pi}}e^{-y^2}x^2 + \mathcal{O}(x^3). \tag{4.61}$$

Substituting the expression for x and collecting orders of d yields:

$$\begin{aligned}&\mathrm{erfc}(\eta|\mathbf{l}+\mathbf{d}|) = \mathrm{erfc}(y+x) = \\ &= \mathrm{erfc}(y) - \frac{2\eta}{\sqrt{\pi}}e^{-y^2}\cdot\frac{\mathbf{y}\cdot\mathbf{d}}{y} + \frac{2\eta^2}{\sqrt{\pi}}e^{-y^2}\left[\frac{(\mathbf{y}\cdot\mathbf{d})^2}{y} - \frac{-(\mathbf{y}\cdot\mathbf{d})^2+y^2d^2}{2y^3}\right] + \mathcal{O}(d^3).\end{aligned} \tag{4.62}$$

Finally, we evaluate the product of this with the dipole expansion Eq. (4.57), only keeping track of the relevant second-order terms,

$$\begin{aligned}&\left[\frac{1}{|\mathbf{l}+\mathbf{d}|}\,\mathrm{erfc}(\eta|\mathbf{l}+\mathbf{d}|)\right]_{\mathcal{O}(d^2)} = \\ &= \frac{\eta^3}{2}\left\{-d^2\left[\underbrace{\frac{\mathrm{erfc}(y)}{y^3} + \frac{2}{\sqrt{\pi}}\cdot\frac{e^{-y^2}}{y^2}}_{h(y)}\right] + \frac{(\mathbf{y}\cdot\mathbf{d})^2}{y^2}\left[3h(y) + \frac{4}{\sqrt{\pi}}e^{-y^2}\right]\right\}\end{aligned} \tag{4.63}$$

At last we can go back to Eq. (4.56) to obtain the missing terms contributing to the short-range energy in the limit $d \to 0$,

$$E^S_{\mathbf{l}\neq\mathbf{0}} = -\frac{\eta^3}{2}\sum_{\mathbf{l}\neq\mathbf{0}}\left\{-P^2h(y) + \frac{(\mathbf{y}\cdot\mathbf{P})^2}{y^2}\left[3h(y) + \frac{4}{\sqrt{\pi}}e^{-y^2}\right]\right\}. \tag{4.64}$$

By inspection, this corresponds to the remaining terms in Kantorovich's expression, specifically the second half of Eq. (4.16).

4.4.5 Generalisation to dielectric background medium

To obtain a dipole correction applicable to the problem at hand, in which space is filled with a dielectric medium (the pentacene crystal), we need to go one step further. The dielectric response of a uniform, but in general anisotropic medium can be described using a dielectric tensor $\underline{\underline{\epsilon}}$. The dielectric tensor is a symmetric 3×3 matrix with eigenvalues $\{\epsilon_i, i=1,2,3\}$

representing the permittivity of the medium along is principal axes. In this setting the Poisson equation is modified, with $\underline{\underline{\epsilon}}$ now appearing inside the Laplacian, namely

$$\boldsymbol{\nabla}^t \underline{\underline{\epsilon}} \boldsymbol{\nabla} \phi(\mathbf{r}) = -4\pi\rho(\mathbf{r}). \tag{4.65}$$

Fischerauer [132] showed that the solution of this general Poisson equation for a point-charge can be reduced to the isotropic case by a coordinate transformation. The new coordinates that achieve this are precisely the ones corresponding to the principal axes of $\underline{\underline{\epsilon}}$. Let $\underline{\underline{C}}$ be the principal axis transformation diagonalising $\underline{\underline{\epsilon}}$, i.e

$$\underline{\underline{C}}^t \underline{\underline{\epsilon}} \underline{\underline{C}} = \begin{bmatrix} \epsilon_1 & 0 & 0 \\ 0 & \epsilon_2 & 0 \\ 0 & 0 & \epsilon_3 \end{bmatrix}. \tag{4.66}$$

$\underline{\underline{C}}$ is an orthogonal matrix obeying $\underline{\underline{C}}^{-1} = \underline{\underline{C}}^t$ and a determinant equal to unity. The only remaining anisotropy is now due to the eigenvalues ϵ_i. It can be removed by means of an additional diagonal scaling matrix $\underline{\underline{D}}$,

$$\underline{\underline{D}} = \begin{bmatrix} \sqrt{\epsilon}_1 & 0 & 0 \\ 0 & \sqrt{\epsilon}_2 & 0 \\ 0 & 0 & \sqrt{\epsilon}_3 \end{bmatrix}. \tag{4.67}$$

Applying this subsequently reduces $\underline{\underline{\epsilon}}$ to the unit matrix,

$$\underline{\underline{D}}^{-1} \underline{\underline{C}}^t \underline{\underline{\epsilon}} \underline{\underline{C}} \underline{\underline{D}}^{-1} = \begin{bmatrix} 1 & 0 & 0 \\ 0 & 1 & 0 \\ 0 & 0 & 1 \end{bmatrix}, \tag{4.68}$$

or equivalently,

$$\epsilon = \underline{\underline{C}} \underline{\underline{D}}^2 \underline{\underline{C}}^t. \tag{4.69}$$

In terms of position vectors, the complete transformation is then defined as follows:

$$\mathbf{r}' = \underline{\underline{D}}^{-1} \underline{\underline{C}}^t \mathbf{r}, \quad \mathbf{r} = \underline{\underline{C}} \underline{\underline{D}} \mathbf{r}' \tag{4.70}$$

In terms of the new coordinates the form of Poisson's equation reverts to the vacuum case, i.e.

$$\Delta' \phi(\mathbf{r}') = -4\pi\rho(\mathbf{r}'). \tag{4.71}$$

If we consider a point-charge centred at the origin this becomes

$$\Delta' \phi(\mathbf{r}') = -\frac{4\pi}{\sqrt{\det \underline{\underline{\epsilon}}}} \delta(\mathbf{r}'). \tag{4.72}$$

The denominator that appears is the Jacobian determinant of the transformation,

$$J = \det \frac{\partial x_i}{\partial x'_j} = \det \underline{\underline{C}} \underline{\underline{D}} = \det \underline{\underline{C}} \cdot \det \underline{\underline{D}} = \sqrt{\det \underline{\underline{\epsilon}}}. \tag{4.73}$$

It ensures that the normalisation of the delta function in the new coordinates is consistent with being unity in the original frame (which is not scaled by $\underline{\underline{D}}$). The solution is straightforwad:

$$\phi(\mathbf{r}') = \frac{1}{\sqrt{\det \underline{\underline{\epsilon}}}} \cdot \frac{1}{|\mathbf{r}'|}. \tag{4.74}$$

Going back to the original coordinates we thus obtain:

$$\phi(\mathbf{r}) = \frac{1}{\sqrt{\det \underline{\underline{\epsilon}}}} \cdot \frac{1}{|\underline{\underline{D}}^{-1}\underline{\underline{C}}^t\mathbf{r}|} = \frac{1}{\sqrt{\det \underline{\underline{\epsilon}}}} \cdot \frac{1}{\sqrt{\mathbf{r}^t\underline{\underline{\epsilon}}^{-1}\mathbf{r}}}. \tag{4.75}$$

The last equality follows since

$$\begin{aligned} |\underline{\underline{D}}^{-1}\underline{\underline{C}}^t\mathbf{r}| &= \sqrt{|\underline{\underline{D}}^{-1}\underline{\underline{C}}^t\mathbf{r}|^2} \\ &= \sqrt{(\underline{\underline{D}}^{-1}\underline{\underline{C}}^t\mathbf{r})^t(\underline{\underline{D}}^{-1}\underline{\underline{C}}^t\mathbf{r})} \\ &= \sqrt{\mathbf{r}^t\underline{\underline{C}}\underline{\underline{D}}^{-2}\underline{\underline{C}}^t\mathbf{r}} \quad = \quad \sqrt{\mathbf{r}^t\underline{\underline{\epsilon}}^{-1}\mathbf{r}}. \end{aligned}$$

Ideally we would like to adapt this procedure, demonstrated here for a point-charge, to the full derivation of the Ewald method and dipole correction. We would hope to obtain expressions that are essentially completely analogous, up to a coordinate transformation of the direct and reciprocal lattice vectors. However, it turns out that a direct application of the method fails. The reason is that the univariate Gaussian used for splitting the charge distribution in the Ewald method becomes multivariate in the transformed coordinates,

$$G_\eta(\mathbf{r}) = \left(\frac{\eta}{\sqrt{\pi}}\right)^3 \exp(-\eta^2\mathbf{r}^t\mathbf{r}) \tag{4.76}$$

$$= \left(\frac{\eta}{\sqrt{\pi}}\right)^3 \exp\left[-\eta^2(\underline{\underline{C}}\underline{\underline{D}}\mathbf{r}')^t(\underline{\underline{C}}\underline{\underline{D}}\mathbf{r}')\right] \tag{4.77}$$

$$= \left(\frac{\eta}{\sqrt{\pi}}\right)^3 \exp\left[-\eta^2\mathbf{r}'^t\underline{\underline{D}}^2\mathbf{r}'\right]. \tag{4.78}$$

Hence, the corresponding potential can no longer be obtained easily in spherical coordinates, and the mathematical expressions start to differ substantially from the vacuum case. To understand how to circumvent this problem we recall that the smearing function was introduced artificially and we were free to chose its (inverse) width as defined by Ewald's parameter η. Taking this idea further, we could consider a multivariate smearing function. A particularly interesting choice turns out to be

$$G^\epsilon_\eta(\mathbf{r}) = \frac{1}{\sqrt{\det \underline{\underline{\epsilon}}}} \left(\frac{\eta}{\sqrt{\pi}}\right)^3 \exp(-\eta^2\mathbf{r}^t\underline{\underline{\epsilon}}^{-1}\mathbf{r}), \tag{4.79}$$

where we have inserted the inverse dielectric tensor $\underline{\underline{\epsilon}}^{-1} = \underline{\underline{C}}\underline{\underline{D}}^{-2}\underline{\underline{C}}^t$ in the exponential, and the prefactor ensures normalisation. The inverse dielectric tensor exactly cancels the

transformation matrices and we obtain a univariate Gaussian in the primed coordinates:

$$\begin{aligned} G_\eta^\epsilon(\mathbf{r}) &= \frac{1}{\sqrt{\det \underline{\underline{\epsilon}}}} \left(\frac{\eta}{\sqrt{\pi}}\right)^3 \exp\left[-\eta^2 (\underline{\underline{CD}}\mathbf{r}')^t \underline{\underline{\epsilon}}^{-1} (\underline{\underline{CD}}\mathbf{r}')\right] \\ &= \frac{1}{\sqrt{\det \underline{\underline{\epsilon}}}} \left(\frac{\eta}{\sqrt{\pi}}\right)^3 \exp\left[-\eta^2 \mathbf{r}'^t \underline{\underline{DC}}^t \underline{\underline{\epsilon}}^{-1} \underline{\underline{CD}}\mathbf{r}'\right] \\ &= \frac{1}{\sqrt{\det \underline{\underline{\epsilon}}}} \left(\frac{\eta}{\sqrt{\pi}}\right)^3 \exp\left[-\eta^2 \mathbf{r}'^t \mathbf{r}'\right] \quad = \quad \frac{1}{\sqrt{\det \underline{\underline{\epsilon}}}} G_\eta(\mathbf{r}'). \end{aligned} \tag{4.80}$$

Hence, the solution of Poisson's equation is now completely analogous to the vacuum case, we obtain

$$\phi_\eta^\epsilon(\mathbf{r}) = \frac{1}{\sqrt{\det \underline{\underline{\epsilon}}}} \cdot \frac{1}{|\mathbf{r}'|} \operatorname{erf}(\eta |\mathbf{r}'|) \tag{4.81}$$

$$= \frac{1}{\sqrt{\det \underline{\underline{\epsilon}}}} \cdot \frac{1}{|\underline{\underline{D}}^{-1} \underline{\underline{C}}^t \mathbf{r}|} \operatorname{erf}(\eta |\underline{\underline{D}}^{-1} \underline{\underline{C}}^t \mathbf{r}|). \tag{4.82}$$

If we follow through the derivation of Ewald's formula with this result, we end up with equivalent expressions for short-range and self-energy, up to an overall factor of $1/\sqrt{\det \underline{\underline{\epsilon}}}$ and transformed position and lattice vectors, $\mathbf{r} \to \mathbf{r}'$ and $\mathbf{l} \to \mathbf{l}'$. As a consequence, the real-space terms of Kantorovich's expression have the same form as in the vacuum case, up to the prefactor and primed direct lattice vectors and dipole vector.

Turning to the reciprocal space part, the Fourier transform of the long-range charge distribution with the modified smearing function is given by

$$\hat{\rho}^L(\mathbf{r}) = \sum_i q_i \int_{\mathbf{R}^3} d^3\mathbf{r} G_\eta^\epsilon(\mathbf{r} - \mathbf{r}_i) e^{-i\mathbf{k}\cdot\mathbf{r}} \tag{4.83}$$

$$= \sum_i q_i \int_{\mathbf{R}^3} d^3\mathbf{r}' G_\eta(\mathbf{r}' - \mathbf{r}_i') e^{-i\mathbf{k}'\cdot\mathbf{r}'} \tag{4.84}$$

$$= \sum_i q_i e^{-i\mathbf{k}'\cdot\mathbf{r}_i'} e^{-\mathbf{k}'^2/4\eta^2}. \tag{4.85}$$

Here $\mathbf{k}' = \underline{\underline{DC}}^t \mathbf{k}$, ensuring that $\mathbf{k}' \cdot \mathbf{r}' = \mathbf{k} \cdot \mathbf{r}$. The prefactor of $1/\sqrt{\det \underline{\underline{\epsilon}}}$ cancels with the Jacobian incurred due to the change of variables under the integral. This expression is identical to Eq. (4.40) up to the primed vectors. Also, the Poisson equation in the primed system has the same form as in the vacuum case. This means that the form of the reciprocal-space term in the Ewald formula is again unchanged up to the vector transformations. Note that we do not obtain an additional prefactor of $1/\sqrt{\det \underline{\underline{\epsilon}}}$ in this case. Again, these properties carry over to the reciprocal-space contribution in Kantorovich's formula.

Now, we are ready to state the final result for the dipole correction in a uniform, anisotropic background medium:

$$E_{\text{dip}} = \frac{1}{\sqrt{\det \underline{\underline{\epsilon}}}} \left(-\frac{2\eta^3}{3\sqrt{\pi}} \cdot |\mathbf{P}'|^2 + \frac{1}{2} \sum_{\alpha,\beta} P'_\alpha \psi'_{\alpha\beta} P'_\beta \right), \tag{4.86}$$

with

$$\psi'_{\alpha\beta} = \frac{4\pi}{V'} \sum_{\mathbf{k}'\neq\mathbf{0}} \frac{k'_\alpha k'_\beta}{|\mathbf{k}'|^2} e^{-|\mathbf{k}'|^2/4\eta^2} - \eta^3 \sum_{\mathbf{l}'\neq\mathbf{0}} H_{\alpha\beta}(\eta\mathbf{l}'), \tag{4.87}$$

and $H_{\alpha\beta}$ as given in Eqs. (4.17) and (4.18). For completeness, we also restate how the coordinate transformation acts on the relevant vectors, namely

$$\mathbf{P}' = \underline{\underline{D}}^{-1}\underline{\underline{C}}^t\mathbf{P}, \quad \mathbf{l}' = \underline{\underline{D}}^{-1}\underline{\underline{C}}^t\mathbf{l}, \quad \mathbf{k}' = \underline{\underline{DC}}^t\mathbf{k}, \tag{4.88}$$

and we introduce

$$V' = \frac{V}{\sqrt{\det \underline{\underline{\epsilon}}}}. \tag{4.89}$$

This rescaling of the cell volume is consistent with the transformation of the direct lattice vectors and is a convenient way to account for the fact that the reciprocal-space term does not share the prefactor $1/\sqrt{\det \underline{\underline{\epsilon}}}$.

4.4.6 Applying the correction

First, we perform a DFPT calculation using the CASTEP code to obtain the dielectric tensor for the primitive cell of the pentacene crystal:

$$\underline{\underline{\epsilon}}_{\mathrm{DFPT}} = \begin{bmatrix} 3.48 & -0.18 & -0.12 \\ -0.18 & 3.14 & 0.19 \\ -0.12 & 0.19 & 5.61 \end{bmatrix}.$$

The effective dielectric tensor as it is experienced by the constrained charges in the cDFT calculation is assumed to be obtained by a uniform scaling $\underline{\underline{\epsilon}} = c \cdot \underline{\underline{\epsilon}}_{\mathrm{DFPT}}$. The scaling accounts for the overestimation of screening due to the band-gap error, as previously discussed. By using a single scaling parameter c we employ the simplifying assumption that the overscreening of DFPT is isotropic. The dipole moments were taken from dimer cDFT calculations in vacuum (atomic units):

$$\begin{aligned} \mathbf{P}_{\mathrm{her1}} &= (1.45, -6.70, -2.07)^t, & |\mathbf{P}_{\mathrm{her1}}| &= 7.16 \\ \mathbf{P}_{\mathrm{her2}} &= (-1.19, 7.58, 2.33)^t, & |\mathbf{P}_{\mathrm{her2}}| &= 8.02 \\ \mathbf{P}_{\mathrm{par1/2}} &= \pm(-7.89, 4.23, 1.85)^t, & \left|\mathbf{P}_{\mathrm{par1/2}}\right| &= 9.14 \end{aligned}$$

The dipole correction is applied to the supercell energies as follows:

$$E_{\mathrm{cor}} = E_{\mathrm{DFT}} - E_{\mathrm{dip}}. \tag{4.90}$$

Minimising the combined standard deviations of the corrected supercell calculations across all three dimer configurations yields a best-fit value $c = 0.378$. The effect of the correction using this value of c for the three cases is shown graphically in Fig. 4.3. We note that the

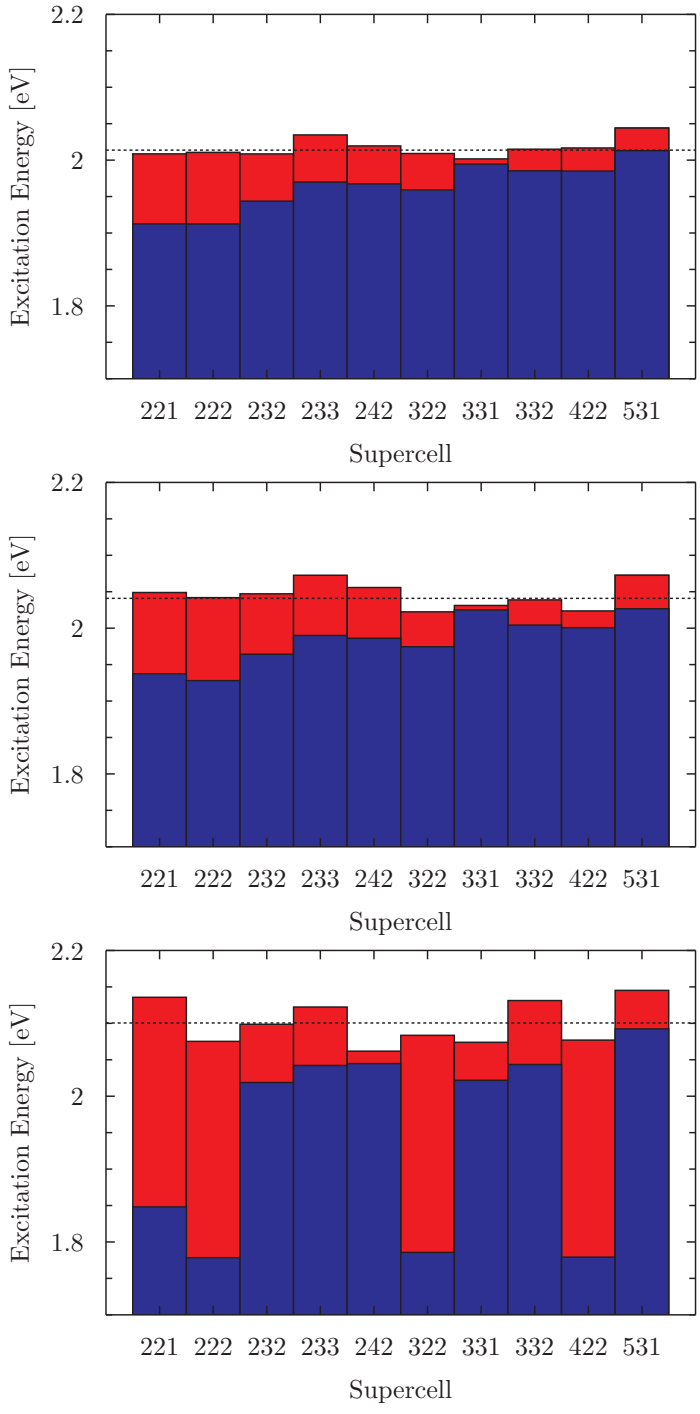

Figure 4.3: *(Top)* Herringbone 1 *(Centre)* Herringbone 2 *(Bottom)* Parallel. Uncorrected energies (blue) and dipole corrections (red) for CT states across a range of supercell embeddings. Dashed lines indicate corrected mean energies. Note that the dipole correction is negative for the 531 supercell for both herringbone configurations.

Configuration	isolated (2 mol)	4-mol cluster	10-mol cluster	crystal
Herringbone 1	2.04	2.16	2.00	2.01
Herringbone 2	2.72	2.25	2.04	2.04
Parallel	2.61	2.35	2.10	2.10

Table 4.3: Comparison of dipole-corrected CT energies in the crystal with isolated and cluster results. Excitation energies are quoted in units of eV.

value of c is in approximate agreement with the ratio of the DFT gap of ~ 0.8 eV to the quasiparticle gap of ~ 2.4 eV calculated with many-body perturbation theory [60], as might be expected.

Having applied Eq. (4.90), for the herringbone dimer we obtain corrected mean energies of 2.01 eV and 2.04 eV, respectively (cf. Tab. 4.3). The parallel dimer yields a mean energy of 2.10 eV. The spread of corrected energies is down to 0.03-0.08 eV, a reduction by a factor of 3-4, demonstrating the success of the method. The significantly larger spread of values in the parallel dimer compared to the herringbone dimer is a result of enhanced dipole interaction between periodic images. This is due to the fact that the dimer (and hence dipole) is aligned with the crystal lattice (along lattice vector $\mathbf{b}$, cf. Fig. 3.2) and the dipole moment is largest among the three configurations.

4.5 Discussion

As elaborated above, the empirical parameter c in the method accounts for the overscreening of DFPT with local functionals. There are additional uncertainties due to the fact that the separation of periodic images is small, implying that the supercell calculations still exhibit a relatively high density of electron-hole pairs. This can modify the dielectric properties. Further errors may stem from higher-order electrostatic corrections as a result of the fact that the CT configurations considered take up a significant portions of the supercells and hence do not constitute perfectly point-like dipoles. All these effects are integrated in the c parameter. The remaining spread of energies is presumably related to residuals of these sources of error which cannot be eliminated with the single c parameter.

It is apparent that the dipole-corrected energies are essentially degenerate with those obtained for the 10-molecule cluster, within the quoted precision of 10 meV (cf. Table 4.3). Presuming this holds for still-larger clusters, this result demonstrates the validity of the cluster approximation for molecular crystals of pentacene and likely a range of similar molecules (eg. tetracene). In case where the molecular unit of a molecular crystal has a net dipole, the cluster approach in vacuum would incur significant difficulties due to the unscreened

net-dipole [133]. The current approach, in employing periodic boundary conditions, would not encounter such problems.

We observe that aggregation has a twofold effect on CT energies in the pentacene molecular crystal: an overall downshift, and a decreasing separation of the different CT configurations considered. The latter is particularly striking in the herringbone dimer, where the initial splitting of nearly 0.7 eV in isolation is reduced to only a few 10 meV when embedded in the crystal. Interestingly, the ordering of the three CT energies also changes. In the isolated dimers, the parallel CT energy is situated between the two herringbone energies, whereas in the crystal the parallel energy is slightly above the two (now nearly degenerate) herringbone energies.

We also note that although our calculations employ the computationally cheap LDA functional they do not appear to suffer from a systematic underestimation of excitation energies relative to those calculated with higher levels of theory. This observation can be rationalised by noting that in cDFT the excited electron orbital is fully occupied. No DFT eigenvalues of unoccupied orbitals which are subject to large systematic underestimation enter the calculation. TDDFT with local exchange requires computationally expensive and parameter-dependent range-separated hybrid functionals in order to yield CT energies that are not severely underestimated [25,35]. By contrast, using the novel combination of linear-scaling methodology with projector-based cDFT, we are able to perform relatively cheap calculations which scale well to large system sizes (1368 atoms, in this work).

We further note that the relatively low CT energies in the crystal of just above 2 eV put them on the lower end of experimental estimates [64]. They are in line with previous theoretical results indicating a significant admixture of CT-like components into the lowest singlet exciton in pentacene [72,73,134]. The low energies also lend support to the notion that a CT-mediated 'super-exchange' mechanism can play a crucial role in ultrafast fission [79–81,91].

Our procedure should also be transferable to other systems in which CT states are situated in a complex screening environment. These include (but are not limited to) a variety of organic materials for organic photovoltaics and optoelectronics/spintronics.

At this point there remain a number of limitations that need to be addressed by future work. Our method as presented here relies on the system in question exhibiting sufficiently homogeneous dielectric properties which can be approximated by a single dielectric tensor. Furthermore, the cDFT approach necessitates prior knowledge of the excited state structure such that appropriate donor and acceptor regions can be defined. Another current drawback is the requirement of performing calculations on a range of supercells for the purpose of the single parameter fit, increasing computational cost. This limitation may be overcome

by using a more accurate functional (or higher-level theory than DFT) for the response calculation, provided that the unit cell is not so large as to make this computationally infeasible.

4.6 Conclusions

In this chapter we have demonstrated the application of (linear-scaling) constrained DFT to charge-transfer states in the pentacene molecular crystal. Our results for isolated dimers are in reasonable agreement with higher-level theory calculations from the literature. Furthermore, we have used cluster calculations to illustrate the transition to the crystal limit, showing that CT energies are lowered both by screening and the formation of bands. We have devised a scheme based on periodic supercell calculations in combination with a dipole correction, in order to establish the limit of the infinite molecular crystal. Our dipole correction method is novel in that it is applicable to very general systems (non-cubic with anisotropic dielectric properties). It is also of significant interest that in spite of the high-polarity of the CT configurations, the excellent agreement between results for the cluster approximation and for the crystal limit reveals an unexpectedly high screening capability for pentacene, with important consequences for the modelling of pentacene interfaces and film structural imperfections.

Chapter 5

Dynamical modelling of singlet fission in dimer pentacene

Singlet fission has been observed to occur in DP-Mes, a covalently linked pentacene dimer, on ultrafast sub-picosecond timescales with the yield of triplet pairs from initial singlets approaching 100%, depending on the specific solvent environment [88, 89]. The geometrical structure of the molecule is shown in Fig. 5.1. Specifically, the pentacene units assume an orthogonal configuration, with the dihedral angle at the linking C-C bond close to 90°.

In this chapter, we develop a dynamical model of singlet fission in DP-Mes. As we will see, the high symmetry of the molecule precludes coupling of the electronic states at the equilibrium geometry. This make DP-Mes an ideal test-case for exploring the interplay between electronic states and symmetry-breaking molecular vibrations in the fission process. We employ a combination of DFT and a multi-reference description of the electronic states using a minimal basis of frontier orbitals to parametrise the vibronic coupling Hamiltonian of the system. This parametrisation forms the basis for subsequent simulations of the full quantum dynamics of the system using tensor network methods. We reveal how ultrafast fission on time-scales on the order of hundreds of femtoseconds arises from a series of symmetry breaking vibrational motions that drive fission via CT-mediated super-exchange. The reorganisation of the vibrational environment after photoexcitation is found to spontaneously create the couplings enabling fission with a high ($\sim 90\%$) yield of triplet pairs.

The high degree of symmetry of the DP-Mes molecule leads to a lot of structure in the electronic-vibrational coupling. Exploiting this structure is crucial for making such high-level modelling possible at reasonable computational cost. Hence, DP-Mes presents itself as an ideal model system for detailed theoretical studies of fission.

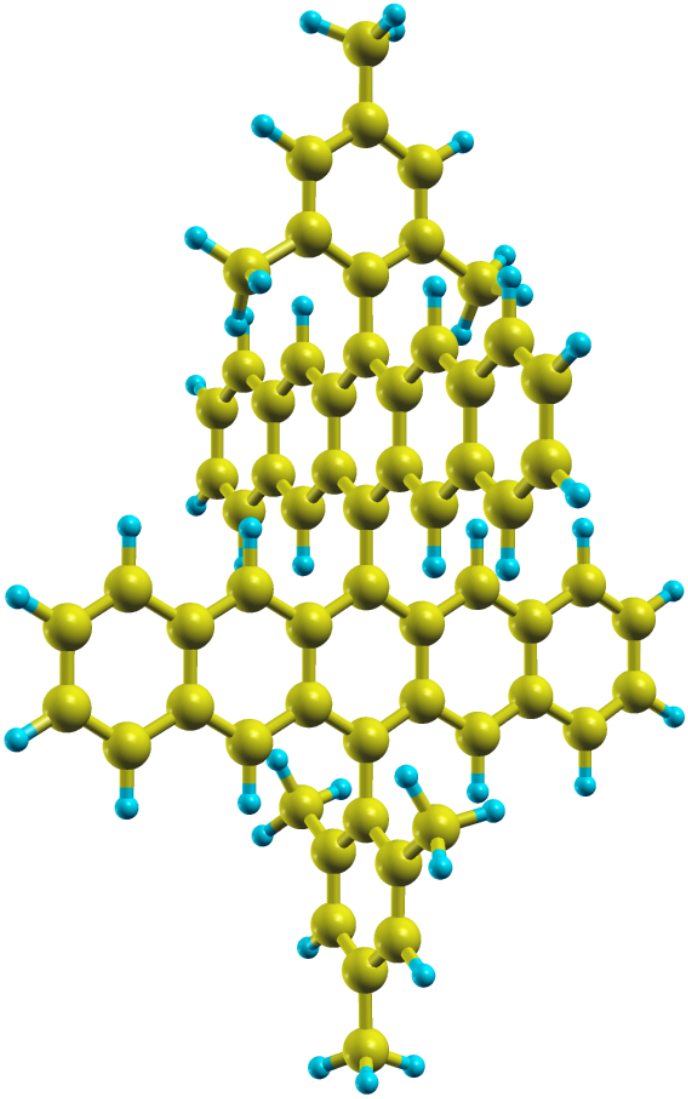

Figure 5.1: 3-dimensional geometry of the covalent pentacene dimer DP-Mes (13,13'-bis(mesityl)-6,6'-dipentacenyl). At the lowest-energy configuration in the electronic ground state the pentacene units are orthogonal, with a dihedral angle close to 90°. This geometry minimises steric repulsion between the hydrogen atoms.

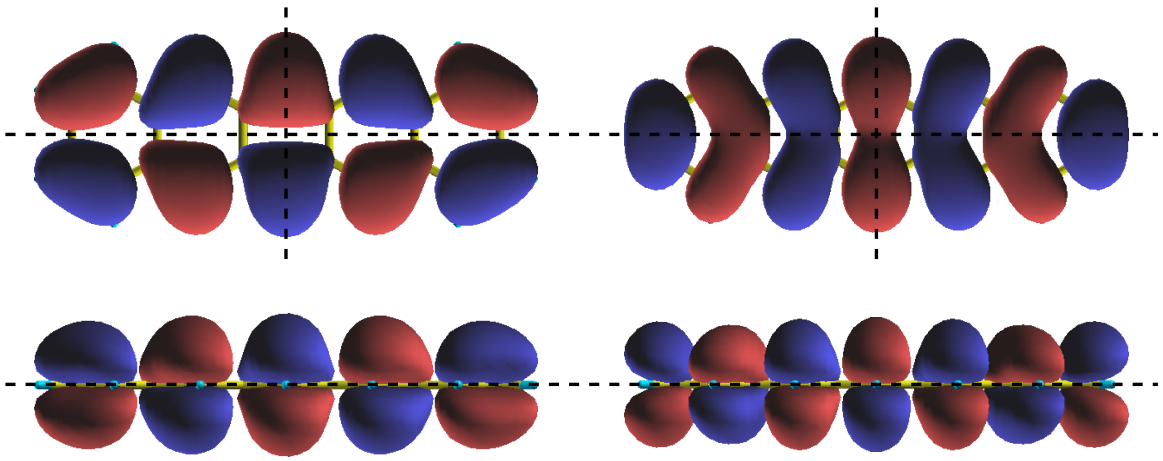

Figure 5.2: HOMO (*left*) and LUMO (*right*) of pentacene monomer, top and edge-on view, respectively. Both orbitals are antisymmetric about the molecular plane (π-character), and symmetric about a perpendicular plane through the short axis. With respect to an orthogonal plane through the long axis, the HOMO is antisymmetric, whereas the LUMO is symmetric.

5.1 Geometry and electronic structure

All DFT calculations for this chapter are performed with the NWChem electronic structure code in vacuum [135]. The relaxed ground-state structure is obtained employing analytical Hessians at the cc-pVDZ/B3LYP level of theory. Excited singlet state energies are calculated from (linear-response) TDDFT at the cc-pVDZ/LC-BLYP level of theory. The long-range corrected functional is required to correctly describe the S_1 state of pentacene as well as the states with charge-transfer character. An optimised range-separation parameter $\mu = 0.29$ is used in the LC-BLYP functional [136]. This choice gives a good description of the energy of the first excited singlet of the pentacene molecule. For TT the quintet state (total spin 2) is used as a proxy for the purpose of calculating energy and forces. Even though the spin wave function is incorrect, it forces a doubly-excited state with local triplet character on each pentacene unit. This can be expected to be sufficient for the purpose of energies and forces due to the weak coupling between the pentacene units in the ground-state geometry.

The choice of the relatively small cc-pVDZ basis set is due to limited computational resources. However, tests show that TDDFT energies of the low-lying excitations of DP-Mes are converged to within 10 meV compared to the larger cc-pVTZ basis set.

5.1.1 Low-energy excitations

The lowest-energy singlet and triplet excited states S_1 and T_1 (the ground state being S_0) of a single pentacene molecule are dominated by a HOMO to LUMO transition (see orbital plots, Fig. 5.2). It can be seen that the HOMO is antisymmetric about a plane through the long molecular axis and orthogonal to the molecular plane, whereas the LUMO is symmetric about this plane. This means that the $S_0 \rightarrow S_1$ transition is polarised along the short molecular axis. The triplet is optically dark since the $S_1 \rightarrow T$ transition is spin-forbidden.

Upon dimerisation, each pentacene molecule mostly retains its S_1 state with little change in energy. However, dipole coupling of the transitions causes Davydov splitting and hybridisation into symmetric and antisymmetric locally excited states $\mathrm{LE}^{\pm} = \frac{1}{\sqrt{2}}(\mathrm{S}_1^{\mathrm{A}}\mathrm{S}_0^{\mathrm{B}} \pm \mathrm{S}_0^{\mathrm{A}}\mathrm{S}_1^{\mathrm{B}})$, where A and B denote the monomers. In the dimer configuration the pentacene units are aligned along their short axes, i.e. their transition dipoles. The dipoles add constructively for a transition to the LE^+ configuration and cancel exactly for LE^-. This means that LE^+ is optically bright, and represents the state populated by photoexcitation from which fission proceeds. LE^-, on the other hand, is optically dark. At the relaxed ground state geometry, our calculations put LE^+ at 2.15 eV, with LE^- at 2.28 eV, higher by about 130 meV due to energetically less favourable dipole alignment.

In addition to the locally excited states, the dimer also supports excitations of charge-transfer character. The lowest-energy pair of these states is again well described by HOMO-LUMO transitions, e.g. from the HOMO of unit A to the LUMO of unit B, and vice versa for the second CT state. In the absence of external symmetry-breaking, the CT states undergo weak (∼10 meV) hybridisation into (anti-)symmetrised 'charge-resonance' states denoted $\mathrm{CT}^{\pm}$. We calculate energies of 2.75 eV and 2.76 eV, respectively. However, we note that these values should be treated with caution since they are obtained from a linear-response (TDDFT) calculation for a state with significantly altered charge distribution compared to the ground state.

The final state of fission is believed to be the TT state which is a doubly excited state constructed from T_1 pairs (one for each unit), such that the overall wave function is a singlet. The TT energy is approximately given by twice the T_1 energy for weakly interacting units. The quintet state, which we use as a proxy for TT, gives an energy of 1.87 eV above the ground state.

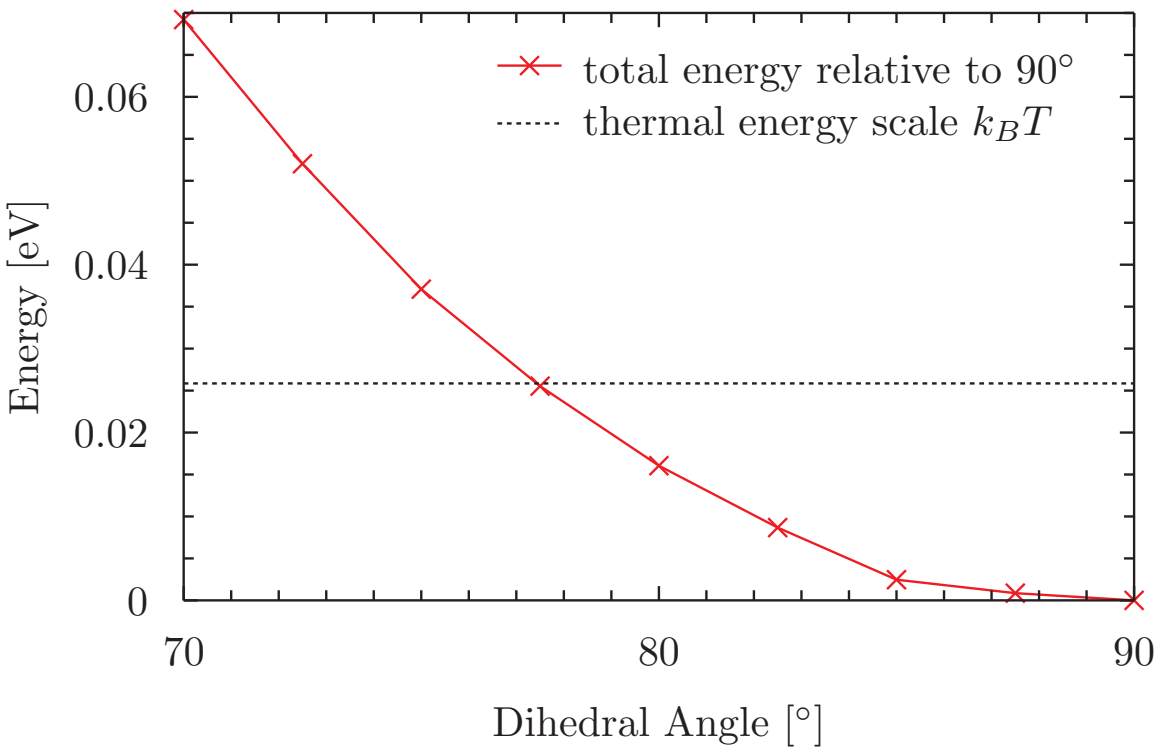

Figure 5.3: Potential energy surface for the electronic ground state along the dihedral coordinate. Each data point represents the total DFT energy relative to the 90°-configuration after geometry relaxation with the dihedral angle fixed at the respective value.

5.1.2 Frontier orbitals and role of dihedral coordinate

In the ground state the minimal total energy of DP-Mes is attained at a dihedral angle of 90°. However, the potential energy surface along the dihedral coordinate is quite shallow, enabling the molecule to explore an angular range of about 10–20° either side of the minimum at room temperature (see Fig. 5.3). Only at large deviations steric repulsion of the hydrogen atoms becomes energetically prohibitive.

Most importantly, the dihedral coordinate determines coupling between the monomers. The monomeric HOMO and LUMO orbitals are antisymmetric with respect to a reflection through the molecular plane, but symmetric about a perpendicular plane through the short axis. Hence, all hopping matrix elements have to vanish by symmetry at the 90° geometry (Fig. 5.4). A coupling can only arise as the dihedral angle moves away from this configuration.

This can also be demonstrated using DFT by looking at the energy gaps between HOMO-1/HOMO and LUMO/LUMO+1 levels of the dimer, respectively (Fig. 5.4). The HOMO-1 (LUMO) and HOMO (LUMO+1) levels result from a hybridisation of the HOMO (LUMO)

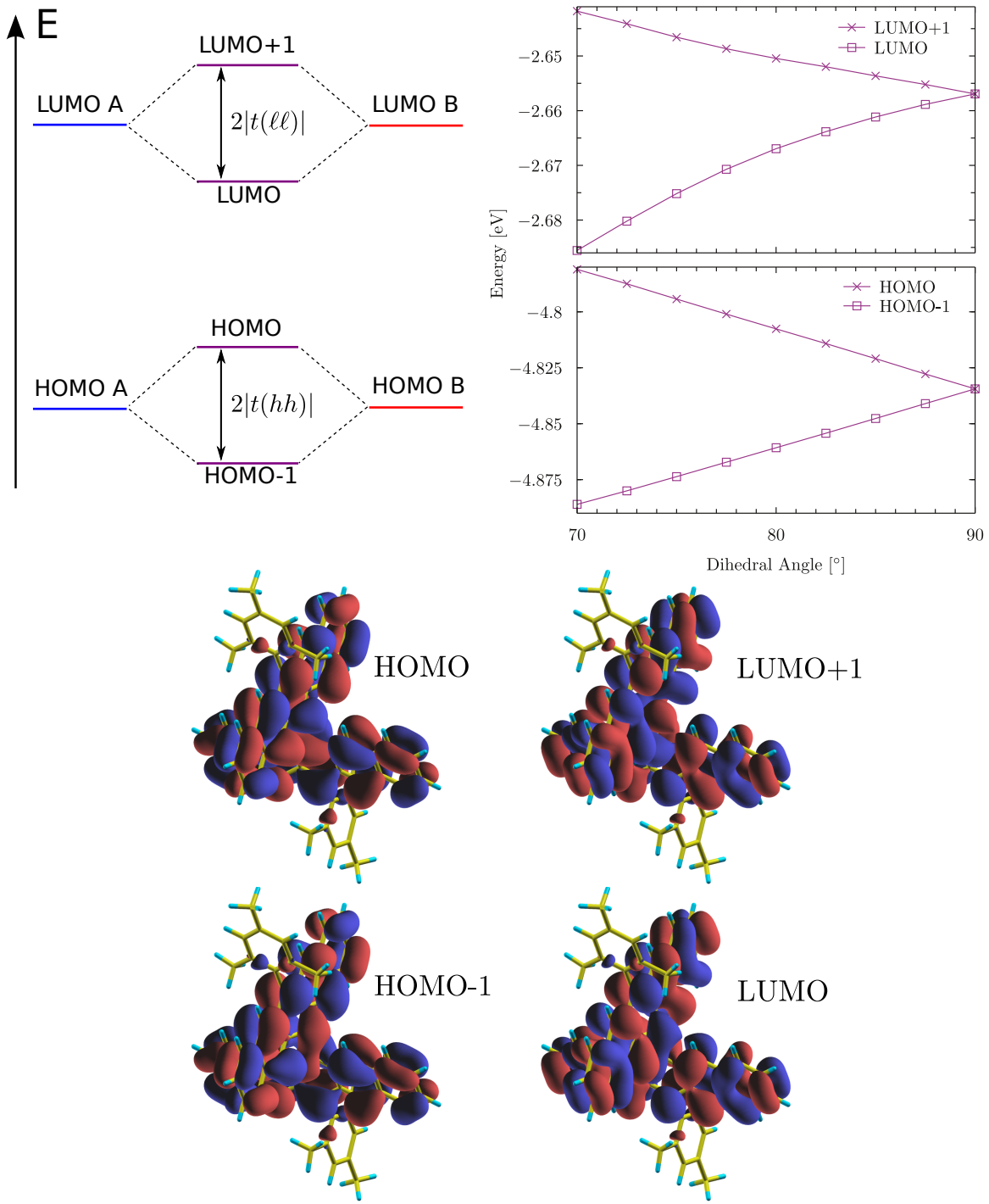

Figure 5.4: (*top left*) Schematic diagram showing how the HOMO-1/HOMO and LUMO/LUMO+1 levels of the dimer arise from a hybridisation of the monomer HOMOs and LUMOs, respectively. (*top right*) DFT results corresponding to figure 5.3 demonstrate angle-dependence of level-splitting. (*bottom*) Frontier orbitals of DP-Mes. They are well-described as (anti)symmetric linear combinations of the monomeric frontier orbitals, compare Fig. 5.2. The different symmetries of the orbitals with respect to the pentacene plane and a perpendicular plane through the short axis, respectively, mean that inter-unit hopping integrals vanish at the orthogonal geometry.

levels of the two pentacene units. The degeneracy present at 90° is increasingly lifted as the angle deviates from this value, with the gaps approximately corresponding to twice the respective hopping integrals $t(hh)$, $t(\ell\ell)$.

5.2 Symmetry considerations and frontier-orbital description of excitations

In this section we discuss the symmetries of the DP-Mes molecule, more specifically the properties of its point group D_{2d}. This includes a review of its symmetry transformations (or elements) and irreducible representations. In combination with a frontier orbital description of the electronic states which we outline in the following, the irreducible representations allow us to classify these states according to how they transform under the molecular symmetries. In a similar manner, the vibrational normal modes of DP-Mes can be assigned to irreducible representations. When we later couple the electronic excitations to the vibrational modes, this analysis is crucial for understanding the interplay of electronic transitions and vibrations.

5.2.1 The D_{2d} point group

Fig. 5.5 shows the DP-Mes structure and the symmetry operations that leave the structure invariant. These symmetries, also referred to as symmetry elements, constitute the point group D_{2d}. As per the group definition, D_{2d} has an identity element, denoted E, which simply leaves space invariant and is therefore a trivial symmetry. The principal or figure axis of the molecule is a twofold rotation axis (C_2), i.e. rotations around this axis by $2\pi/2 = \pi$ leave the structure invariant. We note that the extremal hydrogens on the mesityl groups on either side break this and other symmetry operations of the point group. However, this is irrelevant for the low-energy excitations since the frontier orbitals do not meaningfully extend onto the mesityl groups (cf. Fig. 5.4). In addition to being a twofold rotation axis, the principal axis is also a fourfold improper (or alternating) rotation axis (S_4). This means that rotations around this axis by an angle $2\pi/4 = \pi/2$ followed by a reflection through a perpendicular plane leaves the geometric structure invariant. Note that there are two distinct S_4 elements since rotations by $\pm\pi/2$ are inequivalent (as opposed to $\pm\pi$ rotations). Furthermore, both pentacene planes constitute mirror planes (σ_d). Finally, there are two twofold rotation axes (C_2') perpendicular to the principal axis and bisecting the angles between the mirror planes.

A group representation is a map that assigns a linear transformation to each symmetry

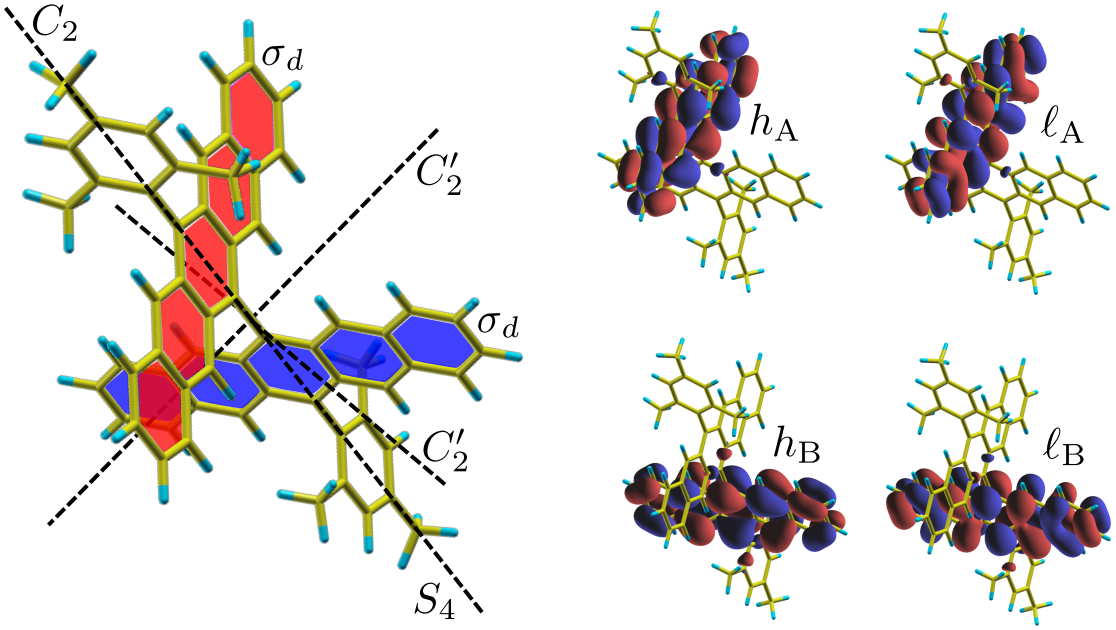

Figure 5.5: DP-Mes structure with symmetry elements of the D_{2d} point group, and unit-localised frontier molecular orbitals. Note that extremal hydrogens of mesityl side-groups weakly break the point group symmetry. However, this is irrelevant for the low-energy excitations since the frontier orbitals firmly reside on the pentacene units.

irrep	E	$2S_4$	C_2	$2C_2'$	$2\sigma_d$
A_1	+1	+1	+1	+1	+1
A_2	+1	+1	+1	−1	−1
B_1	+1	−1	+1	+1	−1
B_2	+1	−1	+1	−1	+1
E	+2	0	−2	0	0

Table 5.1: Character table of D_{2d}.

element, $s \to R(s)$, such that

$$R(s_1 s_2) = R(s_1)R(s_2), \tag{5.1}$$

for all group elements s_1, s_2. The representation of the symmetry transformation obtained by applying s_2 and then s_1 is simply the product of the linear transformations assigned to s_1 and s_2. This condition can be interpreted as saying that the linear transformations of the representation are compatible with the group structure. The dimension of a representation refers to the dimension of the vector space the elements of the representation act on. There is no upper limit to the dimensionality of a representation since we can always combine representations into a larger one, using the direct sum of the linear transformations for each group element. Similarly, representations can be decomposed into lower-dimensional ones if there are subspaces of the representation space that remain invariant under the elements of the representation. A representation that cannot be decomposed further is called 'irreducible'. The irreducible representations (irreps) of a symmetry group are of fundamental importance since all other representations can be built up from them.

The irreps of D_{2d} are are listed in Tab. 5.1, together with the 'characters' of the symmetry elements under each representation. The characters are simply the traces of the transformation matrices corresponding to the groups' elements under each irreducible representation, i.e.

$$\chi_R(s) = \mathrm{Tr}[R(s)]. \tag{5.2}$$

It follows that the character of the identity element E is equal to the dimension of the representation. As can be seen from the table, D_{2d} has four one-dimensional irreps (A_1, A_2, B_1, B_2) and one two-dimensional irrep (E, not to be confused with the identity element!). For the one-dimensional irreps the characters are simply equal to the 1×1 transformation 'matrices'. They indicate how an object (e.g. a wave function) that transforms as a particular irrep changes sign under the symmetry elements of the group. The irrep A_1 leaves the representation space invariant for all symmetry elements. For this reason it is also known as the 'totally symmetric representation', and is trivially an irrep of all point groups.

5.2.2 Symmetry classification of excitations using frontier orbitals

With this background on the point group D_{2d}, we are now in a position to apply representation theory to the electronic states of DP-Mes that are relevant for fission. These insights will be relevant for understanding the structure of coupling between electronic states and molecular vibrations which we derive later in this chapter. For this purpose it is convenient to introduce an approximate description of the electronic states, in terms of Slater determinants built from a small active space of frontier orbitals of DP-Mes. However, using the fully delocalised frontier orbitals (Fig. 5.4) for this makes the resulting wave functions difficult to interpret. To address this issue, we perform an orthogonal transformation in the HOMO−1/HOMO and LUMO/LUMO+1 subspaces, respectively:

$$h_{\mathrm{A}} = \frac{1}{\sqrt{2}}(|\mathrm{HOMO}-1\rangle - |\mathrm{HOMO}\rangle), \tag{5.3}$$

$$h_{\mathrm{B}} = \frac{1}{\sqrt{2}}(|\mathrm{HOMO}-1\rangle + |\mathrm{HOMO}\rangle), \tag{5.4}$$

and

$$\ell_{\mathrm{A}} = \frac{1}{\sqrt{2}}(|\mathrm{LUMO}+1\rangle - |\mathrm{LUMO}\rangle), \tag{5.5}$$

$$\ell_{\mathrm{B}} = \frac{1}{\sqrt{2}}(|\mathrm{LUMO}+1\rangle + |\mathrm{LUMO}\rangle). \tag{5.6}$$

Here, the subscripts A and B refer to the two pentacene units of DP-Mes. The unit-localised orbitals resulting from this transformation are shown in Fig. 5.5. By construction, this set is orthogonal and the new orbitals remain valid eigenfunctions due to the energetic degeneracy in the HOMO and LUMO spaces as a result of the orthogonal geometry of DP-Mes (cf. Fig. 5.4). Normally, obtaining approximately localised orthogonal orbitals in an extended system requires some form of Löwdin orthogonalisation [7]. In our case, however, this is obviated by the special geometric properties of the DP-Mes molecule.

In the next step, we use these orbitals to write down approximate wave functions for the electronic states of interest, following Ref. [7]. The authors use a minimal basis which consists of the HOMO and LUMO orbitals of each unit of a dimer. This basis is sufficient for a first approximation of the low-energy electronic states of DP-Mes, which are all dominated by transitions between HOMOs and LUMOs of the pentacene units. At this level of description, the ground state is given by the following single Slater determinant:

$$\mathrm{GS} = |h_{\mathrm{A}}\alpha h_{\mathrm{A}}\beta h_{\mathrm{B}}\alpha h_{\mathrm{B}}\beta|, \tag{5.7}$$

where α and β label the electron spin states. The interpretation is straightforward, namely each localised HOMO orbital is doubly occupied. The antisymmetrisation of the Slater

determinant takes care of the spin adaption, resulting in a pure singlet. Next, we consider the locally excited states. There are two of them, since there are two pentacene units, on either of which the excitation can reside. Naively, one would take the ground-state determinant and simply promote one of the electrons to the respective LUMO orbital:

$$\mathrm{LE}_{\mathrm{A}}^{?} \quad = \quad |h_{\mathrm{A}}\alpha\ell_{\mathrm{A}}\beta h_{\mathrm{B}}\alpha h_{\mathrm{B}}\beta|. \tag{5.8}$$

The problem becomes apparent when we notice that this choice breaks the (anti)symmetry between the spin labels. Hence, the wave function as written is not a pure singlet state. We need to explicitly take care of the correct symmetry adaptation,

$$\mathrm{LE}_{\mathrm{A}} \quad = \quad \frac{1}{\sqrt{2}}\Big[|h_{\mathrm{A}}\alpha\ell_{\mathrm{A}}\beta h_{\mathrm{B}}\alpha h_{\mathrm{B}}\beta| - |h_{\mathrm{A}}\beta\ell_{\mathrm{A}}\alpha h_{\mathrm{B}}\alpha h_{\mathrm{B}}\beta|\Big], \tag{5.9}$$

and analogously,

$$\mathrm{LE}_{\mathrm{B}} \quad = \quad \frac{1}{\sqrt{2}}\Big[|h_{\mathrm{A}}\alpha h_{\mathrm{A}}\beta h_{\mathrm{B}}\alpha\ell_{\mathrm{B}}\beta| - |h_{\mathrm{A}}\alpha h_{\mathrm{A}}\beta h_{\mathrm{B}}\beta\ell_{\mathrm{B}}\alpha|\Big]. \tag{5.10}$$

The wave functions of the CT states look very similar, the difference being that the electron is promoted not to the LUMO of the same pentacene unit, but rather to the LUMO of the other unit:

$$\mathrm{CT}_{\mathrm{A}} \quad = \quad \frac{1}{\sqrt{2}}\Big[|h_{\mathrm{A}}\alpha\ell_{\mathrm{B}}\beta h_{\mathrm{B}}\alpha h_{\mathrm{B}}\beta| - |h_{\mathrm{A}}\beta\ell_{\mathrm{B}}\alpha h_{\mathrm{B}}\alpha h_{\mathrm{B}}\beta|\Big], \tag{5.11}$$

$$\mathrm{CT}_{\mathrm{B}} \quad = \quad \frac{1}{\sqrt{2}}\Big[|h_{\mathrm{A}}\alpha h_{\mathrm{A}}\beta h_{\mathrm{B}}\alpha\ell_{\mathrm{A}}\beta| - |h_{\mathrm{A}}\alpha h_{\mathrm{A}}\beta h_{\mathrm{B}}\beta\ell_{\mathrm{A}}\alpha|\Big], \tag{5.12}$$

Because of the equivalence of A and B, the thus defined states are degenerate and will hybridise into (anti)symmetric linear combinations, as pointed out earlier,

$$\mathrm{LE}^{\pm} \quad = \quad \frac{1}{\sqrt{2}}\left[\mathrm{LE}_{\mathrm{A}} \pm \mathrm{LE}_{\mathrm{B}}\right], \tag{5.13}$$

$$\mathrm{CT}^{\pm} \quad = \quad \frac{1}{\sqrt{2}}\left[\mathrm{CT}_{\mathrm{A}} \pm \mathrm{CT}_{\mathrm{B}}\right]. \tag{5.14}$$

We remind the reader that LE^{+} is optically bright relative to the ground state since the transition dipoles add constructively, whereas they cancel for LE^{-}, resulting in a dark state. Another consequence of the interaction of transition dipoles is that LE^{+} is lower in energy.

The final state to consider is the correlated triplet pair TT. Its wave function in our minimal basis is given by the expression [7]

$$\begin{aligned}\mathrm{TT} = \frac{1}{\sqrt{3}}\Big[&|h_{\mathrm{A}}\alpha\ell_{\mathrm{A}}\alpha h_{\mathrm{B}}\beta\ell_{\mathrm{B}}\beta| + |h_{\mathrm{A}}\beta\ell_{\mathrm{A}}\beta h_{\mathrm{B}}\alpha\ell_{\mathrm{B}}\alpha| \\ &- \frac{1}{2}(|h_{\mathrm{A}}\alpha\ell_{\mathrm{A}}\beta h_{\mathrm{B}}\alpha\ell_{\mathrm{B}}\beta| + |h_{\mathrm{A}}\alpha\ell_{\mathrm{A}}\beta h_{\mathrm{B}}\beta\ell_{\mathrm{B}}\alpha| + |h_{\mathrm{A}}\beta\ell_{\mathrm{A}}\alpha h_{\mathrm{B}}\alpha\ell_{\mathrm{B}}\beta| + |h_{\mathrm{A}}\beta\ell_{\mathrm{A}}\alpha h_{\mathrm{B}}\beta\ell_{\mathrm{B}}\alpha|)\Big].\end{aligned} \tag{5.15}$$

	E	$2S_4$	C_2	$2C_2'$	$2\sigma_d$
h_A	$+h_\mathrm{A}$	$\mp h_\mathrm{B}$	$-h_\mathrm{A}$	$\pm h_\mathrm{B}$	$\mp h_\mathrm{A}$
h_B	$+h_\mathrm{B}$	$\pm h_\mathrm{A}$	$-h_\mathrm{B}$	$\pm h_\mathrm{A}$	$\pm h_\mathrm{B}$
ℓ_A	$+\ell_\mathrm{A}$	$\pm \ell_\mathrm{B}$	$-\ell_\mathrm{A}$	$\mp \ell_\mathrm{B}$	$\mp \ell_\mathrm{A}$
ℓ_B	$+\ell_\mathrm{B}$	$\mp \ell_\mathrm{A}$	$-\ell_\mathrm{B}$	$\mp \ell_\mathrm{A}$	$\pm \ell_\mathrm{B}$

Table 5.2: Transformations of localised frontier orbitals under the symmetry elements of D_{2d}.

The spatial wave function of this state can be interpreted straightforwardly. It is doubly locally excited, with one electron promoted from the HOMO to the LUMO on each unit. However, the interpretation of the spin part is less transparent. To elucidate what is going on, we write it in terms of its components on the two pentacene units:

$$\frac{1}{\sqrt{3}}\left[|\alpha\alpha\rangle_\mathrm{A}\otimes|\beta\beta\rangle_\mathrm{B} + |\beta\beta\rangle_\mathrm{A}\otimes|\alpha\alpha\rangle_\mathrm{B} - \frac{1}{\sqrt{2}}\left(|\alpha\beta\rangle_\mathrm{A}+|\beta\alpha\rangle_\mathrm{A}\right)\otimes\frac{1}{\sqrt{2}}\left(|\alpha\beta\rangle_\mathrm{B}+|\beta\alpha\rangle_\mathrm{B}\right)\right]. \tag{5.16}$$

It is now apparent that the spin wave function is composed entirely of local two-electron triplets. One can verify that it is also an eigenstate of the total spin operator with eigenvalue zero, i.e. an overall singlet state.

Using this picture, one can now classify the electronic states according to irreducible representations of the point group. First, one considers how the minimal orbital basis h_A, h_B, ℓ_A, ℓ_B transforms under the symmetry operations of D_{2d}. For example a C_2 rotation about the principle axis induces the mapping $h_\mathrm{A}\to -h_\mathrm{A}$, $h_\mathrm{B}\to -h_\mathrm{B}$, $\ell_\mathrm{A}\to -\ell_\mathrm{A}$ and $\ell_\mathrm{B}\to -\ell_\mathrm{B}$. A systematic summary of these transformations is presented in Tab. 5.2. Substituting these transformations into the wave functions makes it possible work out how the electronic states transform under the symmetry elements. In doing so, we can focus on the how the spatial part of the wave function transforms, and ignore transformations of the spin part. This is because we can always choose a spin quantisation axis that is invariant under a given symmetry element. In addition, all the states of interest are singlets, i.e. the form of their spin wave functions is necessarily independent of the choice of spin quantisation axis.

We will now demonstrate this symmetry analysis using the example of the locally excited states $\mathrm{LE}^{\pm}$, and then just state the remaining results in tabular form in the interest of brevity. It is clear that we do not need to explicitly check the effect of the trivial element E since it leaves every state invariant by definition. Similarly, we can notice that C_2 acts trivially as well since it introduces a minus sign to each orbital, but does not transform between them. These minus signs necessarily cancel because we are looking at four-electron wave functions. The remaining symmetry elements to consider are $2S_4$, $2C_2'$, and $2\sigma_d$.

Starting with $2S_4$, we evaluate its action on $\mathrm{LE_A}$,

$$\begin{aligned}
\mathrm{LE_A} &= \frac{1}{\sqrt{2}}\Big[+|h_\mathrm{A}\alpha\ell_\mathrm{A}\beta h_\mathrm{B}\alpha h_\mathrm{B}\beta| - |h_\mathrm{A}\beta\ell_\mathrm{A}\alpha h_\mathrm{B}\alpha h_\mathrm{B}\beta|\Big] \\
&\xrightarrow{2S_4} \frac{1}{\sqrt{2}}\Big[-|h_\mathrm{B}\alpha\ell_\mathrm{B}\beta h_\mathrm{A}\alpha h_\mathrm{A}\beta| + |h_\mathrm{B}\beta\ell_\mathrm{B}\alpha h_\mathrm{A}\alpha h_\mathrm{A}\beta|\Big] \\
&= \frac{1}{\sqrt{2}}\Big[-|h_\mathrm{A}\alpha h_\mathrm{A}\beta h_\mathrm{B}\alpha\ell_\mathrm{B}\beta| + |h_\mathrm{A}\alpha h_\mathrm{A}\beta h_\mathrm{B}\beta\ell_\mathrm{B}\alpha|\Big] \\
&= -\mathrm{LE_B}. \qquad (5.17)
\end{aligned}$$

In analogous fashion we obtain

$$\mathrm{LE_B} \xrightarrow{2S_4} -\mathrm{LE_A}. \qquad (5.18)$$

Now it follows that

$$\begin{aligned}
\mathrm{LE^+} &= \frac{1}{\sqrt{2}}\left[\mathrm{LE_A} + \mathrm{LE_B}\right] \\
&\xrightarrow{2S_4} \frac{1}{\sqrt{2}}\left[-\mathrm{LE_B} - \mathrm{LE_A}\right] \\
&= -\frac{1}{\sqrt{2}}\left[\mathrm{LE_A} + \mathrm{LE_B}\right] = -\mathrm{LE^+}, \qquad (5.19)
\end{aligned}$$

and

$$\begin{aligned}
\mathrm{LE^-} &= \frac{1}{\sqrt{2}}\left[\mathrm{LE_A} - \mathrm{LE_B}\right] \\
&\xrightarrow{2S_4} \frac{1}{\sqrt{2}}\left[-\mathrm{LE_B} + \mathrm{LE_A}\right] \\
&= \frac{1}{\sqrt{2}}\left[\mathrm{LE_A} - \mathrm{LE_B}\right] = \mathrm{LE^-}. \qquad (5.20)
\end{aligned}$$

Under the assumption that these states do in fact transform as irreps (which turns out to be the case) this result already tells us that $\mathrm{LE^+}$ can be assigned to one of the irreps B_1, B_2, whereas $\mathrm{LE^-}$ belongs to either A_1 or A_2 (see Tab. 5.1).

Turning to the symmetry elements $2C_2'$, we repeat the procedure to obtain

$$\begin{aligned}
\mathrm{LE_A} &= \frac{1}{\sqrt{2}}\Big[+|h_\mathrm{A}\alpha\ell_\mathrm{A}\beta h_\mathrm{B}\alpha h_\mathrm{B}\beta| - |h_\mathrm{A}\beta\ell_\mathrm{A}\alpha h_\mathrm{B}\alpha h_\mathrm{B}\beta|\Big] \\
&\xrightarrow{2C_2'} \frac{1}{\sqrt{2}}\Big[-|h_\mathrm{B}\alpha\ell_\mathrm{B}\beta h_\mathrm{A}\alpha h_\mathrm{A}\beta| + |h_\mathrm{B}\beta\ell_\mathrm{B}\alpha h_\mathrm{A}\alpha h_\mathrm{A}\beta|\Big] \\
&= \frac{1}{\sqrt{2}}\Big[-|h_\mathrm{A}\alpha h_\mathrm{A}\beta h_\mathrm{B}\alpha\ell_\mathrm{B}\beta| + |h_\mathrm{A}\alpha h_\mathrm{A}\beta h_\mathrm{B}\beta\ell_\mathrm{B}\alpha|\Big] \\
&= -\mathrm{LE_B}, \qquad (5.21)
\end{aligned}$$

and

$$\mathrm{LE_B} \xrightarrow{2C_2'} -\mathrm{LE_A}, \qquad (5.22)$$

state	E (eV)	irrep	E	$2S_4$	C_2	$2C_2'$	$2\sigma_d$
GS	0.00	A_1	$+1$	$+1$	$+1$	$+1$	$+1$
TT	1.87	A_1	$+1$	$+1$	$+1$	$+1$	$+1$
LE^+	2.15	B_2	$+1$	-1	$+1$	-1	$+1$
LE^-	2.28	A_1	$+1$	$+1$	$+1$	$+1$	$+1$
CT^+	2.75	A_2	$+1$	$+1$	$+1$	-1	-1
CT^-	2.76	B_1	$+1$	-1	$+1$	$+1$	-1

Table 5.3: Excitation energies and symmetry classification of electronic states.

in complete equivalence to the previous case. The differences in sign changes between the two symmetry elements cancel in the Slater determinants. Hence, we also have

$$\mathrm{LE}^+ \xrightarrow{2C_2'} -\mathrm{LE}^+, \tag{5.23}$$

$$\mathrm{LE}^- \xrightarrow{2C_2'} \mathrm{LE}^+. \tag{5.24}$$

Finally, the reflections $2\sigma_d$ leave the orbitals invariant up to changes of sign. For orbitals belonging to the same pentacene unit (A or B) these changes of sign are the same under both σ_d reflections. As the locally excited states have two electrons per unit, the signs neutralise. Hence, both LE^+ and LE^- are invariant under the $2\sigma_d$ symmetry elements.

In conclusion, we have shown that LE^+ transforms as the irreducible representation B_2, whereas LE^- transforms according to the totally symmetric representation A_1. The transformation properties and assignments of the remaining states can be found in Tab. 5.3. In addition to LE^-, both the ground state GS and the triplet pair TT transform as the totally symmetric representation A_1.

5.3 Coupling electronic states to molecular vibrations

In the next step, we consider the interplay between the low-energy excitations and vibrational modes of the DP-Mes molecule. The section is structured as follows: first, we review the molecular Schrödinger equation which provides the physical basis of the discussion, largely following the review article by Worth & Cederbaum [137]. This includes a breakdown of the alternative treatments of this equation in terms of the adiabatic picture and the more tractable diabatic picture. We introduce the diabatic potential matrix which describes the coupling of electronic states and nuclear motion. It is convenient to describe the nuclear motion in terms of normal mode coordinates which are also briefly reviewed. This prepares the ground for a discussion of an approximate parametrisation of the potential matrix (and thereby the molecular Hamiltonian) using electronic structure methods.

5.3.1 The molecular Schrödinger equation

The ultimate goal of this chapter is to (approximately) solve the full molecular Schrödinger equation of the DP-Mes system, including both electronic and nuclear dynamics:

$$i\hbar\frac{\partial\Psi}{\partial t} = \hat{H}\Psi. \tag{5.25}$$

The full Hamiltonian can be decomposed as follows:

$$\hat{H}(\mathbf{R},\mathbf{r}) = \hat{T}_n(\mathbf{R}) + \hat{H}_{el}(\mathbf{R},\mathbf{r}), \tag{5.26}$$

where $\hat{T}_n$ is the nuclear kinetic energy operator and the remaining terms are collected in the familiar electronic Hamiltonian, $\hat{H}_{el}$. In the notation we employ here, $\mathbf{R}$ refers to the nuclear coordinates, and $\mathbf{r}$ to the electronic coordinates. The electronic Hamiltonian is parametrically dependent on the nuclear coordinates. Up until this point, we have always adopted the Born-Oppenheimer approximation which separates electronic and nuclear dynamics by assuming that the nuclei provide a static background for the electrons.

5.3.2 Adiabatic picture

The adiabatic electronic wave functions are defined as the solutions of the clamped nuclei eigenvalue equation

$$\hat{H}_{el}\Phi_i(\mathbf{r};\mathbf{R}) = V_i(\mathbf{R})\Phi_i(\mathbf{r};\mathbf{R}), \tag{5.27}$$

where i labels the electronic eigenstates or adiabatic states. The equation depends on the nuclear configuration $\mathbf{R}$, since the electronic Hamiltonian depends parametrically on $\mathbf{R}$. Hence, the adiabatic wave functions are also parametrically dependent on $\mathbf{R}$. The energy of the adiabatic states in dependence of the nuclear coordinates defines the adiabatic potential energy surfaces $V_i(\mathbf{R})$. Within in the Born-Oppenheimer (or adiabatic) approximation, these potential energy surfaces are independent. The nuclei simply move along the surfaces, and there is no coupling between them which would allow parts of the wave function to transfer from one surface to another one. In this picture, transfer can only happen at points where potential surfaces intersect. However, it turns out that the separation of electronic and nuclear dynamics breaks down severely at such points.

Without ignoring the coupling of the adiabatic surfaces, the adiabatic wave functions still provide a useful basis for restating the molecular Schrödinger equation. Using them, the Schrödinger equation can be rewritten as a matrix equation:

$$[\hat{T}_n\mathbf{1} + \mathbf{V} - \hat{\mathbf{\Lambda}}]\boldsymbol{\chi} = i\hbar\frac{\partial\boldsymbol{\chi}}{\partial t}, \tag{5.28}$$

where $\boldsymbol{\chi}$ is the nuclear wave function with components on the adiabatic surfaces, $\mathbf{V}$ the diagonal matrix of the potential energies of the electronic surfaces (Eq. (5.27)), and $\hat{\mathbf{\Lambda}}$ is the matrix of nonadiabatic coupling operators. As the name suggests, this matrix describes the coupling of the adiabatic surfaces, removing the independence assumption of the adiabatic approximation (hence 'nonadiabatic'). This matrix is challenging to treat since the components of $\hat{\mathbf{\Lambda}}$ are non-local derivative operators. More specifically, the matrix elements contain terms of the form $\langle\Phi_i|\nabla\Phi_j\rangle$ and $\langle\Phi_i|\nabla^2\Phi_j\rangle$.

5.3.3 Diabatic picture

Near some nuclear configuration of interest, the problem can be simplified greatly by switching to the diabatic picture. The diabatic picture is attained by means of a unitary transformation at each nuclear configuration

$$\tilde{\Phi} = \mathbf{S}(\mathbf{R})\Phi, \tag{5.29}$$

where $\mathbf{S}$ is square with dimension equal to the number of electronic states under consideration. This transformation can be chosen such that the derivative coupling terms are cancelled, and only local coupling terms (i.e. without derivatives) remain. In the diabatic basis the molecular Schrödinger equation then takes the form

$$[\hat{T}_n\mathbf{1} + \mathbf{W}]\tilde{\boldsymbol{\chi}} = i\hbar\frac{\partial\tilde{\boldsymbol{\chi}}}{\partial t}. \tag{5.30}$$

In the diabatic picture all the couplings between electronic states are contained in the diabatic potential matrix $\mathbf{W}$ which has only local terms and is therefore much easier to deal with. The diabatic basis can be fixed by the requirement that it is equal to the adiabatic basis at a suitable point (here $\mathbf{S}$ is equal to the identity). In the case of DP-Mes the relaxed ground state provides such a point naturally. At this geometry (also called the 'Franck-Condon geometry'), the adiabatic states of DP-Mes are well-distinguished by their different electronic configurations and symmetries. This makes them suitable for providing diabatic templates onto which the electronic wave function can be projected at nearby geometries.

Assuming that in the course of the dynamics the geometrical change is not too large, one can obtain an approximate description of the dynamics using a low-order expansion of $\mathbf{W}$ around some nuclear configuration $\mathbf{R}_0$. If one is concerned with dynamics following photoexcitation, as is the case for fission, a convenient choice is the Franck-Condon point. In DP-Mes this refers to the photoexcitable state LE^+ at the Franck-Condon geometry. If we take the diabatic basis to be equal to the adiabatic basis at $\mathbf{R}_0$, we obtain the expansion

$$\mathbf{W}(\mathbf{R}) = \mathbf{V}(\mathbf{R}_0) + \mathbf{W}^{(1)} + \mathbf{W}^{(2)} + \ldots \tag{5.31}$$

As we take the diabatic basis to be equal to the adiabatic basis at $\mathbf{R_0}$, the zeroth-order term $\mathbf{V}(\mathbf{R}_0)$ is diagonal with the adiabatic energies as the non-zero entries. The first-order matrix elements can be expressed in the adiabatic basis at $\mathbf{R}_0$ as [137]

$$W^{(1)}_{(\Phi_i\Phi_j)} = \sum_\alpha \left[\left\langle \Phi_i \left| \frac{\partial \hat{H}_{el}}{\partial R_\alpha} \right| \Phi_j \right\rangle \right] R'_\alpha, \tag{5.32}$$

where $\mathbf{R}'$ is the displacement of the nuclei from $\mathbf{R}_0$. The index α labels the nuclear coordinates. The diagonal coefficients are simply the adiabatic forces associated with the respective electronic states at the Franck-Condon geometry. In order to calculate the off-diagonal elements, we employ the aforementioned frontier orbital description of the electronic states as we lay out in the following.

5.3.4 Normal modes and symmetry constraints on coupling

A first-order expansion of the potential matrix is insufficient for a satisfactory description since the resulting Hamiltonian is generically unbounded from below. Hence, higher-order terms in the nuclear coordinates are necessary to obtain physically sensible behaviour. A straightforward way to achieve this, is to include the adiabatic ground-state Hamiltonian to second order in nuclear displacements, namely the vibrational Hamiltonian of the system. It can be diagonalised yielding normal coordinates which behave as independent harmonic oscillators:

$$H_0(\mathbf{Q}) = \sum_n \frac{\hbar\omega_n}{2} \left(-\frac{\partial^2}{\partial Q_n^2} + Q_n^2 \right), \tag{5.33}$$

with the ground-state normal coordinates Q_n in dimensionless mass-frequency-scaled units. The assumption is that the differences between the vibrational frequencies for the relevant electronic states are small. This is justified to the extent that electron reconfiguration in the frontier orbital space between states can be considered small relative to the bulk of the electrons.

As is the case with the electronic states, the vibrational normal modes can be assigned to irreducible representations of the point group. These symmetry assignments together with the assignments of the electronic states determine which elements of the coupling matrix are non-zero. To see this, we rewrite Eq. (5.32) in terms of normal coordinates:

$$W^{(1)}_{(\Phi_i\Phi_j)} = \sum_n \left[\left\langle \Phi_i \left| \frac{\partial \hat{H}_{el}}{\partial Q_n} \right| \Phi_j \right\rangle \right] Q_n. \tag{5.34}$$

In order for a matrix element to take a non-zero value, the product of the irreps of its constituent wave functions and operators has to transform as the totally symmetric representation. The reason is that matrix elements are scalars which are necessarily invariant

	A_1	A_2	B_1	B_2
A_1	A_1	A_2	B_1	B_2
A_2	A_2	A_1	B_2	B_1
B_1	B_1	B_2	A_1	A_2
B_2	B_2	B_1	A_2	A_1

Table 5.4: Product table of 1D-irreps of D_{2d}.

under the symmetry transformations of the system. A non-zero scalar can only stay invariant if it transforms according to the totally symmetric representation. A zero scalar, on the other hand, remains invariant under all irreps. For our one-dimensional irreps the product of irreps is simply obtained by taking the product of the respective signs for each symmetry element. A product table of the one-dimensional irreps of D_{2d} can be found in Tab. 5.4. Note that only the product of an irrep with itself yields the totally symmetric representation A_1. Hence, if the wave functions transform according to irreps R_i and R_j, the operator $\partial\hat{H}_{el}/\partial Q_n$ must transform as $R_i \cdot R_j$ to yield a non-zero matrix element. Since the electronic Hamiltonian shares the symmetry of the molecule, the operator $\partial\hat{H}_{el}/\partial Q_n$ transforms in the same way as the normal mode coordinate Q_n. For example, modes contributing to the coupling between LE^+ (B_2) and CT^+ (A_2) necessarily transform as B_1 (see Fig. 5.6 for an example of a B_1 mode). The relationships between symmetries of electronic states and coupling vibrational modes are systematically summarised in Fig. 5.7.

5.3.5 Derivation of off-diagonal matrix elements

To approximately evaluate the off-diagonal elements of the diabatic potential matrix to first order we can now go ahead and substitute the frontier orbital representations of the electronic states into Eq. (5.32). This is a relatively crude approximation in terms of the representational power of the basis, but more importantly, it correctly captures the symmetries and spin structures of the relevant electronic states. In a slight abuse of notation we drop the superscript (1) and define

$$W_{(\Phi_i\Phi_j)} \equiv \sum_\alpha \left[\left\langle \Phi_i \left| \frac{\partial \hat{H}_{el}}{\partial R_\alpha} \right| \Phi_j \right\rangle \right] R'_\alpha \tag{5.35}$$

$$\equiv \langle \Phi_i | \hat{W} | \Phi_j \rangle. \tag{5.36}$$

We note that $\hat{W}$ is a one-body operator as a results of the derivative of the electronic Hamiltonian with respect to the nuclear coordinates. The two-body part (i.e. the electron-electron interaction) drops out when taking the derivative since it does not depend on the nuclear coordinates. This means that we can evaluate matrix elements of $\hat{W}$ between Slater determinants using the Slater-Condon rules for one-body operators. Let Ψ be a Slater

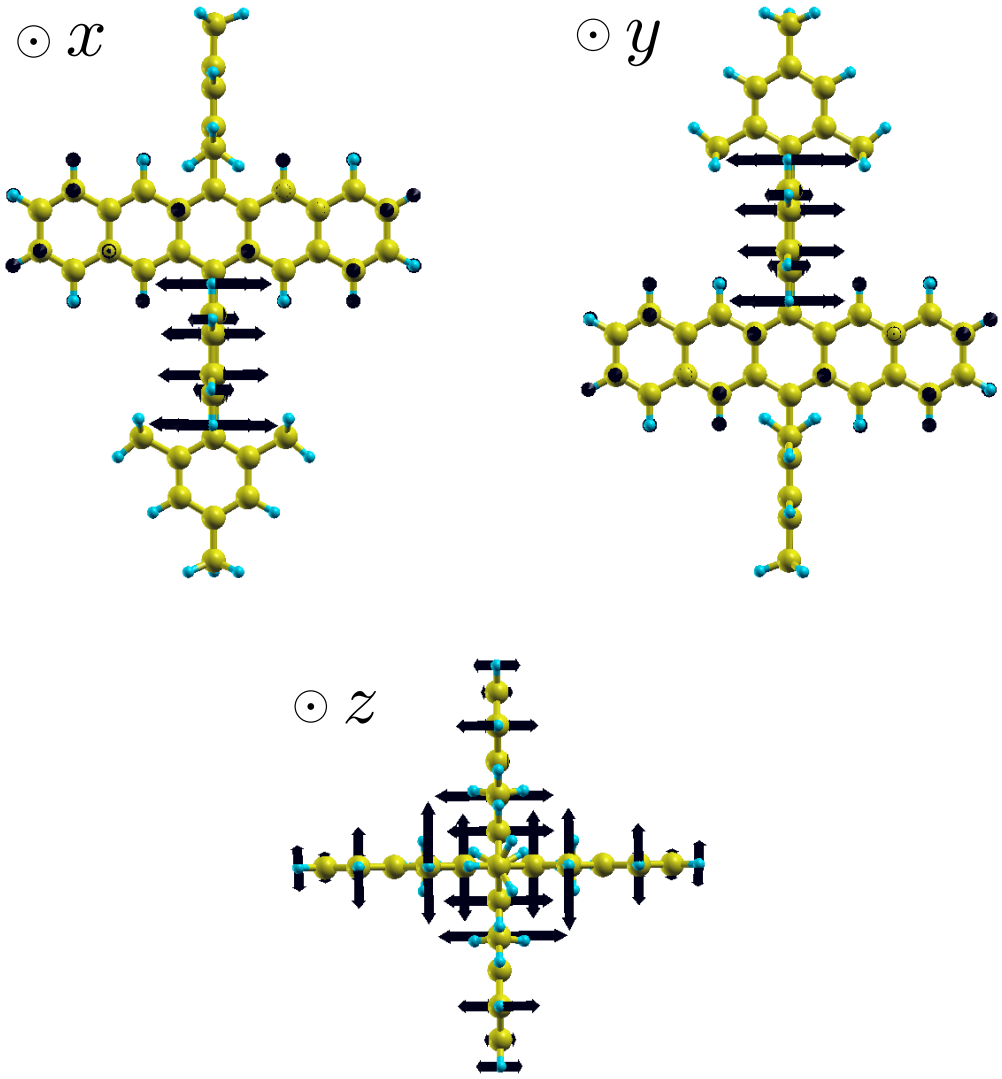

Figure 5.6: Normal mode number 99 of DP-Mes; it transforms according to the B_1 irrep of the D_{2d} point group and has a calculated vibrational frequency of 720.8 cm^{-1}.

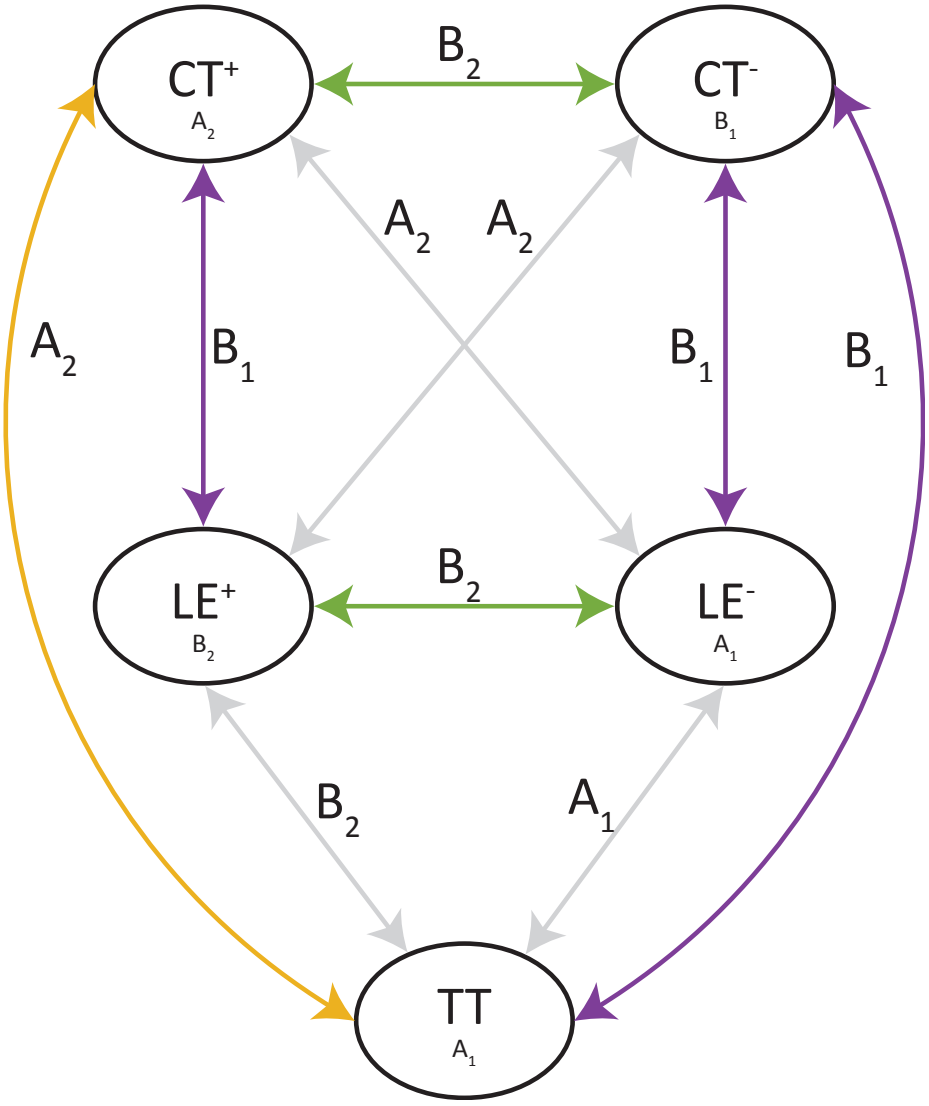

Figure 5.7: Electronic states with irreps in the symmetry group D_{2d}. The lines indicate vibrational coupling and the symmetries of the corresponding normal modes. The grey lines involve 2-electron transfer and do not contribute to the coupling matrix to first order. Courtesy of F. A. Y. N. Schröder.

determinant constructed from spin-orbitals ϕ_i. Then we use the notation Ψ_m^p to denote the Slater determinant that results from replacing spin-orbital ϕ_m with spin-orbital ϕ_p in the determinant Ψ. The Slater-Condon rules for a one-body operator can then be stated as follows:

$$\langle\Psi|\hat{W}|\Psi\rangle = \sum_i \langle\phi_i|\hat{W}|\phi_i\rangle, \tag{5.37}$$

$$\langle\Psi|\hat{W}|\Psi_m^p\rangle = \langle\phi_m|\hat{W}|\phi_p\rangle. \tag{5.38}$$

All matrix elements between Slater determinants that differ by two or more spin-orbitals evaluate to zero.

We begin by considering the locally excited states (before anti/symmetrisation), reminding the reader of their expressions in terms of the frontier-orbital basis,

$$\mathrm{LE_A} = \frac{1}{\sqrt{2}}\Big[|h_\mathrm{A}\alpha\ell_\mathrm{A}\beta h_\mathrm{B}\alpha h_\mathrm{B}\beta| - |h_\mathrm{A}\beta\ell_\mathrm{A}\alpha h_\mathrm{B}\alpha h_\mathrm{B}\beta|\Big], \tag{5.39}$$

$$\mathrm{LE_B} = \frac{1}{\sqrt{2}}\Big[|h_\mathrm{A}\alpha h_\mathrm{A}\beta h_\mathrm{B}\alpha\ell_\mathrm{B}\beta| - |h_\mathrm{A}\alpha h_\mathrm{A}\beta h_\mathrm{B}\beta\ell_\mathrm{B}\alpha|\Big]. \tag{5.40}$$

In the expression for $\langle\mathrm{LE_A}|\hat{W}|\mathrm{LE_A}\rangle$ we only need to consider the interaction of each of the two terms with itself since the other combinations differ by two spin-orbitals. Then, applying the first Slater-Condon rule for identical spin-orbitals (Eq. (5.37)) yields

$$\langle\mathrm{LE_A}|\hat{W}|\mathrm{LE_A}\rangle = \langle h_\mathrm{A}|\hat{W}|h_\mathrm{A}\rangle + \langle\ell_\mathrm{A}|\hat{W}|\ell_\mathrm{A}\rangle + 2\langle h_\mathrm{B}|\hat{W}|h_\mathrm{B}\rangle. \tag{5.41}$$

Completely analogously, one also obtains

$$\langle\mathrm{LE_B}|\hat{W}|\mathrm{LE_B}\rangle = \langle h_\mathrm{B}|\hat{W}|h_\mathrm{B}\rangle + \langle\ell_\mathrm{B}|\hat{W}|\ell_\mathrm{B}\rangle + 2\langle h_\mathrm{A}|\hat{W}|h_\mathrm{A}\rangle. \tag{5.42}$$

Note that there are technically contributions from all the occupied orbitals below the HOMOs when evaluating the first Slater-Condon rule. However, these contributions ultimately cancel for the off-diagonal matrix elements, so we do not include them here.

Furthermore, we have

$$\langle\mathrm{LE_A}|\hat{W}|\mathrm{LE_B}\rangle = 0, \tag{5.43}$$

since we need to exchange two electrons to get from one state to the other. Now, we can evaluate the matrix element between the two locally excited eigenstates, i.e.

$$\begin{aligned}\langle\mathrm{LE}^+|\hat{W}|\mathrm{LE}^-\rangle &= \frac{1}{2}\Big[\langle\mathrm{LE_A}|\hat{W}|\mathrm{LE_A}\rangle - \langle\mathrm{LE_A}|\hat{W}|\mathrm{LE_B}\rangle + \langle\mathrm{LE_B}|\hat{W}|\mathrm{LE_A}\rangle - \langle\mathrm{LE_B}|\hat{W}|\mathrm{LE_B}\rangle\Big] \\ &= \frac{1}{2}\Big[\langle\mathrm{LE_A}|\hat{W}|\mathrm{LE_A}\rangle - \langle\mathrm{LE_B}|\hat{W}|\mathrm{LE_B}\rangle\Big] \\ &= \frac{1}{2}\Big[-\langle h_\mathrm{A}|\hat{W}|h_\mathrm{A}\rangle + \langle h_\mathrm{B}|\hat{W}|h_\mathrm{B}\rangle + \langle\ell_\mathrm{A}|\hat{W}|\ell_\mathrm{A}\rangle - \langle\ell_\mathrm{B}|\hat{W}|\ell_\mathrm{B}\rangle\Big],\end{aligned} \tag{5.44}$$

where the second equality uses the fact that the wave functions of the (approximate) eigenstates are real-valued.

The treatment of the charge-transfer states is analogous. Again, we remind the reader of the expressions:

$$\mathrm{CT_A} = \frac{1}{\sqrt{2}}\Big[|h_\mathrm{A}\alpha\ell_\mathrm{B}\beta h_\mathrm{B}\alpha h_\mathrm{B}\beta| - |h_\mathrm{A}\beta\ell_\mathrm{B}\alpha h_\mathrm{B}\alpha h_\mathrm{B}\beta|\Big], \tag{5.45}$$

$$\mathrm{CT_B} = \frac{1}{\sqrt{2}}\Big[|h_\mathrm{A}\alpha h_\mathrm{A}\beta h_\mathrm{B}\alpha\ell_\mathrm{A}\beta| - |h_\mathrm{A}\alpha h_\mathrm{A}\beta h_\mathrm{B}\beta\ell_\mathrm{A}\alpha|\Big]. \tag{5.46}$$

The matrix elements are obtained in very similar fashion, yielding

$$\langle \mathrm{CT_A}|\hat{W}|\mathrm{CT_A}\rangle = \langle h_\mathrm{A}|\hat{W}|h_\mathrm{A}\rangle + \langle \ell_\mathrm{B}|\hat{W}|\ell_\mathrm{B}\rangle + 2\langle h_\mathrm{B}|\hat{W}|h_\mathrm{B}\rangle, \tag{5.47}$$

$$\langle \mathrm{CT_B}|\hat{W}|\mathrm{CT_B}\rangle = \langle h_\mathrm{B}|\hat{W}|h_\mathrm{B}\rangle + \langle \ell_\mathrm{A}|\hat{W}|\ell_\mathrm{A}\rangle + 2\langle h_\mathrm{A}|\hat{W}|h_\mathrm{A}\rangle, \tag{5.48}$$

$$\langle \mathrm{CT_A}|\hat{W}|\mathrm{CT_B}\rangle = 0. \tag{5.49}$$

Now, the matrix element between the eigenstates evaluates to

$$\langle \mathrm{CT}^+|\hat{W}|\mathrm{CT}^-\rangle = \frac{1}{2}\Big[-\langle h_\mathrm{A}|\hat{W}|h_\mathrm{A}\rangle + \langle h_\mathrm{B}|\hat{W}|h_\mathrm{B}\rangle - \langle \ell_\mathrm{A}|\hat{W}|\ell_\mathrm{A}\rangle + \langle \ell_\mathrm{B}|\hat{W}|\ell_\mathrm{B}\rangle\Big] \tag{5.50}$$

For the next step we consider matrix elements between locally-excited and charge-transfer states. Starting with $\mathrm{LE_A}$ and $\mathrm{CT_A}$ it can be seen that the latter is obtained from the former by moving the excited electron from ℓ_A to ℓ_B. Hence, by the second Slater-Condon rule (Eq. (5.38)),

$$\langle \mathrm{LE_A}|\hat{W}|\mathrm{CT_A}\rangle = \langle \ell_\mathrm{A}|\hat{W}|\ell_\mathrm{B}\rangle, \tag{5.51}$$

and similarly

$$\langle \mathrm{LE_B}|\hat{W}|\mathrm{CT_B}\rangle = \langle \ell_\mathrm{B}|\hat{W}|\ell_\mathrm{A}\rangle = \langle \ell_\mathrm{A}|\hat{W}|\ell_\mathrm{B}\rangle. \tag{5.52}$$

In contrast to the previous cases we also get non-zero cross-terms between states associated with A and B. This is because (say) $\mathrm{CT_B}$ can be obtained from $\mathrm{LE_A}$ by moving a single electron from h_B to h_A. When applying the second Slater-Condon rule we need to make sure that the spin-orbitals in the determinants are ordered such that the matching orbitals are paired up. Achieving that requires a swap of two spin-orbitals in one of the determinants, giving an overall minus sign:

$$\langle \mathrm{LE_A}|\hat{W}|\mathrm{CT_B}\rangle = -\langle h_\mathrm{B}|\hat{W}|h_\mathrm{A}\rangle = -\langle h_\mathrm{A}|\hat{W}|h_\mathrm{B}\rangle, \tag{5.53}$$

and

$$\langle \mathrm{LE_B}|\hat{W}|\mathrm{CT_A}\rangle = -\langle h_\mathrm{A}|\hat{W}|h_\mathrm{B}\rangle. \tag{5.54}$$

Now, we are able to evaluate all the matrix elements between eigenstates of LE and CT type, yielding

$$\begin{aligned}\langle \mathrm{LE}^+|\hat{W}|\mathrm{CT}^+\rangle &= \frac{1}{2}\Big[\langle \mathrm{LE_A}|\hat{W}|\mathrm{CT_A}\rangle + \langle \mathrm{LE_B}|\hat{W}|\mathrm{CT_B}\rangle + \langle \mathrm{LE_A}|\hat{W}|\mathrm{CT_B}\rangle + \langle \mathrm{LE_B}|\hat{W}|\mathrm{CT_A}\rangle\Big] \\ &= \frac{1}{2}\Big[\langle \ell_\mathrm{A}|\hat{W}|\ell_\mathrm{B}\rangle + \langle \ell_\mathrm{A}|\hat{W}|\ell_\mathrm{B}\rangle - \langle h_\mathrm{A}|\hat{W}|h_\mathrm{B}\rangle - \langle h_\mathrm{A}|\hat{W}|h_\mathrm{B}\rangle\Big] \\ &= \langle \ell_\mathrm{A}|\hat{W}|\ell_\mathrm{B}\rangle - \langle h_\mathrm{A}|\hat{W}|h_\mathrm{B}\rangle, \end{aligned} \tag{5.55}$$

$$\begin{aligned}\langle \mathrm{LE}^+|\hat{W}|\mathrm{CT}^-\rangle &= \frac{1}{2}\Big[\langle \mathrm{LE_A}|\hat{W}|\mathrm{CT_A}\rangle - \langle \mathrm{LE_B}|\hat{W}|\mathrm{CT_B}\rangle - \langle \mathrm{LE_A}|\hat{W}|\mathrm{CT_B}\rangle + \langle \mathrm{LE_B}|\hat{W}|\mathrm{CT_A}\rangle\Big] \\ &= \frac{1}{2}\Big[\langle \ell_\mathrm{A}|\hat{W}|\ell_\mathrm{B}\rangle - \langle \ell_\mathrm{A}|\hat{W}|\ell_\mathrm{B}\rangle + \langle h_\mathrm{A}|\hat{W}|h_\mathrm{B}\rangle - \langle h_\mathrm{A}|\hat{W}|h_\mathrm{B}\rangle\Big] \\ &= 0, \end{aligned} \tag{5.56}$$

$$\begin{aligned}\langle \mathrm{LE}^-|\hat{W}|\mathrm{CT}^+\rangle &= \frac{1}{2}\Big[\langle \mathrm{LE_A}|\hat{W}|\mathrm{CT_A}\rangle - \langle \mathrm{LE_B}|\hat{W}|\mathrm{CT_B}\rangle + \langle \mathrm{LE_A}|\hat{W}|\mathrm{CT_B}\rangle - \langle \mathrm{LE_B}|\hat{W}|\mathrm{CT_A}\rangle\Big] \\ &= \frac{1}{2}\Big[\langle \ell_\mathrm{A}|\hat{W}|\ell_\mathrm{B}\rangle - \langle \ell_\mathrm{A}|\hat{W}|\ell_\mathrm{B}\rangle - \langle h_\mathrm{A}|\hat{W}|h_\mathrm{B}\rangle + \langle h_\mathrm{A}|\hat{W}|h_\mathrm{B}\rangle\Big] \\ &= 0, \end{aligned} \tag{5.57}$$

$$\begin{aligned}\langle \mathrm{LE}^-|\hat{W}|\mathrm{CT}^-\rangle &= \frac{1}{2}\Big[\langle \mathrm{LE_A}|\hat{W}|\mathrm{CT_A}\rangle + \langle \mathrm{LE_B}|\hat{W}|\mathrm{CT_B}\rangle - \langle \mathrm{LE_A}|\hat{W}|\mathrm{CT_B}\rangle - \langle \mathrm{LE_B}|\hat{W}|\mathrm{CT_A}\rangle\Big] \\ &= \frac{1}{2}\Big[\langle \ell_\mathrm{A}|\hat{W}|\ell_\mathrm{B}\rangle + \langle \ell_\mathrm{A}|\hat{W}|\ell_\mathrm{B}\rangle + \langle h_\mathrm{A}|\hat{W}|h_\mathrm{B}\rangle + \langle h_\mathrm{A}|\hat{W}|h_\mathrm{B}\rangle\Big] \\ &= \langle \ell_\mathrm{A}|\hat{W}|\ell_\mathrm{B}\rangle + \langle h_\mathrm{A}|\hat{W}|h_\mathrm{B}\rangle. \end{aligned} \tag{5.58}$$

Finally, we look at how TT couples to the other excited states. At this level of approximation, we only need to consider matrix elements with the charge-transfer states. They are related to TT by a single electron transfer, whereas conversion from/to the locally-excited states requires the transfer of two electrons. Once again, we remind the reader of the relevant wave function in the frontier-orbital picture,

$$\begin{aligned}\mathrm{TT} = \frac{1}{\sqrt{3}}\Big[&|h_\mathrm{A}\alpha\ell_\mathrm{A}\alpha h_\mathrm{B}\beta\ell_\mathrm{B}\beta| + |h_\mathrm{A}\beta\ell_\mathrm{A}\beta h_\mathrm{B}\alpha\ell_\mathrm{B}\alpha| \\ &- \frac{1}{2}(|h_\mathrm{A}\alpha\ell_\mathrm{A}\beta h_\mathrm{B}\alpha\ell_\mathrm{B}\beta| + |h_\mathrm{A}\alpha\ell_\mathrm{A}\beta h_\mathrm{B}\beta\ell_\mathrm{B}\alpha| + |h_\mathrm{A}\beta\ell_\mathrm{A}\alpha h_\mathrm{B}\alpha\ell_\mathrm{B}\beta| + |h_\mathrm{A}\beta\ell_\mathrm{A}\alpha h_\mathrm{B}\beta\ell_\mathrm{B}\alpha|)\Big]. \end{aligned} \tag{5.59}$$

To make the subsequent application of the Slater-Condon rules more transparent we permute the spin-orbitals in $\mathrm{CT_A}$ to align better with the order in TT, i.e.

$$\mathrm{CT_A} = \frac{1}{\sqrt{2}}\Big[|h_\mathrm{A}\alpha h_\mathrm{B}\alpha h_\mathrm{B}\beta\ell_\mathrm{B}\beta| - |h_\mathrm{A}\beta h_\mathrm{B}\alpha h_\mathrm{B}\beta\ell_\mathrm{B}\alpha|\Big] \tag{5.60}$$

Accordingly, TT can be broken down into two contributions that can be matched up with the two terms in $\mathrm{CT_A}$, respectively, and remaining terms:

$$\begin{aligned}\mathrm{TT} \;=\; & \frac{1}{\sqrt{3}}\Big[|h_\mathrm{A}\alpha\ell_\mathrm{A}\alpha h_\mathrm{B}\beta\ell_\mathrm{B}\beta| + \frac{1}{2}|h_\mathrm{A}\alpha h_\mathrm{B}\alpha\ell_\mathrm{A}\beta\ell_\mathrm{B}\beta|\Big] \\ & -\frac{1}{\sqrt{3}}\Big[|h_\mathrm{A}\beta h_\mathrm{B}\alpha\ell_\mathrm{A}\beta\ell_\mathrm{B}\alpha| + \frac{1}{2}|h_\mathrm{A}\beta\ell_\mathrm{A}\alpha h_\mathrm{B}\beta\ell_\mathrm{B}\alpha|\Big] \\ & +\frac{1}{2\sqrt{3}}\Big[|h_\mathrm{A}\alpha\ell_\mathrm{A}\beta h_\mathrm{B}\beta\ell_\mathrm{B}\alpha| + |h_\mathrm{A}\beta\ell_\mathrm{A}\alpha h_\mathrm{B}\alpha\ell_\mathrm{B}\beta|\Big], \end{aligned} \tag{5.61}$$

where changes of sign compared to the original expression compensate for rearrangements of spin-orbitals. The first two contributions are related to the respective terms of $\mathrm{CT_A}$ by a transfer of an electron between orbitals ℓ_A and h_B. The remaining terms differ by two spin-orbitals and do not yield a contribution, hence

$$\langle \mathrm{TT}|\hat{W}|\mathrm{CT_A}\rangle \;=\; \sqrt{\frac{3}{2}}\langle \ell_\mathrm{A}|\hat{W}|h_\mathrm{B}\rangle. \tag{5.62}$$

In analogous fashion we have

$$\langle \mathrm{TT}|\hat{W}|\mathrm{CT_B}\rangle \;=\; \sqrt{\frac{3}{2}}\langle \ell_\mathrm{B}|\hat{W}|h_\mathrm{A}\rangle \;=\; \sqrt{\frac{3}{2}}\langle h_\mathrm{A}|\hat{W}|\ell_\mathrm{B}\rangle. \tag{5.63}$$

With this we finally obtain

$$\begin{aligned}\langle \mathrm{TT}|\hat{W}|\mathrm{CT}^\pm\rangle \;&=\; \frac{1}{\sqrt{2}}\Big[\langle \mathrm{TT}|\hat{W}|\mathrm{CT_A}\rangle \pm \langle \mathrm{TT}|\hat{W}|\mathrm{CT_B}\rangle\Big] \\ &=\; \frac{\sqrt{3}}{2}\Big[\langle \ell_\mathrm{A}|\hat{W}|h_\mathrm{B}\rangle \pm \langle h_\mathrm{A}|\hat{W}|\ell_\mathrm{B}\rangle\Big]. \end{aligned} \tag{5.64}$$

All in all, we have derived the following off-diagonal, non-zero contributions to the first-order potential matrix (using compact notation, see Eq. (5.35)):

$$W_{(\mathrm{LE^+LE^-})} \;=\; \frac{1}{2}\left[-W_{(h_\mathrm{A}h_\mathrm{A})} + W_{(h_\mathrm{B}h_\mathrm{B})} + W_{(\ell_\mathrm{A}\ell_\mathrm{A})} - W_{(\ell_\mathrm{B}\ell_\mathrm{B})}\right] \tag{5.65}$$

$$W_{(\mathrm{CT^+CT^-})} \;=\; \frac{1}{2}\left[-W_{(h_\mathrm{A}h_\mathrm{A})} + W_{(h_\mathrm{B}h_\mathrm{B})} - W_{(\ell_\mathrm{A}\ell_\mathrm{A})} + W_{(\ell_\mathrm{B}\ell_\mathrm{B})}\right] \tag{5.66}$$

$$W_{(\mathrm{LE^+CT^+})} \;=\; W_{(\ell_\mathrm{A}\ell_\mathrm{B})} - W_{(h_\mathrm{A}h_\mathrm{B})} \tag{5.67}$$

$$W_{(\mathrm{LE^-CT^-})} \;=\; W_{(\ell_\mathrm{A}\ell_\mathrm{B})} + W_{(h_\mathrm{A}h_\mathrm{B})} \tag{5.68}$$

$$W_{(\mathrm{TT\,CT^\pm})} \;=\; \frac{\sqrt{3}}{2}\left[W_{(\ell_\mathrm{A}h_\mathrm{B})} \pm W_{(h_\mathrm{A}\ell_\mathrm{B})}\right] \tag{5.69}$$

The individual terms $W_{(\phi\psi)}$ in these expressions are matrix elements of $\partial\hat{H}_{el}/\partial\mathbf{R}$ between pairs of one-electron orbitals ϕ and ψ. The relevant part of the electronic Hamiltonian that depends on the nuclear coordinates is the Coulomb potential between nuclei and electrons. This means the terms can be evaluated as the electrostatic 'forces' on the nuclei due to the overlap-density $\rho(\mathbf{r}) = \phi(\mathbf{r})\psi(\mathbf{r})$. These coupling vectors are then transformed to the normal-coordinate basis which is the natural choice for the dynamics calculations described in section 5.4.

5.3.6 Computational details and limitations

The vibrational modes are obtained at the relaxed ground-state geometry, employing analytical Hessians at the cc-pVDZ/B3LYP level of theory. Excited state forces, corresponding to the diagonal elements of W, for $LE^{\pm}$ and $CT^{\pm}$ are calculated from (linear-response) TDDFT gradients at the cc-pVDZ/LC-BLYP level of theory. The frontier molecular orbitals at the cc-pVDZ/LC-BLYP level are also used as inputs for the evaluation of the off-diagonal couplings.

There are a number of limitation of the methods and approximations described. These include treating the normal modes in the harmonic regime, and only accounting for the coupling between vibrations and electronic states to first order in the nuclear displacements. Furthermore, the evaluation of the off-diagonal elements of the potential matrix is based on a description of the electronic states in terms of a small active space of frontier-orbitals only. This is necessary to correctly capture the spin-structure of the states involved in fission, at the expense of the representational power of the basis used. In addition, these wave functions are constructed from Kohn-Sham orbitals which are eigenfunctions of the non-interacting Kohn-Sham system rather than the full electronic Hamiltonian. Since these orbitals are expressed in terms of Gaussian basis functions centred on the nuclei we also do not capture Pulay terms when evaluating the off-diagonal elements of W according to Eq. (5.35). Finally, it should be noted that CT energies from TDDFT, while not severely underestimated thanks to the use of range-separation, come out relatively high. There is a certain amount of tension with lower cDFT estimates of these energies discussed in the next chapter. Partly, this can be explained simply by the fact that we have not included any solvent effects so far. Additionally, we can suspect that the lack of diffuse functions in the basis set and the linear-response nature of the TDDFT calculations play a role here. Both hamper the ability to capture the intra-molecular relaxation of a CT configuration.

Given all these limitations, our parametrisation of the vibronic coupling Hamiltonian of DP-Mes should be considered semi-quantitative.

5.4 Quantum dynamics calculations

In the preceding section we have described a method for constructing a linear vibronic coupling Hamiltonian for the DP-Mes system from DFT. Next, we will briefly outline the methodology behind quantum dynamics calculations using this Hamiltonian, which have been performed by F. A. Y. N. Schröder, describing the dynamics of singlet fission in DP-Mes.

Using slightly more compact notation than before, the linear vibronic Hamiltonian reads

$$\hat{\boldsymbol{H}}_{LVC} = \boldsymbol{H}_S + \sum_{n=1}^{318} \boldsymbol{W}_n \frac{(\hat{b}_n^\dagger + \hat{b}_n)}{\sqrt{2}} + \hat{H}_{vib}, \tag{5.70}$$

where the sum runs over all 318 harmonic normal modes of DP-Mes (108 atoms, hence $3 \times 108 - 6 = 318$ modes). The normal modes are associated with creation and annihilation operators $\hat{b}_n^\dagger$, $\hat{b}_n$. $\boldsymbol{H}_S$ and $\boldsymbol{W}_n$ are 5×5 matrices, corresponding to the five excited states we consider, $\mathrm{LE}^{\pm}$, $\mathrm{CT}^{\pm}$ and TT. The first term $\boldsymbol{H}_S$ is diagonal in the vertical excitation energies of these states. The $\boldsymbol{W}_n$ describe the induced electronic couplings as the system is perturbed along mode n, to first order. The harmonic oscillator Hamiltonians of the normal vibrational modes are collected in the term $\hat{H}_{vib}$.

As written, the Hamiltonian is computationally intractable due to the large number of vibrational modes coupling to the electronic states. In order to reduce the complexity of the Hamiltonian, a k-means clustering analysis of the (normalised) coupling patterns $\boldsymbol{W}_n$ is performed [138]. This makes it possible to group the modes into a minimal set of independent environments i. This clustering analysis results in the discovery of a minimal set of seven independent groups with associated coupling centroids $\overline{\boldsymbol{W}_i}$. Each couples to a single system operator, and each bath can then be mapped onto a harmonic oscillator chain $\hat{H}_{c,i}$ using the orthogonal polynomial transformation [139–141]. Since the clustering analysis is performed after a normalisation step, the relationship of the centroids to the original couplings is

$$\boldsymbol{W}_n = \overline{\boldsymbol{W}}_{i_n} \times \lambda_n, \tag{5.71}$$

where λ_n is the relative coupling strength for mode n. This procedure yields the following form of the Hamiltonian:

$$\hat{\boldsymbol{H}}_{star} = \boldsymbol{H}_S + \sum_{i=1}^{7} \overline{\boldsymbol{W}}_i |\boldsymbol{\lambda}_i| \frac{(\hat{a}_{i,0}^\dagger + \hat{a}_{i,0})}{\sqrt{2}} + \hat{H}_{c,i}, \tag{5.72}$$

with the $\hat{a}_{i,0}^\dagger$ the so-called reaction coordinate (RC) of chain i, and the $\boldsymbol{\lambda}_i$ the vectors of relative coupling strengths of modes belonging to chain i. In this formulation the electronic part of the Hamiltonian only couples directly to the RC of each chain. The independent environments discovered by the clustering procedure closely correspond to the symmetry classification of the normal modes into irreps of the D_{2d} point group. We obtain one chain for modes of A_2 symmetry and two each for modes of A_1, B_1, and B_2 symmetries (see Fig. 5.8). The A_1 modes couple diagonally to all electronic states as tuning modes, while the others act as off-diagonal coupling modes, mixing the states.

The resulting model parameters, together with a table of the most significant coupling modes, can be found in the appendix.

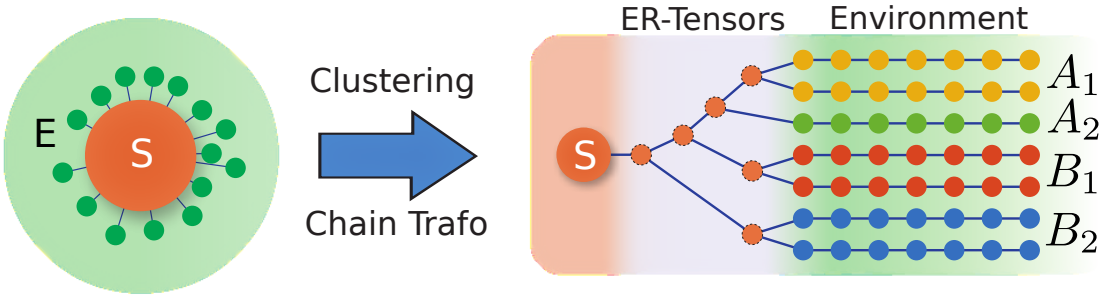

Figure 5.8: Normal modes are clustered according to their coupling to the electronic system, and each cluster is mapped onto a chain model. Each of the groups can be associated with an irreducible representation of D_{2d} and acts as an independent environment. The electronic system is connected to the chains through a tree of entanglement renormalisation (ER) tensors. Courtesy of F. A. Y. N. Schröder.

The model is simulated using a tree tensor network state (TTNS) [142, 143], namely a low-rank tensor approximation to the full system-environment wave function. This allows very efficient and accurate simulations of the system with many explicit quantum degrees of freedom which can also be highly excited. This approach is a multi-dimensional extension of matrix-product state (MPS) approaches to open quantum system dynamics [144, 145]. To illustrate the basic idea of the TTNS method, we briefly outline how a matrix-product state can approximate a many-body wave function. Considering a 1D chain of L subsystems or sites, a general quantum state can be written as

$$|\Psi\rangle = \sum_{\{n_k\}=1}^{d_k} \Psi_{n_1,\ldots,n_L} |n_1,\ldots,n_L\rangle, \tag{5.73}$$

where the n_k index the local Hilbert spaces of sites k with local dimensions d_k. In the MPS approach the single rank-L tensor $\Psi_{n_1,\ldots,n_L}$ describing the amplitudes is approximately decomposed into L rank-3 tensors $\boldsymbol{A}^{n_k}$ which can be interpreted as indexed matrices of size $D_{k-1} \times D_k$,

$$|\Psi_{MPS}\rangle = \sum_{\{n_k\}=1}^{d_k} \mathrm{Tr}\left[\boldsymbol{A}^{n_1}\boldsymbol{A}^{n_2}\cdots\boldsymbol{A}^{n_L}\right] |n_1,\ldots,n_L\rangle\,. \tag{5.74}$$

The amount of entanglement that can be encoded in an MPS state is directly related to the choice of bond dimensions D_k of the matrices. Provided that the bond dimensions can be chosen relatively small while retaining a satisfactory approximation to the quantum state, the MPS decomposition makes it possible to hugely reduce the numerical resources necessary to simulate the many-body dynamics of the system. The MPS representation can be straightforwardly used to for each of the seven chains of transformed oscillators. However,

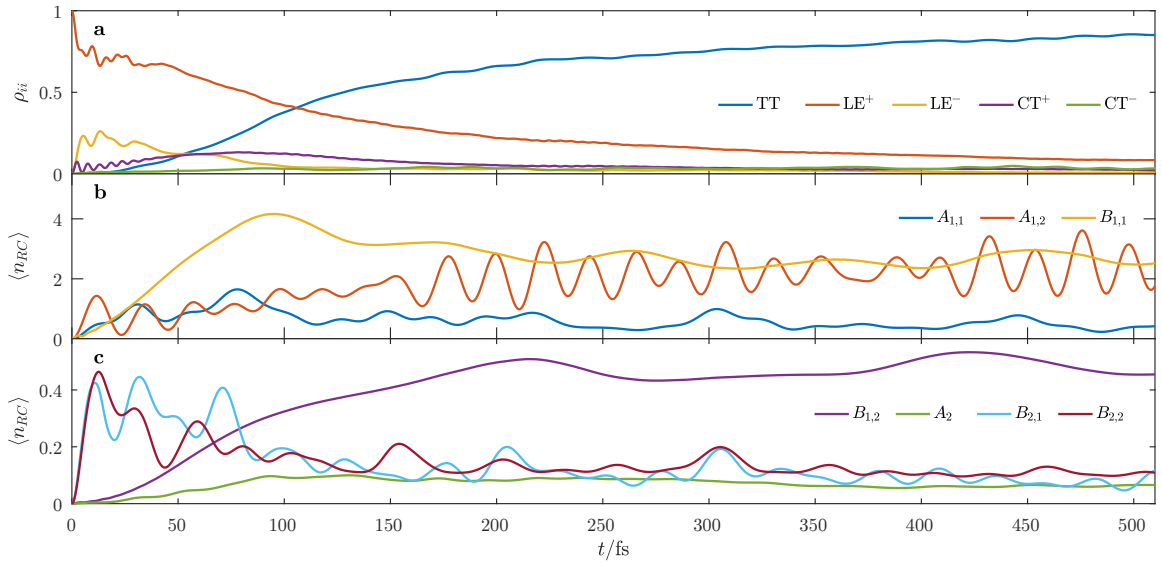

Figure 5.9: Populations (a) and environmental reaction coordinate occupation dynamics (b,c). For $< 100\,\mathrm{fs}$ SF is controlled by B_2, while B_1 defines the long-time state. Simulations show SF with almost 90% TT yield. Courtesy of F. A. Y. N. Schröder.

the core tensor representing the interaction of the electronic system with the chains would still contain seven independent bond indices, leading to a very large number of components. To address this problem, the core tensor is further decomposed into a tree of auxiliary entanglement renormalisation (ER) tensors [146, 147]. This tree network allows an efficient description of the entanglement between the electronic states and the harmonic chains.

The TTNS is time-evolved by employing the time-dependent variational principle (TDVP) [141, 148]. The simulations are performed at zero temperature (i.e. no initial environmental excitations), and start from the optically bright state LE^+.

5.5 Results

5.5.1 Fission dynamics

The central results of simulating the electronic-vibrational dynamics of DP-Mes after photoexcitation to LE^+ are shown in Fig. 5.9. Panel (a) presents the population dynamics of the electronic states, panels (b, c) show the occupation expectation of the vibrational reaction coordinates broken down by chains/symmetries. Singlet fission mediated by vibrations occurs on a 200 fs timescale, with a final TT yield of about 90%. There is a certain amount of scale-separation in the dynamics obtained from the simulation. Early on, in the course of the first $\sim$50 fs we observe ultrafast, damped Rabi-like oscillations between states

LE^+, CT^+ (mediated by B_1 modes) and states LE^+, LE^- (mediated by B_2 modes). This is associated with noticeable transfer of populations from LE^+ to LE^-, and rapid excitation of the B_2 modes which couple these states (Fig 5.7). The excitation of these modes occurs spontaneously, breaking the initial symmetry in the process. Subsequently, at times >50 fs we observe a rapid rise of the TT population, mirrored by the decay of LE^+ population. On the vibrational side this conversion is associated with a strong build-up of B_1 occupation. The B_1 modes couple LE^- to TT via CT^- (see Fig. 5.7), opening a vibronic super-exchange pathway for fission. The rapid modulation seen in the TT population corresponds to the fast oscillatory activity observed in the $A_{1,2}$ tuning modes.

5.5.2 Dynamic energy surfaces

Additional insights into the fission mechanism can be gained by considering the time-evolution of energy surfaces, specifically the adiabatic potential energy surfaces (PES) and the total energy surfaces (TES). They are defined as the time-dependent eigenvalues of the effective potential energy and effective Hamiltonian of the electronic system, respectively. The time-evolution of these surfaces is shown in Fig. 5.10. Initially, at around 20 fs the TES of the TT state is initially pushed above LE^+. This rise co-occurs with the rapid displacement of the B_2 reaction coordinate. Subsequently, the TT surface slowly drops in energy, eventually crossing the LE^+ surface. However, in the PES no significant crossing is apparent which suggests that conical intersection dynamics is not relevant for the fission process. Rather, we observe an avoided crossing in both the PES and TES at about 80 fs with respective gaps of 220 meV and 10 meV. This corresponds to an effective LE^+ to TT coupling of 110 meV which results from the excitation of both B_1 and B_2 modes. The avoided crossing allows resonant population conversion from LE^+ to TT and occurs sufficiently slowly for the bulk of the LE^+ population to convert to TT. A crucial enabler of this resonant transfer is the existence of the B_1 super-exchange pathway $LE^- \rightarrow CT^- \rightarrow TT$, allowing coupling through CT^- as a virtual state. Coupling is thus enabled without incurring the significant energy penalty that would otherwise be required to occupy the state. While the TES make the resonant nature of the process apparent, the PES demonstrate that fission dynamics is continuously downhill. This suggests that fission should be reasonable robust against perturbations, such as a change of solvent environment.

5.6 Conclusions

In this chapter we developed a dynamical model of the singlet fission process in a covalent pentacene dimer, DP-Mes. This was achieved by means of an approximate DFT parametrisa-

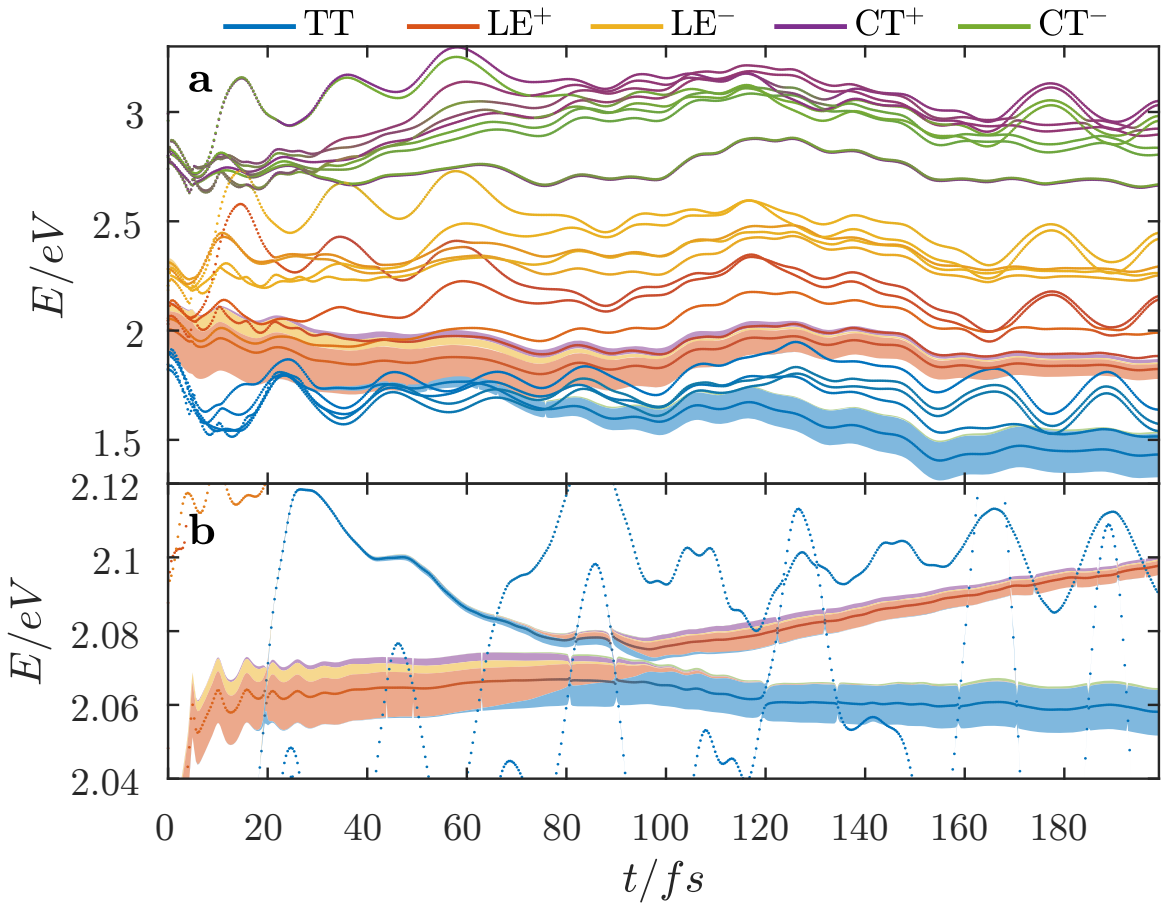

Figure 5.10: Energy surfaces and their diabatic populations. The filled areas indicate the amount of diabatic population on each surface. The surfaces (dots) are coloured according to their mixing of electronic states. (a) The dynamics are not caused by conical intersections in the adiabatic potential energy surfaces. (b) Instead the vibronic mixing and super-exchange is sufficient to produce an avoided crossing of LE^+ and TT in the total energy surfaces, causing rapid fission. Courtesy of F. A. Y. N. Schröder.

tion of the vibronic coupling Hamiltonian, forming the basis for tree tensor network quantum dynamics calculations. Both the parametrisation and the dynamics simulations take advantage of the high symmetry of the DP-Mes molecule. Even though this symmetry precludes direct electronic couplings between the relevant electronic states, the simulations show that fission can still be achieved through symmetry-breaking vibrational coupling. In particular, it is demonstrated that SF in DP-Mes is facilitated by the activity of modes of B_1 and B_2 representations which spontaneously break the initial symmetry. Furthermore, it is shown that fission proceeds via an avoided crossing (rather than a conical intersection) and takes advantage of a super-exchange pathway mediated by high-lying states of charge-transfer character.

Chapter 6

Solvent effects on electronic excitations in dimer pentacene

Following the investigation of fission dynamics in DP-Mes in the previous chapter, we now turn to the questions of how the solvent environment affects the electronic structure and thereby fission in dimer pentacene. Previously, we had completely disregarded this aspect for the sake of simplicity, by performing the DFT calculations in vacuum. In addition to the effect of solvents, we also explore the influence of the choice of side-groups of the pentacene dimers. This is accomplished by contrasting the behaviour of DP-Mes with another dimer, DP-TIPS. DP-TIPS has the same basic structure, with a pair of centrally linked pentacene molecules forming an orthogonal configuration. However, it differs from DP-Mes in terms of its side-groups, which contain silicon and are linked to the pentacene molecules via C≡C triple bonds (see Fig. 6.1).

First, we review experimental investigations of fission in DP-Mes and DP-TIPS conducted by Lukman et al., for which we provided support from the theory side [88,89]. These include measurements of fission rates and yields, as well as transient absorption (TA) spectroscopy, in a range of solvent environments. TA allows us to probe the dynamics of the absorption spectrum of a sample, giving time-resolved access to the populations of different electronic states implicated in the fission process. Based on the experimental results, a model is proposed to explain differences in the observed behaviour of DP-Mes and DP-TIPS. In accordance with the results of the previous chapter, a virtual CT intermediate is conjectured in the case of DP-Mes, whereas the measurements indicate a 'real' CT intermediate for DP-TIPS (i.e. the CT state is substantially populated). In addition to fast fission dynamics, the experiments reveal interesting long-time behaviour. This includes triplet-triplet annihilation (the inverse process of fission), as well as substantial solvent stabilisation of residual LE and CT states in polar solvents. The latter is possibly associated with significant geometric

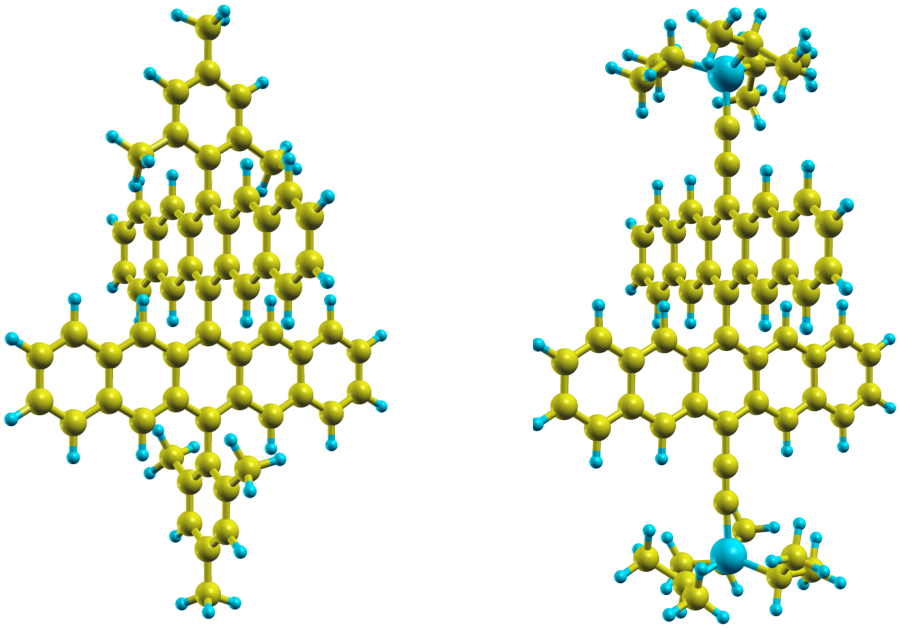

Figure 6.1: DP-Mes (left) and the second dimer DP-TIPS (right), where the mesityl side groups are replaced by triisopropylsilylethynyl. The TIPS side groups contain silicon atoms and link to the pentacene molecules via C≡C triple bonds.

change in the pentacene dimers.

Following the discussion of experimental results, we turn to the question of to what extent electronic structure theory can elucidate the observed differences between the dimers, and the influence of the solvent environment on the electronic states and fission. To this end, we perform a range of DFT calculations of the significant electronic states, using TDDFT, cDFT and global spin constraints. Solvent effects are accounted for both with implicit continuum solvation models as well as explicit solvent. For the explicit solvent calculations we employ a hybrid approach of molecular dynamics (MD) and DFT. Computationally inexpensive empirical-potential MD is used to generate realistic solvent-solute configurations in thermal equilibrium. Subsequently, we take the configurations thus generated as input geometries for DFT and TDDFT. In this way we can obtain *ab initio* spectra of representative solvent-solute configurations without the need for full MD which would be prohibitively expensive computationally.

Finally, the theoretical results are compared to the experimental observations, from the point of view of the experimentally motivated fission model. This leads on to a discussion of the merits and limitations of the presented DFT methods in shedding light on the effects of complex environment interaction on electronic excitations.

6.1 Overview of experiments and solvent environments

The excitations and fission dynamics in DP-Mes and DP-TIPS have been investigated using optical steady-state absorption, delayed photoemission and transient absorption (TA) measurements [88, 89]. In TA the time-evolution of the absorption spectrum of a sample which has been hit by a sharp pump-pulse to create excitations can be recorded with high (sub-picosecond) time resolution [149]. Specific features in the spectrum can be matched to particular electronic states, with feature intensity being proportional to population of the respective state. This makes it possible to extract the full time-evolution of the electronic states in the sample after excitation through the initial pump-pulse.

The two pentacene dimers were measured in dilute solution of a variety of solvents, listed in Tab. 6.1. In the context of this work the salient solvent properties affecting the physics are polarity and polarisability. More precisely, polarity characterises the long-term dielectric response of a solvent. This relies on the reorientation of solvent molecules with intrinsic dipoles and is comparatively slow. A good way to quantify this is the static dielectric constant ϵ_0. Highly polar solvents with large values of ϵ_0 have large intrinsic dipole moments, as can be gleaned form the table.

Polarisability, on the other hand, describes the short-term response of a solvent on optical timescales. This property can be quantified using the refractive index, or equivalently, the infinite-frequency dielectric constant ϵ_∞. The effect relies on the polarisation of electron orbitals and is particularly pronounced in the presence of delocalised valence orbitals. This explains the relatively high polarisability of toluene and o-DCB which have delocalised pi-systems. A special case is hexane which does not have an intrinsic dipole. Here, the entire dielectric response is due to orbital polarisation, meaning that polarity and polarisability are virtually identical.

At low polarity, triplet yields in DP-Mes are close to 200%, but decline gradually decline with increasing polarity, down to about 120% in DMSO. Low-polarity yields in DP-TIPS are slightly lower, about 180%, but initially go up with increasing polarity, before ultimately declining down to roughly 160% [89].

6.2 Absorption and photoluminescence

6.2.1 Experimental details

The absorption spectra of DP-Mes and DP-TIPS are shown in Fig. 6.2 (a) and (d). Compared to the respective pentacene monomers with two side-groups, the absorption is shifted:

Solvent	ϵ_0	ϵ_∞ (n_D^2)	Dipole moment (D)
Hexane	1.88	1.89	0.00
Toluene	2.38	2.24	0.36
Chloroform	4.81	2.09	1.04
o-dichlorobenzene (o-DCB)	9.93	2.41	-
Ethanol	24.6	1.85	1.69
Acetonitrile (ACN)	37.5	1.81	3.92
Dimethylformamide (DMF)	38	2.05	3.82
Dimethyl sulfoxide (DMSO)	46.7	2.19	3.96

Table 6.1: Dielectric properties of the range of solvents used in experiments. The high-frequency dielectric constants are calculated as the squared refractive index at the sodium D line.

to the red in DP-Mes, and to the blue in DP-TIPS. This results from a competition between side-group delocalisation and Davydov splitting. In general, a redshift of the absorption with increasing polarisability is apparent in both molecules. This observation is consistent with the fact that absorption probes the dielectric response of the sample on optical timescales.

Significant differences between DP-Mes and DP-TIPS emerge in the delayed photoemission or photoluminescence (PL). The relevant spectra are displayed in Fig. 6.2 (b) and (e). Since the PL response occurs over a longer (nanosecond) timescale, the observed redshifts are sensitive to solvent polarity rather than polarisability.

In the case of DP-Mes, the entire spectrum redshifts uniformly, with the shape staying largely invariant. In addition, the PL decays uniformly (c) which indicates the presence of just a single long-lived species for each solvent. However, there is a separation of decay timescales in that the rate of decay in hexane is significantly faster than in DMSO. This hints at the fact that the emissive species in hexane is distinct from the emissive species in DMSO, as is corroborated by the TA data discussed below.

The PL response of DP-TIPS, on the other hand, shows a loss of structure and very strong redshifts at high polarity values. The PL decay reveals two species with different lifetimes at low polarity, and a single species at higher polarities. A spectral decomposition of the PL decay shows that the first component is only weakly affected by solvent polarity. The second component is spectrally broad, with a slightly shorter lifetime and redshift strongly with increasing polarity. These properties are indicative of states with charge-transfer character [150].

The results show that the populations of electronic states in both pentacene dimers strongly depend on solvent polarity. Furthermore, the side-groups which distinguish the two dimers also have a significant effect on the excitations.

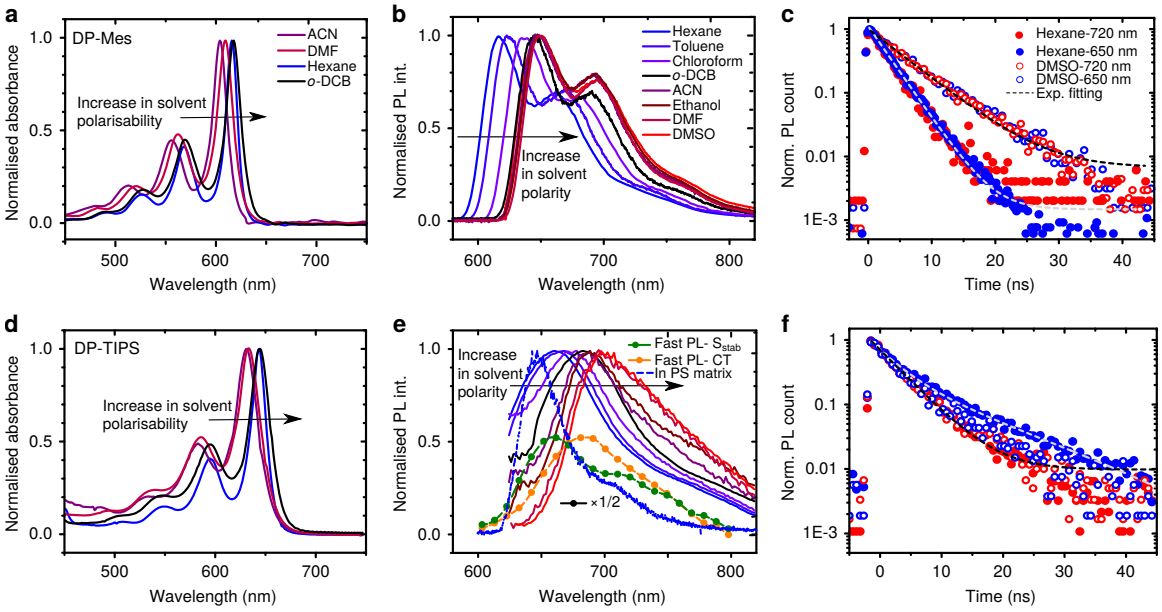

Figure 6.2: Solvent dependence of absorption and emission. Absorption spectra of DP-Mes (a) and DP-TIPS (d) exhibit redshifts with increasing solvent polarisability. The photoluminescence (PL) spectra of DP-Mes (b) and DP-TIPS (e) show strong redshifts with increasing solvent polarity. (c) The decay of the PL spectra of DP-Mes is uniform across the spectral range for both polar and non-polar solvents. (f) In DP-TIPS the decay kinetics vary across the spectrum in the case of hexane (filled circles). This indicates the presence of several, distinct emissive states. Reproduced from Ref. [89].

6.2.2 Electronic structure calculations

Attempting to model the absorption of pentacene dimers constitutes a valuable test-bed for large-scale TDDFT with explicit solvent. It can be seen as a first step towards modelling the full range of interactions between solvent and the electronic structure of the solute. Techniques similar to the ones we will lay out have been applied to *ab initio* predictions of the colour of dyes in different solvent environments [151, 152].

Obtaining realistic spectra at finite temperature is made challenging by the requirement to sufficiently sample the space of geometrical configurations of the solvent-solute system. This is because excitation energies are strongly affected by geometry, especially in the case of the low-lying excitations of the relatively large and flexible pentacene dimers we are interested in. A full ab-initio MD simulation of solvent and solute would be computationally prohibitive. Hence, we opt for a hybrid approach, namely using empirical potential MD to generate solvent-solute configurations in thermal equilibrium, which form the basis for subsequent TDDFT calculations.

For the purpose of this analysis we focus on two solvents, toluene and acetonitrile (ACN). The molecular structures are show in Fig. 6.3. This selection is motivated by the contrasting properties of these two molecules, cf. Tab. 6.1. Toluene, on the one hand, only has a small intrinsic dipole, but a delocalised π-system in the from of the benzene ring. As a consequence, toluene is easy to polarise, manifesting itself in a relatively high ϵ_∞ of 2.24. The static dielectric constant ϵ_0 is only marginally higher (2.38) due to the lack of a large intrinsic dipole. ACN, on the other hand, has low polarisability as a result of its small size with no delocalised electron system. However, a large intrinsic dipole is set up by the differing electron affinities of nitrogen and carbon. This leads to low polarisability (ϵ_∞ of 1.81), but high polarity with a static permittivity of 37.5.

Empirical MD for configuration sampling

For the MD calculations the AMBER molecular dynamics package is employed [153], using the general AMBER force field (GAFF). We embed the pentacene dimers in a truncated octahedral solvent shell with a radius of 25 Å, and impose periodic boundary conditions. This translates to about 700 molecules of toluene or about 1700 molecules of ACN, respectively. A 200 ps run in the NVT ensemble is performed to equilibrate the temperature, which is gradually raised from 0 to 300 K (using the Langevin thermostat [154]). Subsequently, the pressure is equilibrated for another 200 ps, this time in the NPT ensemble, with the pressure held constant at 1 atmosphere. After thermal equilibrium at the relevant temperature and

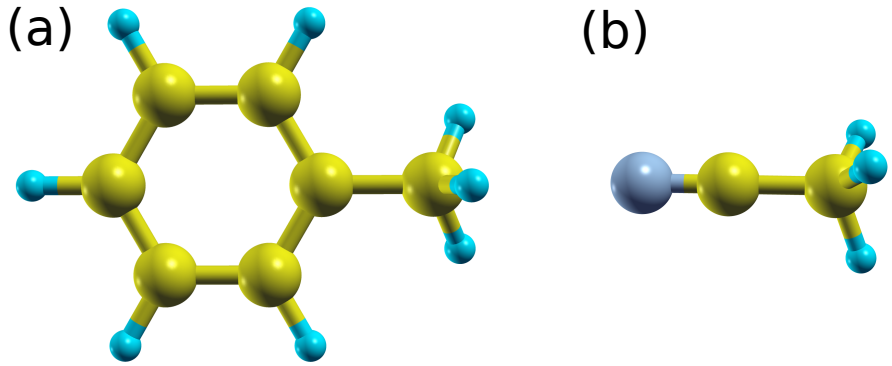

Figure 6.3: (a) Toluene and (b) acetonitrile solvents used in calculations. While toluene is highly polarisable due to delocalised electrons in the benzene ring, its permanent dipole is weak. Acetonitrile, on the other hand, has a large permanent dipole but has low polarisability.

pressure has thus been achieved, we conduct a production run lasting 1000 ps. From this run we sample a set of 100 snapshots for each of the four solute-solvent combinations, respectively.

TDDFT calculations

To prepare simulation cells for the TDDFT part of the calculation we need to reduce the size of the explicit solvent region in the interest of manageable computational cost. This is achieved by carving out a sphere around the centre of mass of the pentacene dimers, only retaining solvent molecules that completely fall within a radius of 15 Å. This results in simulation cells with 600–800 atoms and ensures that the solute molecule is completely covered by explicit solvent on all sides, cf. Fig. 6.4. The explicit region is then surrounded by implicit solvent with a dielectric constant corresponding to ϵ_0 of the respective solvent. This ensures that any random net dipole of the explicit solvent region is screened and avoids a potential closure of the band gap as a results of such dipole fields [133]. It should be noted that in this setup the solvent geometry is strictly frozen, and the entire response of the solute-solvent system is due to the electrons, i.e. polarisability (ϵ_∞). However, this is sufficient to model absorption taking place on optical timescales during which the geometry does not change significantly.

For the TDDFT calculations, we employ the PBE functional and norm-conserving pseudopotentials. Further, we choose an energy cutoff of 750 eV and an NGWF localisation radius of $10\,a_0$. These values have been shown to yield reliable results for low-energy exci-

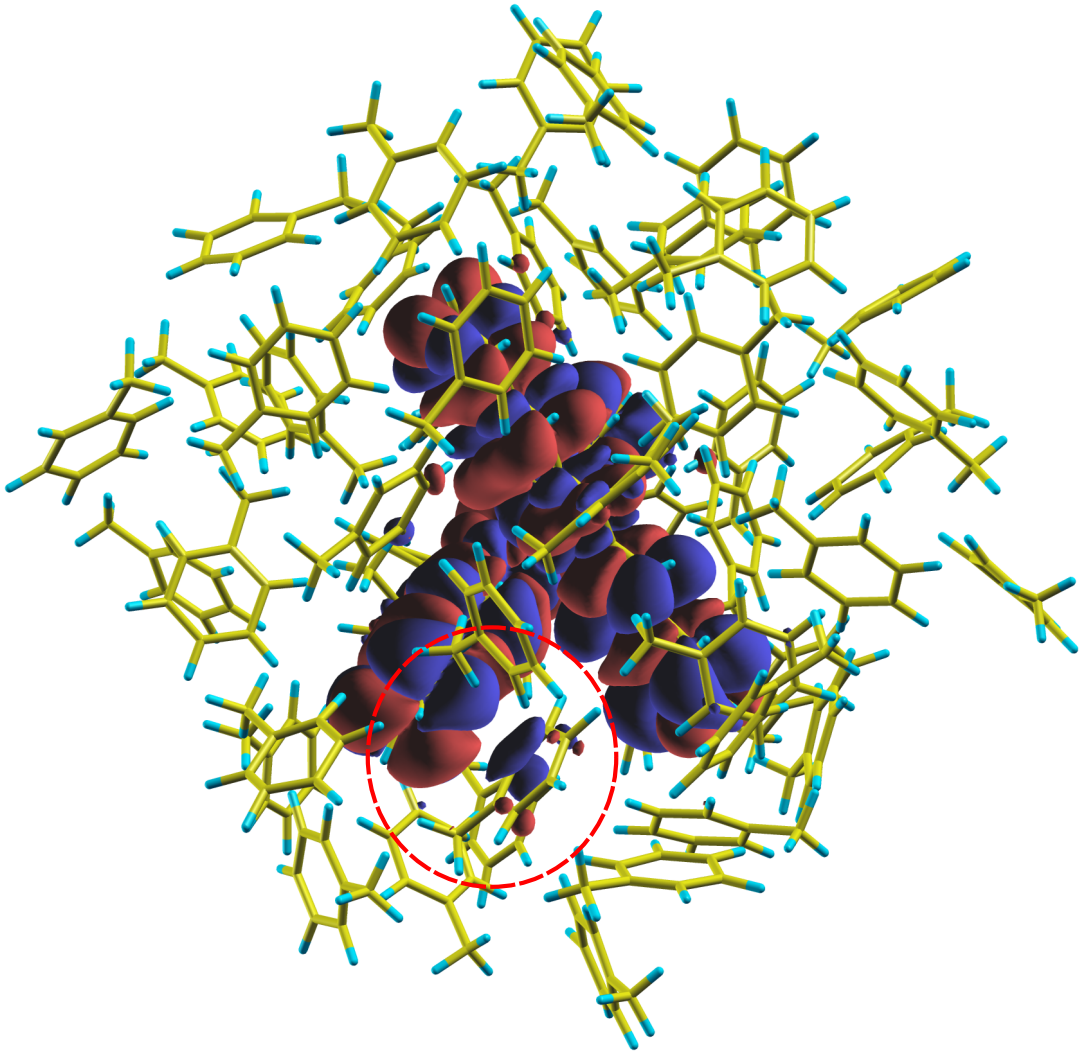

Figure 6.4: DP-Mes in toluene solvent sphere (radius 15 Å) with isosurfaces indicating electron-hole density of the excited state. π-π interactions between solute and solvent manifest as a delocalisation of the excitation onto solvent molecules.

tations of organic molecules [155]. We then converge the four lowest excited singlet states for each snapshot. These states comprise two of Frenkel type and two of charge-transfer type. TDDFT with (semi-)local functionals such as PBE is known to severely underestimate the energies of CT-like states. However, this is not a concern for the prediction of the optical absorption spectrum since CT states carry negligible oscillator strength. The two states of Frenkel type correspond to the bright and dark local singlet excitations of the dimers discussed in the previous chapter. However, due to disorder these states tend to mix significantly, with the bright state often lending significant oscillator strength to the dark state.

In toluene solvent we find that the solvent molecules, specifically their π-systems, can participate in the excitation of the pentacene dimer to a certain extent. This is evidenced by the fact that the electron-hole density of the excitation can delocalise onto close-by toluene molecules. An example of this can be seen in Fig. 6.4.

Convergence of spectra

To obtain absorption spectra from the TDDFT runs, all we have to do in principle is to construct a convolution of the excitation energies of the snapshots with a suitable smearing function, weighted by the oscillator strength of each excitation [156]. However, since we are only able to calculate excitation energies for a finite sample of configurations, it is important to evaluate the degree of convergence of the spectra. In particular, we need to ensure sufficient convergence to resolve the shifts of the spectral maxima which are only a few 10 meV between the chosen solvents. In order to achieve this, we sample 100 configurations for each of the four solvent-solute combinations, which is at the upper end of feasibility in terms of available computational resources.

A semi-quantitative estimate of the convergence can be obtained from Fig. 6.5b, for the example of DP-Mes in ACN. Here, we subdivide the 100 snapshots into equal portions of various sizes, and plot families of averaged spectra for each sample size. The degree of variation between these families then gives an indication of the convergence that has been achieved for a particular sample size. In the figure and all of the following analysis we use a Gaussian smearing function of width 0.03 eV. This choice ensures sufficiently low variability of the spectral shape when averaged over all 100 samples, without completely washing out the shape information, cf. Fig. 6.5a.

In order to estimate the error in the spectral maximum for all 100 samples we would like to avoid having to draw multiple such samples for reasons of computational feasibility. Rather, we extrapolate the variance seen in the families of spectra with smaller sample size to the

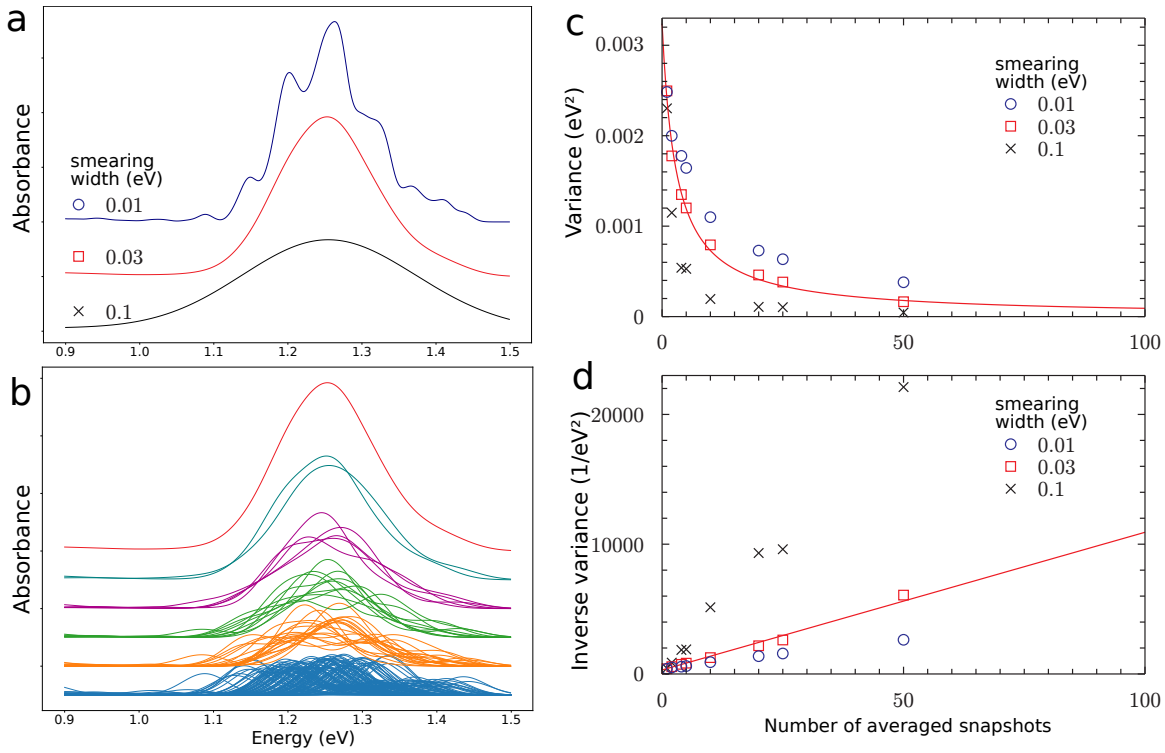

Figure 6.5: (a) Spectral shape of calculated absorption spectrum of DP-Mes in ACN for three different smearing widths. (b) Convergence of the spectrum with respect to number of snapshots (for smearing width 0.03 eV). The families of spectra are averaged over 1, 5, 10, 20, 50 and all 100 snapshots, respectively. (c, d) Variances in the spectral maximum in dependence of the number of averaged snapshots, for the same three different values of the smearing width. The variance is extrapolated to 100 snapshots using a linear fit to the inverse variance.

full set. To this end, we plot the variance and inverse variance of the spectral maxima in dependence of the sample size (Fig. 6.5c, d), and for three different smearing widths.

In the limit of large smearing widths, calculating the maximum of the averaged spectra becomes equivalent to simply calculating the oscillator-strength-weighted average of the individual energies. This is because in the vicinity of the maximum, Gaussians are approximately quadratic. Hence, the spectral maximum becomes the point with minimum squared deviation from the data points, i.e. their (weighted) mean. In line with the known basic properties of the variance of the mean, it is then expected that the variance of the maximum behaves like $1/N$ if N is the number of snapshots. Hence, the inverse variance is expected to be proportional to the number of snapshots.

In the limit of very small smearing width, on the other hand, spectral averaging would not be expected to reduce the variance of the maximum significantly, since there would be only small overlap between the supports of spectra corresponding to different snapshots.

This behaviour is also apparent in Fig. 6.5c, where the variance of the maximum decays more quickly for large smearing width, and more slowly for a smaller value of the smearing width. Looking at the inverse variance (d) for our chosen smearing of 0.03 eV, we see that it grows less quickly than what would be expected from proportionality to N. However, the trend is still well-described by a linear function if we relax the constraint that it should intercept the origin. The plot of the variance (c) confirms that this constitutes a good fit also for small numbers of snapshots. Extrapolating, the inverse of the variance of the spectral maximum for all 100 snapshots is about $10^4\,\mathrm{eV}^{-2}$. This translates to a standard deviation of about 0.01 eV, with very similar numbers applying to all four solute-solvent combinations.

6.2.3 Results

The normalised absorption spectra for DP-Mes and DP-TIPS in toluene and ACN solvents are shown in Fig. 6.6. It is apparent that the calculated spectra are strongly redshifted compared to the experimental spectra, which have maxima in the vicinity of 2 eV. This is caused by two systematic errors in the calculations. Firstly, semi-local functionals are known to significantly underestimate the TDDFT energies of low-lying excitations in polyacenes such as pentacene [157]. This is reflected by the fact that the calculated vacuum energy of S_1 in DP-Mes is only 1.56 eV. Secondly, errors in the empirical potentials mean that MD geometries exhibit systematic deviations from the ones that would be sampled by *ab initio* MD. These deviations have a tendency to close the band-gap, lowering excitation energies further. If the vacuum S_1 energy in DP-Mes is evaluated at the fully relaxed geometry of the empirical potential, a value of only 1.28 eV is obtained. As a result, absolute

excitation energies obtained by this method cannot be considered meaningful without further correction.

Turning our attention to the relative shifts, we observe that DP-TIPS energies are redshifted relative to DP-Mes, by about 0.07 eV which compares favourably to the experimental value of roughly 0.1 eV. This difference between the dimers can be explained by looking at the transition densities associated with S_1 as plotted in Fig. 6.7. It is apparent that in the case of DP-TIPS there is stronger delocalisation of the excitation onto the side group, specifically the region around the linking carbon atom and the C≡C triple bond. This can be expected to lead to lower excitation energies in DP-TIPS relative to DP-Mes.

Comparing the two solvents, theory predicts respective redshifts of 0.008 eV and 0.014 eV for DP-Mes and DP-TIPS going from ACN to toluene. This qualitatively matches the observations in terms of direction of shifts, but does not reproduce the values derived from experiment with any precision (0.05 eV and 0.04 eV, respectively). However, given the multiple uncertainties due to the electronic structure methods and the sampling, as well as the small absolute magnitude of the shifts in question, this can still be considered a success. It should also be noted that we use a simple Gaussian smearing function for the convolution, whereas in reality the natural line shape is determined by Franck-Condon effects. Recent work has shown that improved spectra are obtained if this is accounted for [156].

6.3 SF kinetics and solvent dependence

In the following section we discuss the TA results which provide much more detailed insights into the nature and dynamics of the electronic states involved in fission.

6.3.1 Experimental details

DP-Mes

The kinetics of SF in DP-Mes is shown in Fig. 6.8 (a) and (b) for the hexane and DMSO solvents [89]. The populations are derived from the transient absorption data which can be disentangled using an evolutionary algorithm [88], identifying three distinct species: the initial singlet excitation S_1, the triplet pair TT, and an emissive species S^* which is created from triplets through triplet-triplet annihilation (TTA).

The population dynamics show that fission in DP-Mes proceeds as a one-step process, directly from S_1 to TT, without any detectable intermediate. The fission rate is solvent dependent and increases with polarity. This hints at a role of CT states as facilitators of

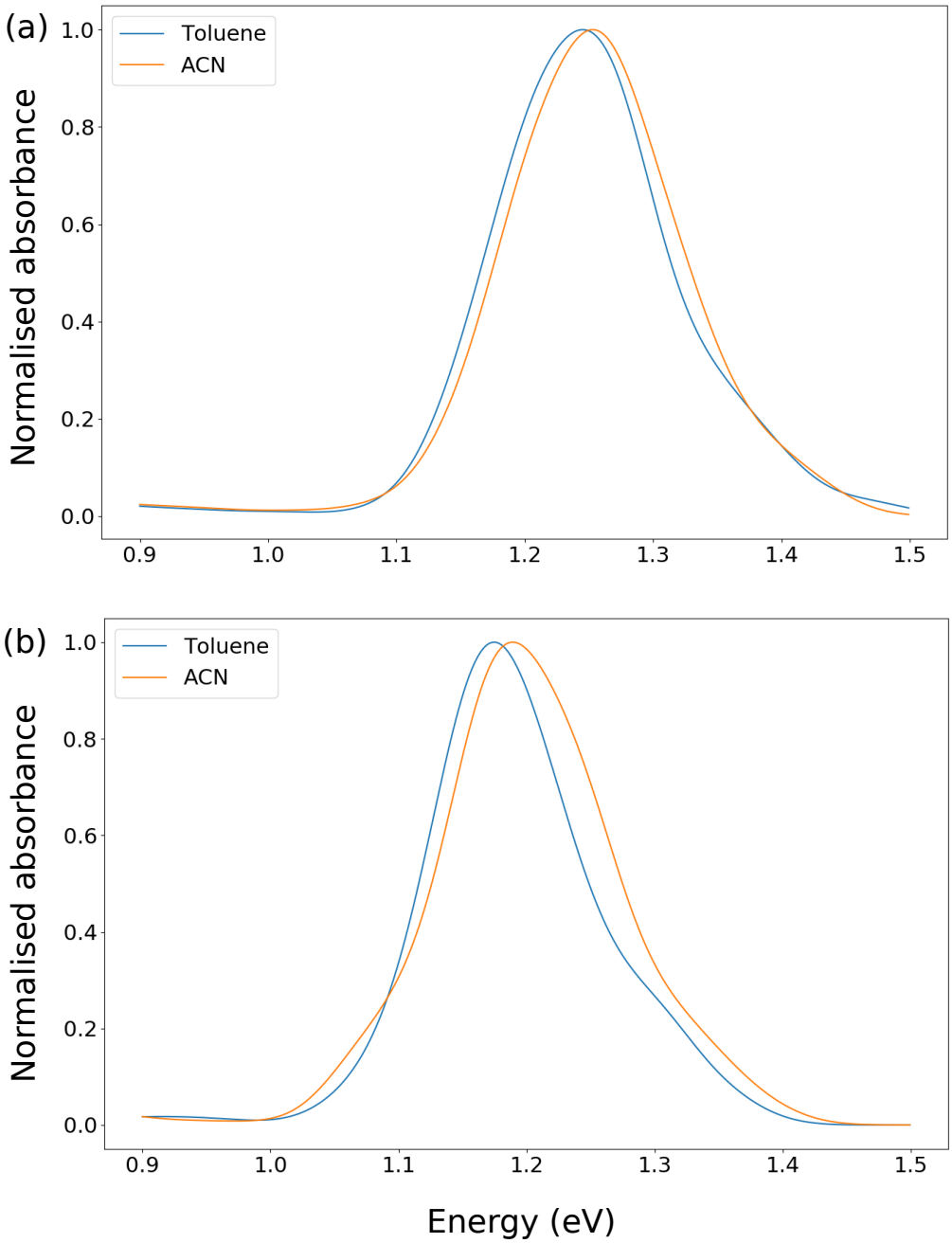

Figure 6.6: Calculated absorption spectra of (a) DP-Mes and (b) DP-TIPS. Each spectrum is averaged over 100 MD snapshots.

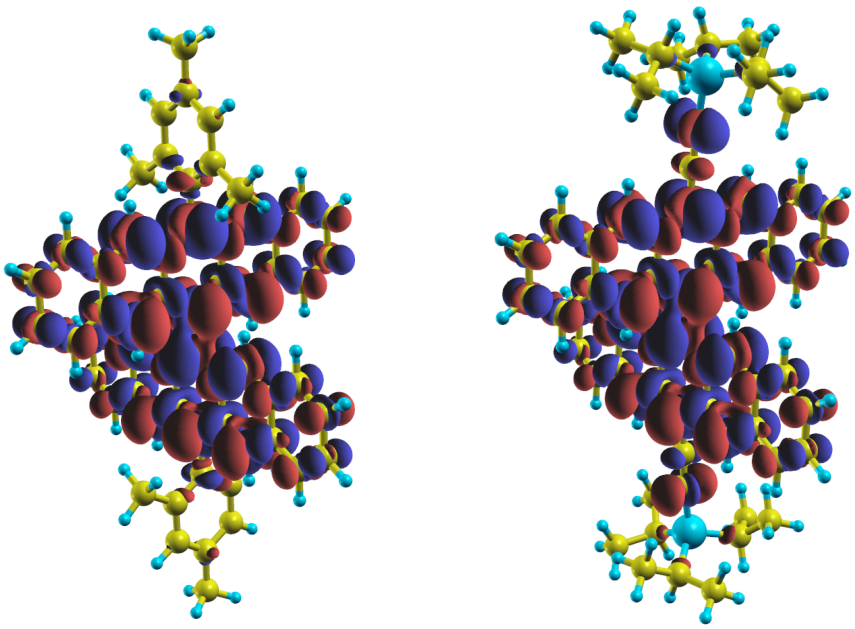

Figure 6.7: Transition densities of S_1 for DP-Mes and DP-TIPS. The C≡C triple bonds of the TIPS groups participate significantly in the excitation. This lowers the S_1 energy in DP-TIPS compared to DP-Mes where the side-groups participate only weakly.

the electronic coupling which are, however, not directly observed (cf. the model discussed in the previous chapter). The spectral features associated with the initial singlet suggest that it has some admixing of CT character.

In non-polar solvents like hexane, fission is followed by TTA, which then converts the triplets into an emissive species denoted S^*. There are a few lines of evidence that suggest that S^* is a geometrically relaxed version of S_1. The spectral features associated with S^* are redshifted and broadened compared to S_1, and its formation is impeded by geometrical restriction of DP-Mes with a rigid polystyrene matrix [88]. This provides evidence that the formation of S^* requires significant geometrical change, possibly from the orthogonal configuration to a more planar configuration with a lower dihedral angle between the pentacene units.

At higher polarities the fission rate increases (c), but the triplet yield declines. This is due to solvent stabilisation of singlets which are subsequently unable to undergo fission for energetic reasons. Fig. 6.8 (b) illustrates this phenomenon for DMSO where about half the singlets do not convert to TT, but rather experience solvent relaxation and settle into the species denoted S_{stab}.

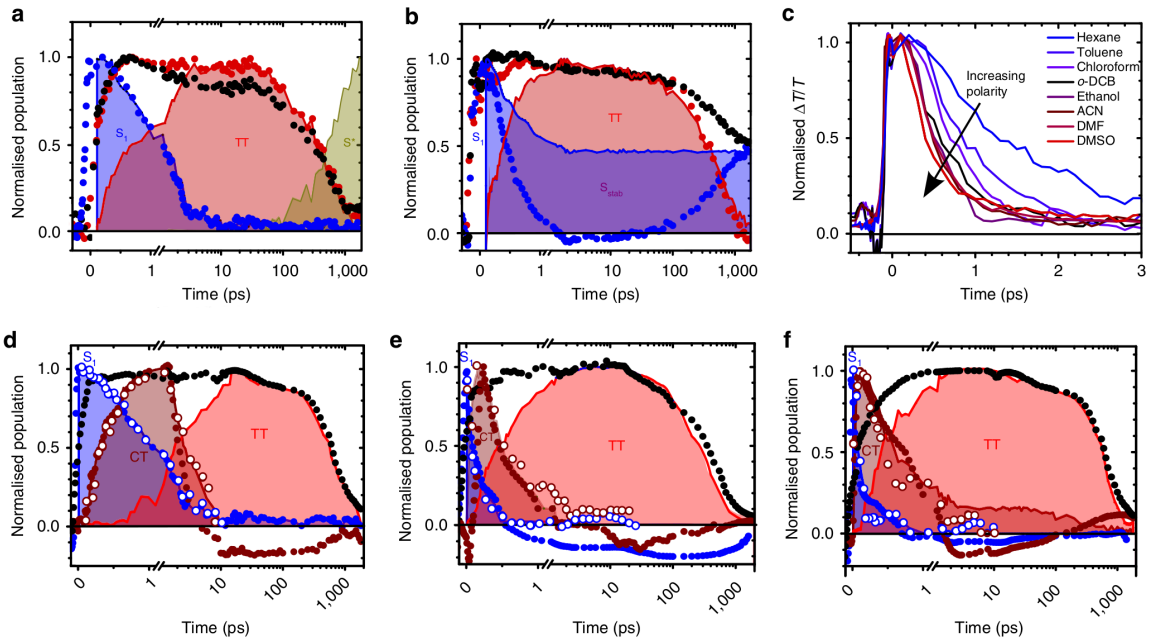

Figure 6.8: Species kinetics for DP-Mes in (a) hexane and (b) DMSO as derived from transient absorption (TA) measurements. Filled regions indicate the normalised population of electronic states, circles denote the intensity of the raw TA features averaged across three spectral regions. In hexane the entire singlet population converts into triplets which later decay yielding an emissive state S*. In DMSO, on the other hand, about half the singlet population fails to convert, and settles into a stabilised state S_{stab}. (c) The lifetime of S_1 exhibits a strong dependence on solvent polarity. DP-TIPS kinetics in (d) hexane, (e) o-DCB and (f) DMF show explicit intermediate CT state. Hexane exhibits a residual singlet population, whereas residual CT states are present in highly-polar DMF. Adapted from Ref. [89]

DP-TIPS

As in DP-Mes, fast triplet formation can also be observed in DP-TIPS, as shown in Fig. 6.8 (d-f). However, in contrast to DP-Mes, there are additional spectral features present between singlet decay and emergence of TT. The kinetics of these features match the kinetics of the PL that corresponds to CT-like emission, motivating the labelling of the intermediate as a CT state. Furthermore, spectral decomposition reveals that the state exhibiting these features is intermediate to triplet formation. In addition, its spectrum matches that of a radical anion-cation pair. This constitutes a direct observation of a CT intermediate in singlet fission. As in DP-Mes, the decay of the singlet accelerates with increasing polarity (however it converts to CT rather than TT), and conversion to CT becomes more efficient. In hexane (d) a small fraction of the S_1 population settles into S_{stab} without undergoing fission. However, the amount of S_{stab} is reduced with increasing polarity.

The rate of CT to TT conversion also depends on the solvent; at high polarities residual CT states can be observed, like in DMF (f). Here the strong solvent relaxation makes CT an energetic trap for fission. As polarity is decreased, we obtain less CT residual. A kind of optimum is achieved in o-DCB solvent (e), where both S_1 to CT and CT to TT conversion are near 100% efficient.

If the geometrical freedom of DP-TIPS is constrained by means of a rigid polymer matrix, no CT intermediate can be detected. Fission still takes place, but via the direct pathway like in DP-Mes. This suggests that substantial geometrical relaxation plays a role in enhancing the electronic coupling between S_1 and CT and/or lowering the CT energy. Both phenomena would contribute to CT appearing as a significantly populated real intermediate in DP-TIPS as opposed to just a virtual intermediate as in DP-Mes. We will return to this point in the theoretical section.

6.3.2 Proposed model

The interpretation of the experimental findings in terms of the electronic states and transitions between them is summarised in Fig. 6.9. Due to the importance of CT states as intermediates (albeit virtual in DP-Mes) fission has a strong dependence on solvent polarity which significantly affects CT energies. For DP-TIPS in low-polarity solvent, the CT energy is presumed higher than the S_{stab} energy, leading to a slow transition of the initial singlet to CT, which also competes with relaxation into S_{stab}. As polarity increases, the CT energy comes down, enabling faster conversion to CT. However, in high-polarity solvents CT is lowered so much that it becomes an energetic trap. This causes a reduction of the fission

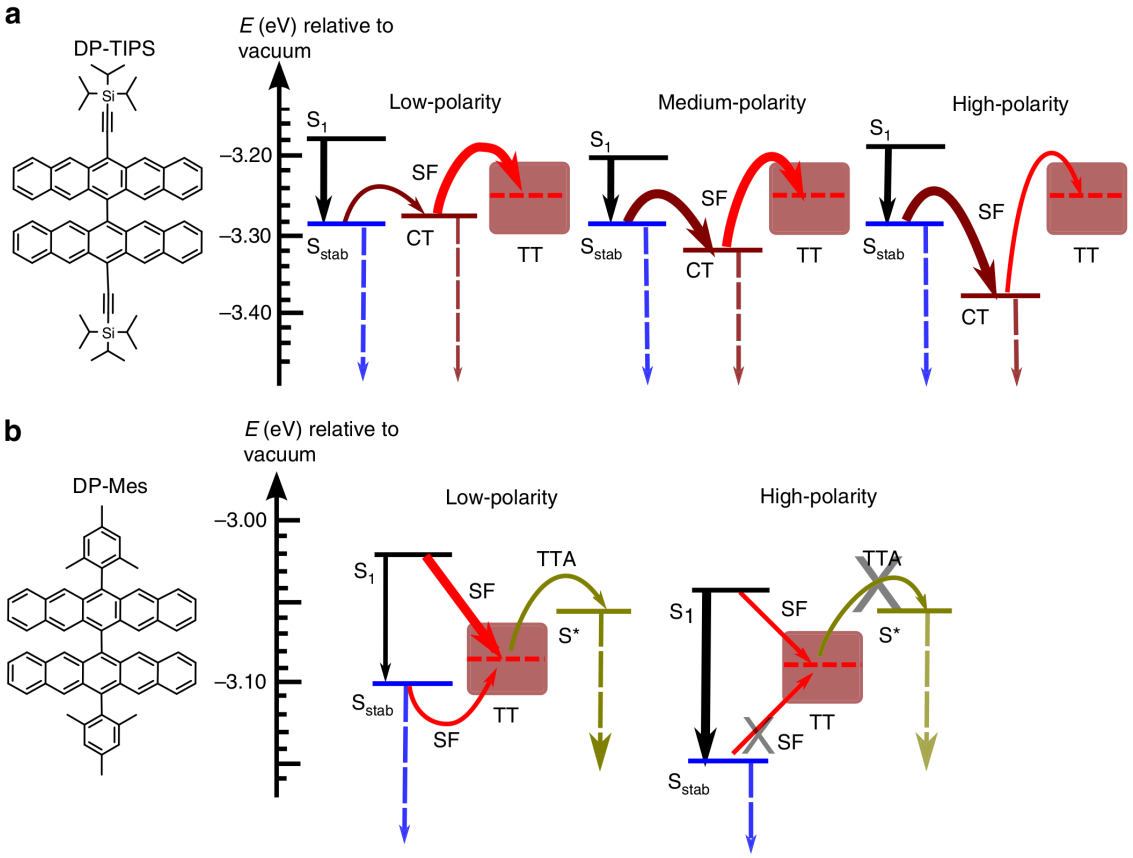

Figure 6.9: Fission model motivated by experimental data. (a) In the case of DP-TIPS, the initial singlet is stabilised by solvent and converts to intermediate CT states, which in turn transition to triplet pairs. The CT energy is strongly dependent on solvent polarity. This creates an energetic trap at high polarities, frustrating triplet formation. (b) Triplet formation is direct in DP-Mes, with no detectable CT intermediate. The process competes with solvent stabilisation of the initial singlet into S_{stab}, which is more pronounced in polar solvents. In low-polarity media ,triplet pairs convert to an emissive state S^* with altered geometry through triplet-triplet annihilation. Solid arrows denote population conversions, with thickness indicating efficiency. Dashed errors indicate radiative decay. Reproduced from Ref. [89]

yield.

The general picture is similar in DP-Mes, the main difference being that CT presumably only appears as a virtual intermediate and cannot be directly detected. At high solvent polarities, relaxation competes with fission as it does in DP-TIPS, but not through the lowering of CT but S_{stab}. The latter is more strongly affected by solvent in DP-Mes than in DP-TIPS. The results suggest that the initial S_1 state in DP-Mes already has significant admixture of CT character, whereas it is predominantly of Frenkel type in DP-TIPS, and requires geometric change in order to couple and transition to CT. In the subsequent theoretical section we explore how these differences in the observed behaviour relate to differences in the electronic structure between the two dimers. Specifically, it is of interest what effect the Mes and TIPS groups have on the relative energies of S_1 and CT states.

6.3.3 Electronic structure calculations

In an attempt to elucidate the observations about differences in fission dynamics between the two dimers, we conduct excited-state calculations with the NWChem code, using the COSMO implicit solvation model [135,158]. This makes it possible to look at all the relevant excited states and solute-solvent combinations with reasonable computational effort, even when using more accurate hybrid functionals.

First, the geometries of the dimers are relaxed at the cc-pVDZ/B3LYP level of theory. To obtain local singlet excitations, we use TDDFT at the cc-pVDZ/LC-BLYP level. Range separation is necessary here since it has been shown standard hybrid functionals without asymptotically correct exchange perform poorly for low-lying TDDFT excitations in polyacenes [136]. However, it should be noted that there is no guarantee that the improvements seen for individual oligoacenes also carry over to dimers. In both dimers the lowest singlet excitation from TDDFT is bright and corresponds to the optically excited S_1 state. For the CT state we use cDFT at the cc-pVDZ/B3LYP level. The constraint used is a net charge and spin of one electron on one half of the molecule, and one fewer on the other half. The additional spin constraint is needed to ensure the correct limit of the energy for large electron-hole separations [159]. For the TT state two proxies are considered: the quintet with an overall net-spin of 4 electron units, and a constrained configuration with a net up-spin of 2 units on one half of the molecules, and a net down-spin of 2 units on the other half. Both approaches yield energies within 10 meV of each other, which is encouraging. Still, it should be noted that neither of these proxies captures the multi-reference spin configuration of the TT state correctly.

The COSMO solvation model fills the space outside the molecule (as defined by the Van der

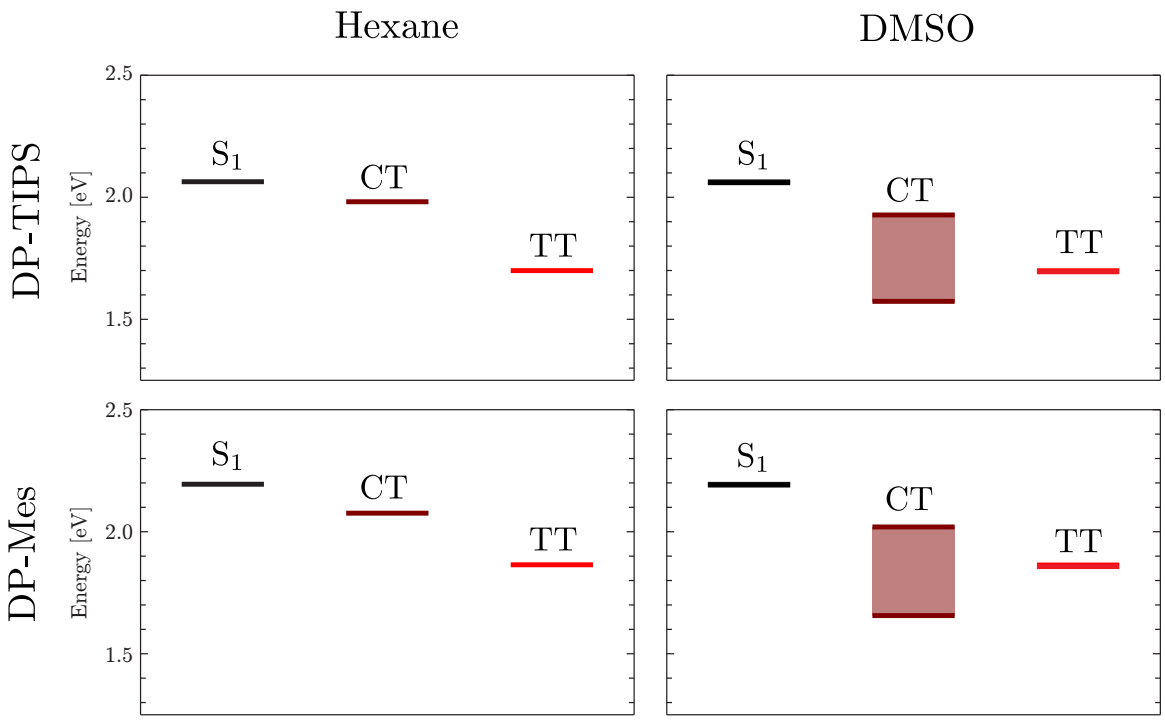

Figure 6.10: Equivalent of Fig. 6.9 with theoretical values for excitation energies calculated with implicit solvent. The chosen solvents hexane and DMSO represent the low and high ends of the polarity scale (cf. Tab. 6.1). The band of CT energies in DMSO reflects the range of relaxation through slow reorientation of solvent molecules.

Waals radii of the atoms) with a uniform, isotropic dielectric of a given permittivity [158]. We choose to consider the two solvents at opposite ends of the polarity scale, namely hexane and DMSO (see Tab. 6.1). In the case of a non-polar solvent like hexane, short-term and long-term responses are effectively identical and can be described by a single value of the permittivity. For a highly-polar solvent like DMSO, on the other hand, ϵ_∞ and ϵ_0 differ very significantly. On very short timescales an excited state will experience only ϵ_0, with a gradual transition to ϵ_0 as the solvent molecules reorient over time. In DMSO this timescale is on the order of 10 ps [160], comparable to the timescale of fission. This process of solvent relaxation is particularly significant for the CT states with their large dipole moments.

6.3.4 Discussion

Fig. 6.10 is the equivalent of Fig. 6.9 with theoretical numbers. The solvents hexane and DMSO correspond to the low- and high-polarity scenarios in Fig. 6.9. The overall alignment of the energy levels broadly agrees with the experimental picture. However, it is notable that the calculated energy of TT is significantly lower than S_1. The calculated TT energy

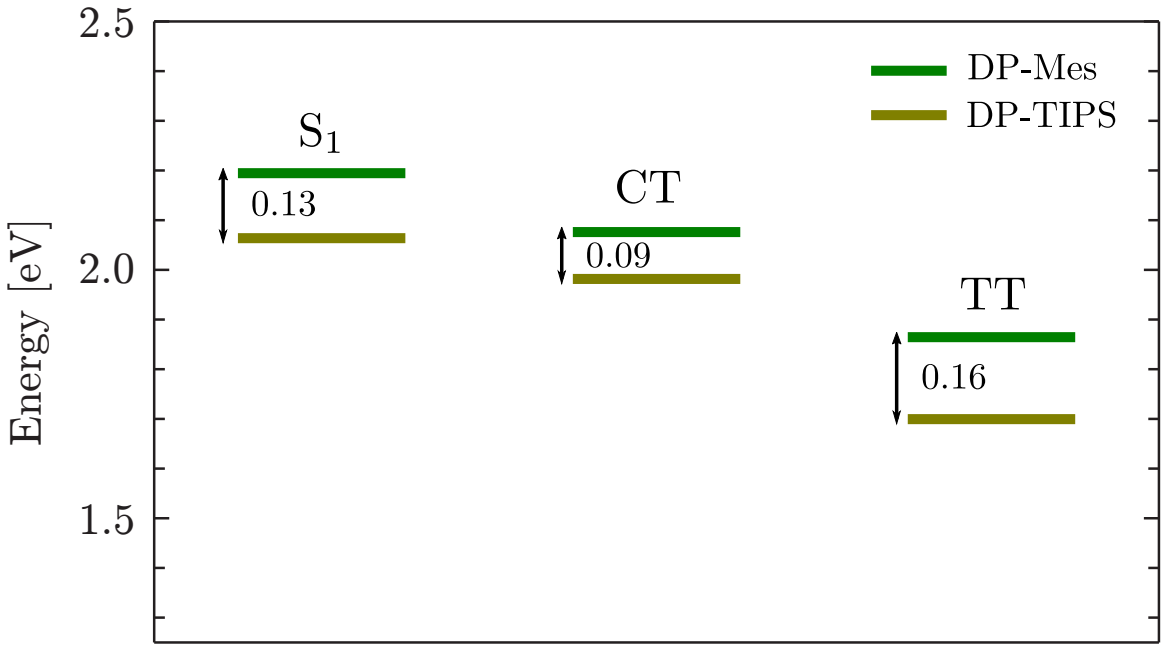

Figure 6.11: Comparison of calculated excitations energies for DP-Mes and DP-TIPS in implicit hexane solvent. Relative shifts are indicated. The differential shifts can be explained as a result of the differing degrees of side-group delocalisation.

is very close to twice the energy of a single triplet confined to one of the pentacene units, as expected. The slight tension with experiment may indicate inaccuracy in the DFT estimate of the strength of the exchange interaction, which determines the singlet-triplet gap.

Even so the calculations agree well with the idea that in highly polar environments the CT states can fall significantly below TT, thereby creating an energetic trap for fission. According to the model, this effect is directly observable in DP-TIPS. In DP-Mes, on the other hand, CT is thought to be admixed into S_1, causing strong relaxation into S_{stab} in polar environments. However, it is not entirely clear how the calculation results mesh with this supposed difference between DP-Mes and DP-TIPS. The theoretical picture looks very similar for both molecules, except for an overall redshift in the case of DP-TIPS.

To elucidate what is going on we directly compare DP-Mes and DP-TIPS energies in the case of hexane, as shown in Fig. 6.11. This perspective does indeed reveal differential shifts which could help explain the observed differences between the two dimers. The dominant feature is a redshift of the DP-TIPS energies, of 130 meV for S_1. As previously stated, this is a result of stronger side-group delocalisation of the frontier orbitals in DP-TIPS, slightly closing the band gap. Interestingly, this shift is reduced for the CT states, down to 90 meV. A natural explanation is that the same delocalisation effect causes a slight increase of the electron-hole separation in DP-TIPS, making the CT energy a bit higher than what would

be expected purely from the change in the band gap. For TT, on the other hand, the shift actually increases to 160 meV. This appears to be a straightforward consequence of the band gap reduction in DP-TIPS. The effect is stronger compared to S_1 since TT is a doubly-excited state.

We return to the question of to what extent theory backs up the experimentally motivated model. Taken at face value, the computed numbers do not agree with the notion that S_1 and CT energies are relatively closer in DP-Mes to explain strong CT mixing into the optically excited initial state in DP-Mes, but not in DP-TIPS. However, it should be kept in mind that the calculated S_1-CT difference is susceptible to systematic uncertainties, especially given the different methodologies used to obtain the energies (TDDFT vs cDFT). Within these uncertainties, it is certainly possible that S_1 and CT are in fact very close in DP-Mes. If that were the case, the differential shifts could then account for a larger S_1-CT separation in DP-TIPS. The limitations of DFT and the small magnitude of the energy differences in question mean that it is difficult to support a more definite statement. The picture is further complicated by the observation that the differences between DP-TIPS and DP-Mes are robust in experiment even though the precise S_1-CT alignment is strongly affected by the solvent environment.

6.4 Conclusions

In this chapter we considered experimental observations of singlet fission in two pentacene dimers in a range of different solvent environments. Furthermore, we employed excited-state DFT with both explicit and implicit solvent models in order to understand the observations from an electronic structure point of view. We find that our calculations show general agreement with experiment in terms of how the electronic states involved in fission are aligned and are influenced by the different solvent environments. However, question remain which are not fully answered by the presented theoretical models. A better understanding may require a combination of techniques from the previous chapter with the ones applied in the present chapter. It appears likely that geometrical relaxation and vibrational dynamics play a crucial role in a satisfactory explanation of the observed differences between DP-Mes and DP-TIPS. This is strongly suggested by the experimental result that fission dynamics in DP-TIPS becomes similar to DP-Mes when the molecules are restricted in their geometrical freedom.

Chapter 7

Concluding remarks

7.1 Summary of findings

In this thesis we employed *ab initio* electronic structure methods to investigate excitations in the molecular crystal and in covalent dimers of pentacene. This was motivated by a desire to gain a better understanding of the singlet fission process in pentacene-derived systems.

Linear-scaling DFT was used to model the influence of the crystal environment on CT configurations in the pentacene crystal. This was combined with a general dipole correction scheme that allowed us to eliminate finite-size effects of the calculations. We found that CT energies are significantly lowered by the response of the crystal environment, bringing them close to the energies of local excitations. This result lends support to the idea that the photoexcited precursor state to fission has significant CT character, and emphasises the role played by CT configurations in fission in the crystal.

We then shifted our attention to molecular dimers of pentacene. We used DFT to parametrise a linear vibronic coupling Hamiltonian of a pentacene dimer, forming the basis for many-body quantum dynamics calculations of the interplay between electronic and vibrational degrees of freedom. This revealed an interesting role for symmetry in fission in such dimers. Due to their high symmetry, couplings that could enable fission are precluded at the ground-state geometry. However, dynamic symmetry breaking by vibrational modes opens up an efficient pathway for fission. We showed that the process proceeds through an avoided crossing of the surfaces corresponding to the photoexcited state and the triplet pair. The coupling between the surfaces is enabled by superexchange via CT states resulting from symmetry breaking.

As a next step we, we performed a systematic comparison of two dimers of pentacene with different side groups. Experimental evidence showed significant differences in how fission

proceeds between the molecules. In one case, explicit CT configurations could be detected in the dynamics, but not in the other case. Rather, the initial bright excitation showed signs of significant CT character. Also, experiments revealed a striking influence of the solvent environment on the rate and yield of fission in both molecules. We attempted to elucidate these observations using DFT calculations in explicit and implicit solvent. The calculations showed that CT can become an energetic trap for fission in highly polar solvents, as is observed. However, we also found that our approach was insufficient to fully account for the observed differences between the molecules. This highlights the limitations of the DFT methods that were employed, as well as of a partial approach that does not include a full treatment of both the electrostatic and vibrational environments.

7.2 Future directions

The are a number of directions for future work that promise to address some of the shortcomings of present approaches.

In order to achieve a more complete and detailed picture of fission, theoretical models must include a comprehensive treatment of both the electrostatics and vibrational effects of the environment. This requires electronic structure methods that are both accurate and scale well to larger system sizes. One significant direction in this context is combining linear-scaling approaches with hybrid functionals [161].

A significant limitation of DFT in the context of modelling fission is its inability to give a satisfactory description of all the relevant electronic states in a unified framework. In this work we tried to address this issue to some extent by combining TDDFT and cDFT. The former is quite good at describing locally-excited states, whereas the latter can be applied successfully to states with charge-transfer character. However, cDFT requires prior knowledge about the state for defining appropriate constraints. Also, this approach is insufficient for excitations of mixed Frenkel and charge-transfer character, which appear important in fission. In addition, it would be desirable to have a more principled method that can deal with multi-excited states like the triplet pair. Methods beyond DFT, like the GW/BSE formalism, may provide a way forward [116, 162]. GW/BSE promises to be able to describe such states states in a unified framework, at still reasonable computational effort compared to high-level quantum chemistry methods like multireference configuration interaction. Another interesting direction are projector-based embedding schemes that make it possible to integrate accurate high-level models of subsystems into large-scale DFT calculations [163].

Finally, there are a number of improvements that could be made to the linear vibronic

coupling model of fission that we presented for a pentacene dimer. As a linear coupling model, it only included couplings to first order in the nuclear displacements. In particular, this means that two-electron couplings that could open up a direct pathway for fission were not included in the model. Adding higher-order terms would address some of these shortcomings, albeit at the expense of increased complexity. Furthermore, the vibrational modes were modelled as harmonic. It seems likely that some of the slower modes leave their harmonic regime during the fission dynamics. Taking account of this would allow more accurate modelling especially at later times, and may shed light on the long-time dynamics which includes the triplet-triplet annihilation observed in some solvents.

Appendix A

Vibronic coupling Hamiltonian

Optimal coupling centroids from clustering analysis (columns ordered as TT, LE^+, LE^-, CT^+, CT^-):

$$\overline{\boldsymbol{W}}_{A_{1,1}} = -\begin{pmatrix} 0 & & & & \\ & 0.45 & & & \\ & & 0.38 & & \\ & & & 0.57 & \\ & & & & 0.57 \end{pmatrix}, \overline{\boldsymbol{W}}_{A_{1,2}} = -\begin{pmatrix} 0.75 & & & & \\ & 0.3 & & & \\ & & 0.29 & & \\ & & & 0.37 & \\ & & & & 0.37 \end{pmatrix},$$

$$\overline{\boldsymbol{W}}_{A_2} = -\begin{pmatrix} 0 & & 1 & & \\ & 0 & & & \\ & & 0 & & \\ 1 & & & 0 & \\ & & & & 0 \end{pmatrix},$$

$$\overline{\boldsymbol{W}}_{B_{1,1}} = -\begin{pmatrix} 0 & & & & 0.63 \\ & 0 & & -0.73 & \\ & & 0 & & 0.26 \\ & -0.73 & & 0 & \\ 0.63 & & 0.26 & & 0 \end{pmatrix},$$

$$\overline{\boldsymbol{W}}_{B_{1,2}} = \begin{pmatrix} 0 & & & & 0.28 \\ & 0 & & -0.33 & \\ & & 0 & & -0.9 \\ & -0.33 & & 0 & \\ 0.28 & & -0.9 & & 0 \end{pmatrix},$$

$$\overline{\boldsymbol{W}}_{B_{2,1}} = -\begin{pmatrix} 0 & & & & \\ & 0 & 0.86 & & \\ & 0.86 & 0 & & \\ & & & 0 & 0.52 \\ & & & 0.52 & 0 \end{pmatrix}, \overline{\boldsymbol{W}}_{B_{2,2}} = \begin{pmatrix} 0 & & & & \\ & 0 & -0.86 & & \\ & -0.86 & 0 & & \\ & & & 0 & 0.52 \\ & & & 0.52 & 0 \end{pmatrix}.$$

Irrep.	ω/cm^{-1}	λ/cm^{-1}	Irrep.	ω/cm^{-1}	λ/cm^{-1}
$A_{1,1}$	903.4	1454.6	$A_{1,2}$	1377.3	4012.6
$B_{1,1}$	450.1	1851.5	$B_{1,2}$	225.4	628.2
$B_{2,1}$	1193.7	1083.9	$B_{2,2}$	1079.4	986.4
A_2	428.0	560.5			

Table A.1: Reaction coordinate frequencies and couplings.

	No.	ω/cm^{-1}	λ/cm^{-1}	No.	ω/cm^{-1}	λ/cm^{-1}
$A_{1,1}$	28	129.8	398.5	40	259.5	198.1
	42	269.2	479.3	60	471.3	-116.9
	82	579.6	-712.3	88	613.7	112.6
	98	706.0	495.3	146	991.7	167.9
	178	1190.0	-175.4	200	1339.6	150.8
	225	1464.6	-270.9	228	1469.2	597.9
	236	1505.6	-326.3	260	1595.6	242.7
	266	1654.6	-282.4	271	1692.1	-338.9
$A_{1,2}$	116	805.2	1094.8	158	1036.0	-552.1
	174	1164.9	536.7	182	1219.4	537.7
	186	1232.4	-850.0	190	1265.1	974.3
	192	1271.4	1010.4	208	1372.5	985.2
	214	1426.0	1217.4	216	1445.3	-1804.3
	256	1579.0	-2285.9			
A_2	24	122.4	-206.8	38	248.0	263.0
	50	302.3	323.4	66	493.3	92.2
	100	726.3	136.2	112	783.1	-111.8
	120	873.7	-53.7	134	937.9	222.4
$B_{1,1}$	35	234.9	-148.4	39	250.6	1137.4
	61	479.2	-1157.9	65	484.9	439.0
	99	720.8	493.0	111	782.7	214.7
	133	921.5	389.9	135	939.6	305.9
$B_{1,2}$	25	122.6	410.0	49	301.7	-475.8
$B_{2,1}$	41	268.2	-373.6	83	587.8	-242.6
	85	596.7	123.1	95	696.9	230.6
	119	828.6	-131.1	159	1036.0	235.1
	173	1140.8	126.3	177	1188.2	144.1
	185	1231.1	141.8	187	1249.5	-440.6
	207	1347.7	-187.2	227	1466.9	213.2
	235	1503.2	155.8	255	1576.6	676.0
$B_{2,2}$	21	108.5	-131.4	33	217.3	-98.9
	51	324.6	94.4	81	572.2	298.5
	91	638.6	174.8	113	797.6	545.7
	181	1218.6	-146.7	191	1270.6	-162.5
	209	1384.4	202.7	215	1435.2	-600.8
	226	1464.7	-163.0	237	1522.9	78.9
	265	1654.1	100.5	272	1692.1	95.7

Table A.2: All modes containing at least 90% of the total coupling.

Bibliography

[1] S.-S. Sun and L. R. Dalton, *Introduction to Organic Electronic and Optoelectronic Materials and Devices*. CRC Press: New York, 2008.

[2] G. J. Hedley, A. Ruseckas, and I. D. W. Samuel, "Light harvesting for organic photovoltaics," *Chemical Reviews*, vol. 117, no. 2, pp. 796–837, 2017. PMID: 27951633.

[3] W. Shockley and H. J. Queisser, "Detailed balance limit of efficiency of p-n junction solar cells," *Journal of Applied Physics*, vol. 32, no. 3, pp. 510–519, 1961.

[4] F. Dimroth, T. N. D. Tibbits, M. Niemeyer, F. Predan, P. Beutel, C. Karcher, E. Oliva, G. Siefer, D. Lackner, P. Fuss-Kailuweit, A. W. Bett, R. Krause, C. Drazek, E. Guiot, J. Wasselin, A. Tauzin, and T. Signamarcheix, "Four-junction wafer-bonded concentrator solar cells," *IEEE Journal of Photovoltaics*, vol. 6, pp. 343–349, Jan 2016.

[5] A. Moyez, A. Dhar, P. Sarkar, H. S. Jung, and S. Roy, *Reviews in Advanced Sciences and Engineering*, vol. 5, ch. A Review of the Multiple Exciton Generation in Photovoltaics, pp. 51–64. Mar 2016.

[6] M. C. Beard, K. P. Knutsen, P. Yu, J. M. Luther, Q. Song, W. K. Metzger, R. J. Ellingson, and A. J. Nozik, "Multiple exciton generation in colloidal silicon nanocrystals," *Nano Letters*, vol. 7, no. 8, pp. 2506–2512, 2007. PMID: 17645368.

[7] M. B. Smith and J. Michl, "Singlet fission," *Chemical Reviews*, vol. 110, pp. 6891–6936, Nov. 2010.

[8] M. B. Smith and J. Michl, "Recent advances in singlet fission," *Annual Review of Physical Chemistry*, vol. 64, no. 1, pp. 361–386, 2013. PMID: 23298243.

[9] C.-K. Skylaris, P. D. Haynes, A. A. Mostofi, and M. C. Payne, "Introducing ONETEP: Linear-scaling density functional simulations on parallel computers," *J. Chem. Phys.*, vol. 122, p. 084119, Feb. 2005.

[10] M. Born and R. Oppenheimer, "Zur Quantentheorie der Molekeln," *Annalen der Physik*, vol. 389, no. 20, pp. 457–484, 1927.

[11] R. Martin, *Electronic Structure: Basic Theory and Practical Methods.* Cambridge University Press, 2008.

[12] P. Hohenberg and W. Kohn, "Inhomogeneous electron gas," *Phys. Rev.*, vol. 136, pp. B864–B871, Nov 1964.

[13] M. Levy, "Universal variational functionals of electron densities, first-order density matrices, and natural spin-orbitals and solution of the v-representability problem," *Proceedings of the National Academy of Sciences*, vol. 76, no. 12, pp. 6062–6065, 1979.

[14] M. Levy, "Electron densities in search of Hamiltonians," *Phys. Rev. A*, vol. 26, pp. 1200–1208, Sep 1982.

[15] E. H. Lieb, "Density functionals for coulomb systems," *International Journal of Quantum Chemistry*, vol. 24, no. 3, pp. 243–277, 1983.

[16] W. Kohn and L. J. Sham, "Self-consistent equations including exchange and correlation effects," *Phys. Rev.*, vol. 140, pp. A1133–A1138, Nov 1965.

[17] D. M. Ceperley and B. J. Alder, "Ground state of the electron gas by a stochastic method," *Phys. Rev. Lett.*, vol. 45, pp. 566–569, Aug 1980.

[18] R. O. Jones and O. Gunnarsson, "The density functional formalism, its applications and prospects," *Rev. Mod. Phys.*, vol. 61, pp. 689–746, Jul 1989.

[19] F. Herman, J. P. Van Dyke, and I. B. Ortenburger, "Improved statistical exchange approximation for inhomogeneous many-electron systems," *Phys. Rev. Lett.*, vol. 22, pp. 807–811, Apr 1969.

[20] P. S. Svendsen and U. von Barth, "Gradient expansion of the exchange energy from second-order density response theory," *Phys. Rev. B*, vol. 54, pp. 17402–17413, Dec 1996.

[21] J. P. Perdew, K. Burke, and M. Ernzerhof, "Generalized gradient approximation made simple," *Phys. Rev. Lett.*, vol. 77, pp. 3865–3868, Oct 1996.

[22] A. D. Becke, "Density-functional exchange-energy approximation with correct asymptotic behavior," *Phys. Rev. A*, vol. 38, pp. 3098–3100, Sep 1988.

[23] C. Lee, W. Yang, and R. G. Parr, "Development of the colle-salvetti correlation-energy formula into a functional of the electron density," *Phys. Rev. B*, vol. 37, pp. 785–789, Jan 1988.

[24] A. D. Becke, "Density-functional thermochemistry. III. The role of exact exchange," *The Journal of Chemical Physics*, vol. 98, no. 7, pp. 5648–5652, 1993.

[25] Y. Tawada, T. Tsuneda, S. Yanagisawa, T. Yanai, and K. Hirao, "A long-range-corrected time-dependent density functional theory," *J. Chem. Phys.*, vol. 120, pp. 8425–8433, May 2004.

[26] J. P. Perdew, R. G. Parr, M. Levy, and J. L. Balduz, "Density-functional theory for fractional particle number: Derivative discontinuities of the energy," *Phys. Rev. Lett.*, vol. 49, pp. 1691–1694, Dec 1982.

[27] E. Runge and E. K. U. Gross, "Density-functional theory for time-dependent systems," *Phys. Rev. Lett.*, vol. 52, pp. 997–1000, Mar 1984.

[28] M. Marques, N. Maitra, F. Nogueira, E. Gross, and A. Rubio, *Fundamentals of Time-Dependent Density Functional Theory*. Lecture Notes in Physics, Springer Berlin Heidelberg, 2012.

[29] Y. Li and C. A. Ullrich, "Time-dependent v-representability on lattice systems," *The Journal of Chemical Physics*, vol. 129, no. 4, pp. –, 2008.

[30] R. van Leeuwen, "Mapping from densities to potentials in time-dependent density-functional theory," *Phys. Rev. Lett.*, vol. 82, pp. 3863–3866, May 1999.

[31] M. Casida and M. Huix-Rotllant, "Progress in time-dependent density-functional theory," *Annual Review of Physical Chemistry*, vol. 63, no. 1, pp. 287–323, 2012. PMID: 22242728.

[32] G. Onida, L. Reining, and A. Rubio, "Electronic excitations: density-functional versus many-body Green's-function approaches," *Reviews of Modern Physics*, vol. 74, pp. 601–659, June 2002.

[33] M. E. Casida, "Time-dependent density functional response theory for molecules," *Recent advances in density functional methods*, vol. 1, p. 155, 1995.

[34] S. Hirata and M. Head-Gordon, "Time-dependent density functional theory within the Tamm-Dancoff approximation," *Chemical Physics Letters*, vol. 314, no. 3-4, pp. 291 – 299, 1999.

[35] A. Dreuw, J. L. Weisman, and M. Head-Gordon, "Long-range charge-transfer excited states in time-dependent density functional theory require non-local exchange," *J. Chem. Phys.*, vol. 119, pp. 2943–2946, Aug. 2003.

[36] A. Dreuw and M. Head-Gordon, "Failure of time-dependent density functional theory for long-range charge-transfer excited states: The zincbacteriochlorin-bacteriochlorin

and bacteriochlorophyll-spheroidene complexes," *Journal of the American Chemical Society*, vol. 126, no. 12, pp. 4007–4016, 2004. PMID: 15038755.

[37] B. G. Levine, C. Ko, J. Quenneville, and T. J. Martinez, "Conical intersections and double excitations in time-dependent density functional theory," *Molecular Physics*, vol. 104, no. 5-7, pp. 1039–1051, 2006.

[38] P. Romaniello, D. Sangalli, J. A. Berger, F. Sottile, L. G. Molinari, L. Reining, and G. Onida, "Double excitations in finite systems," *The Journal of Chemical Physics*, vol. 130, no. 4, pp. –, 2009.

[39] C.-K. Skylaris, P. D. Haynes, A. A. Mostofi, and M. C. Payne, "Introducing ONETEP: Linear-scaling density functional simulations on parallel computers," *The Journal of Chemical Physics*, vol. 122, no. 8, pp. –, 2005.

[40] C.-K. Skylaris, P. D. Haynes, A. A. Mostofi, and M. C. Payne, "Recent progress in linear-scaling density functional calculations with plane waves and pseudopotentials: the ONETEP code," *Journal of Physics: Condensed Matter*, vol. 20, no. 6, p. 064209, 2008.

[41] W. Kohn, "Analytic properties of Bloch waves and Wannier functions," *Phys. Rev.*, vol. 115, pp. 809–821, Aug 1959.

[42] J. D. Cloizeaux, "Energy bands and projection operators in a crystal: Analytic and asymptotic properties," *Phys. Rev.*, vol. 135, pp. A685–A697, Aug 1964.

[43] S. Ismail-Beigi and T. A. Arias, "Locality of the density matrix in metals, semiconductors, and insulators," *Phys. Rev. Lett.*, vol. 82, pp. 2127–2130, Mar 1999.

[44] C.-K. Skylaris, A. A. Mostofi, P. D. Haynes, O. Diéguez, and M. C. Payne, "Nonorthogonal generalized wannier function pseudopotential plane-wave method," *Phys. Rev. B*, vol. 66, p. 035119, Jul 2002.

[45] X.-P. Li, R. W. Nunes, and D. Vanderbilt, "Density-matrix electronic-structure method with linear system-size scaling," *Phys. Rev. B*, vol. 47, pp. 10891–10894, Apr 1993.

[46] P. D. Haynes and M. C. Payne, "Corrected penalty-functional method for linear-scaling calculations within density-functional theory," *Phys. Rev. B*, vol. 59, pp. 12173–12176, May 1999.

[47] P. D. Haynes, C.-K. Skylaris, A. A. Mostofi, and M. C. Payne, "Density kernel optimization in the ONETEP code," *Journal of Physics: Condensed Matter*, vol. 20, no. 29, p. 294207, 2008.

[48] C.-K. Skylaris, A. A. Mostofi, P. D. Haynes, C. J. Pickard, and M. C. Payne, "Accurate kinetic energy evaluation in electronic structure calculations with localized functions on real space grids," *Computer Physics Communications*, vol. 140, no. 3, pp. 315 – 322, 2001.

[49] T. J. Zuehlsdorff, N. D. M. Hine, J. S. Spencer, N. M. Harrison, D. J. Riley, and P. D. Haynes, "Linear-scaling time-dependent density-functional theory in the linear response formalism," *J. Chem. Phys.*, vol. 139, p. 064104, Aug. 2013.

[50] L. E. Ratcliff, N. D. M. Hine, and P. D. Haynes, "Calculating optical absorption spectra for large systems using linear-scaling density functional theory," *Physical Review B*, vol. 84, p. 165131, Oct. 2011.

[51] C. Yam, S. Yokojima, and G. Chen, "Linear-scaling time-dependent density-functional theory," *Phys. Rev. B*, vol. 68, p. 153105, Oct 2003.

[52] G. Chen and S. Mukamel, "Nonlinear polarizabilities of donor-acceptor substituted conjugated polyenes," *The Journal of Physical Chemistry*, vol. 100, no. 26, pp. 11080–11085, 1996.

[53] D. D. O'Regan, M. C. Payne, and A. A. Mostofi, "Subspace representations in ab initio methods for strongly correlated systems," *Physical Review B*, vol. 83, p. 245124, June 2011.

[54] M. Pope and C. Swenberg, *Electronic processes in organic crystals and polymers*. Monographs on the physics and chemistry of materials, Oxford University Press, 1999.

[55] E. C. Greyson, B. R. Stepp, X. Chen, A. F. Schwerin, I. Paci, M. B. Smith, A. Akdag, J. C. Johnson, A. J. Nozik, J. Michl, and M. A. Ratner, "Singlet exciton fission for solar cell applications: Energy aspects of interchromophore coupling," *The Journal of Physical Chemistry B*, vol. 114, pp. 14223–14232, Nov. 2010.

[56] J. Lee, P. Jadhav, P. D. Reusswig, S. R. Yost, N. J. Thompson, D. N. Congreve, E. Hontz, T. Van Voorhis, and M. A. Baldo, "Singlet exciton fission photovoltaics," *Accounts of Chemical Research*, vol. 46, pp. 1300–1311, June 2013.

[57] D. N. Congreve, J. Lee, N. J. Thompson, E. Hontz, S. R. Yost, P. D. Reusswig, M. E. Bahlke, S. Reineke, T. V. Voorhis, and M. A. Baldo, "External quantum efficiency above 100% in a singlet-exciton-fission-based organic photovoltaic cell," *Science*, vol. 340, pp. 334–337, Apr. 2013. PMID: 23599489.

[58] A. Rao, P. C. Y. Chow, S. Gelinas, C. W. Schlenker, C.-Z. Li, H.-L. Yip, A. K.-Y. Jen, D. S. Ginger, and R. H. Friend, "The role of spin in the kinetic control of recombination in organic photovoltaics," *Nature*, vol. advance online publication, Aug. 2013.

[59] S. R. Yost, E. Hontz, S. Yeganeh, and T. Van Voorhis, "Triplet vs singlet energy transfer in organic semiconductors: The tortoise and the hare," *The Journal of Physical Chemistry C*, vol. 116, no. 33, pp. 17369–17377, 2012.

[60] S. Sharifzadeh, A. Biller, L. Kronik, and J. B. Neaton, "Quasiparticle and optical spectroscopy of the organic semiconductors pentacene and PTCDA from first principles," *Physical Review B*, vol. 85, p. 125307, Mar. 2012.

[61] C. C. Mattheus, A. B. Dros, J. Baas, A. Meetsma, J. L. d. Boer, and T. T. M. Palstra, "Polymorphism in pentacene," *Acta Crystallographica Section C Crystal Structure Communications*, vol. 57, pp. 939–941, Aug. 2001.

[62] M. W. B. Wilson, A. Rao, J. Clark, R. S. S. Kumar, D. Brida, G. Cerullo, and R. H. Friend, "Ultrafast dynamics of exciton fission in polycrystalline pentacene," *Journal of the American Chemical Society*, vol. 133, pp. 11830–11833, Aug. 2011.

[63] W.-L. Chan, M. Ligges, A. Jailaubekov, L. Kaake, L. Miaja-Avila, and X.-Y. Zhu, "Observing the multiexciton state in singlet fission and ensuing ultrafast multielectron transfer," *Science*, vol. 334, pp. 1541–1545, Dec. 2011. PMID: 22174249.

[64] L. Sebastian, G. Weiser, and H. Bässler, "Charge transfer transitions in solid tetracene and pentacene studied by electroabsorption," *Chemical Physics*, vol. 61, pp. 125–135, Oct. 1981.

[65] K. Lee and T. Gan, "Influence of substrate temperature on the optical properties of evaporated films of pentacene," *Chemical Physics Letters*, vol. 51, no. 1, pp. 120 – 124, 1977.

[66] J. Burgos, M. Pope, C. E. Swenberg, and R. R. Alfano, "Heterofission in pentacene-doped tetracene single crystals," *physica status solidi (b)*, vol. 83, no. 1, pp. 249–256, 1977.

[67] O. Ostroverkhova, D. G. Cooke, S. Shcherbyna, R. F. Egerton, F. A. Hegmann, R. R. Tykwinski, and J. E. Anthony, "Bandlike transport in pentacene and functionalized pentacene thin films revealed by subpicosecond transient photoconductivity measurements," *Phys. Rev. B*, vol. 71, p. 035204, Jan 2005.

[68] J. C. Johnson, T. H. Reilly, A. C. Kanarr, and J. van de Lagemaat, "The ultrafast photophysics of pentacene coupled to surface plasmon active nanohole films," *The Journal of Physical Chemistry C*, vol. 113, no. 16, pp. 6871–6877, 2009.

[69] M. Grobosch, R. Schuster, T. Pichler, M. Knupfer, and H. Berger, "Analysis of the anisotropy of excitons in pentacene single crystals using reflectivity measurements and electron energy-loss spectroscopy," *Phys. Rev. B*, vol. 74, p. 155202, Oct 2006.

[70] R. Schuster, M. Knupfer, and H. Berger, "Exciton band structure of pentacene molecular solids: Breakdown of the Frenkel exciton model," *Physical Review Letters*, vol. 98, p. 037402, Jan. 2007.

[71] D. Qi, H. Su, M. Bastjan, O. D. Jurchescu, T. M. Palstra, A. T. S. Wee, M. Rübhausen, and A. Rusydi, "Observation of Frenkel and charge transfer excitons in pentacene single crystals using spectroscopic generalized ellipsometry," *Applied Physics Letters*, vol. 103, p. 113303, Sept. 2013.

[72] M. L. Tiago, J. E. Northrup, and S. G. Louie, "Ab initio calculation of the electronic and optical properties of solid pentacene," *Physical Review B*, vol. 67, p. 115212, Mar. 2003.

[73] P. Cudazzo, M. Gatti, and A. Rubio, "Excitons in molecular crystals from first-principles many-body perturbation theory: Picene versus pentacene," *Physical Review B*, vol. 86, p. 195307, Nov. 2012.

[74] H. Marciniak, M. Fiebig, M. Huth, S. Schiefer, B. Nickel, F. Selmaier, and S. Lochbrunner, "Ultrafast exciton relaxation in microcrystalline pentacene films," *Physical Review Letters*, vol. 99, p. 176402, Oct. 2007.

[75] H. Marciniak, I. Pugliesi, B. Nickel, and S. Lochbrunner, "Ultrafast singlet and triplet dynamics in microcrystalline pentacene films," *Physical Review B*, vol. 79, p. 235318, June 2009.

[76] T. S. Kuhlman, J. Kongsted, K. V. Mikkelsen, K. B. Moller, and T. I. Solling, "Interpretation of the ultrafast photoinduced processes in pentacene thin films," *Journal of the American Chemical Society*, vol. 132, pp. 3431–3439, Mar. 2010.

[77] P. M. Zimmerman, Z. Zhang, and C. B. Musgrave, "Singlet fission in pentacene through multi-exciton quantum states," *Nature Chemistry*, vol. 2, pp. 648–652, Aug. 2010.

[78] P. M. Zimmerman, F. Bell, D. Casanova, and M. Head-Gordon, "Mechanism for singlet fission in pentacene and tetracene: From single exciton to two triplets," *Journal of the American Chemical Society*, vol. 133, pp. 19944–19952, Dec. 2011.

[79] T. C. Berkelbach, M. S. Hybertsen, and D. R. Reichman, "Microscopic theory of singlet exciton fission. II. Application to pentacene dimers and the role of superexchange," *The Journal of Chemical Physics*, vol. 138, p. 114103, Mar. 2013.

[80] W.-L. Chan, T. C. Berkelbach, M. R. Provorse, N. R. Monahan, J. R. Tritsch, M. S. Hybertsen, D. R. Reichman, J. Gao, and X.-Y. Zhu, "The quantum coherent mechanism for singlet fission: Experiment and theory," *Accounts of Chemical Research*, vol. 46, pp. 1321–1329, June 2013.

[81] T. C. Berkelbach, M. S. Hybertsen, and D. R. Reichman, "Microscopic theory of singlet exciton fission. I. General formulation," *The Journal of Chemical Physics*, vol. 138, p. 114102, Mar. 2013.

[82] S. R. Yost, J. Lee, M. W. B. Wilson, T. Wu, D. P. McMahon, R. R. Parkhurst, N. J. Thompson, D. N. Congreve, A. Rao, K. Johnson, M. Y. Sfeir, M. G. Bawendi, T. M. Swager, R. H. Friend, M. A. Baldo, and T. Van Voorhis, "A transferable model for singlet-fission kinetics," *Nature Chemistry*, vol. 6, pp. 492–497, June 2014.

[83] E. C. Greyson, J. Vura-Weis, J. Michl, and M. A. Ratner, "Maximizing Singlet Fission in Organic Dimers: Theoretical Investigation of Triplet Yield in the Regime of Localized Excitation and Fast Coherent Electron Transfer," *J. Phys. Chem. B*, vol. 114, pp. 14168–14177, Nov. 2010.

[84] A. A. Bakulin, S. E. Morgan, T. B. Kehoe, M. W. B. Wilson, A. W. Chin, D. Zigmantas, D. Egorova, and A. Rao, "Real-time observation of multiexcitonic states in ultrafast singlet fission using coherent 2d electronic spectroscopy," *Nature Chemistry*, vol. 8, pp. 16–23, Jan. 2016.

[85] K. Miyata, Y. Kurashige, K. Watanabe, T. Sugimoto, S. Takahashi, S. Tanaka, J. Takeya, T. Yanai, and Y. Matsumoto, "Coherent singlet fission activated by symmetry breaking," *Nat Chem*, vol. 9, pp. 983–989, Oct 2017.

[86] S. N. Sanders, E. Kumarasamy, A. B. Pun, M. T. Trinh, B. Choi, J. Xia, E. J. Taffet, J. Z. Low, J. R. Miller, X. Roy, X.-Y. Zhu, M. L. Steigerwald, M. Y. Sfeir, and L. M. Campos, "Quantitative intramolecular singlet fission in bipentacenes," *Journal of the American Chemical Society*, vol. 137, no. 28, pp. 8965–8972, 2015. PMID: 26102432.

[87] J. Zirzlmeier, D. Lehnherr, P. B. Coto, E. T. Chernick, R. Casillas, B. S. Basel, M. Thoss, R. R. Tykwinski, and D. M. Guldi, "Singlet fission in pentacene dimers," *Proceedings of the National Academy of Sciences*, vol. 112, no. 17, pp. 5325–5330, 2015.

[88] S. Lukman, A. J. Musser, K. Chen, S. Athanasopoulos, C. K. Yong, Z. Zeng, Q. Ye, C. Chi, J. M. Hodgkiss, J. Wu, R. H. Friend, and N. C. Greenham, "Tuneable singlet exciton fission and triplet–triplet annihilation in an orthogonal pentacene dimer," *Advanced Functional Materials*, vol. 25, no. 34, pp. 5452–5461, 2015.

[89] S. Lukman, K. Chen, J. M. Hodgkiss, D. H. P. Turban, N. D. M. Hine, S. Dong, J. Wu, N. C. Greenham, and A. J. Musser, "Tuning the role of charge-transfer states in intramolecular singlet exciton fission through side-group engineering," *Nat. Commun.*, vol. 7, pp. 13622 EP –, Dec 2016. Article.

[90] G. B. Piland and C. J. Bardeen, "How morphology affects singlet fission in crystalline tetracene," *The Journal of Physical Chemistry Letters*, vol. 6, no. 10, pp. 1841–1846, 2015. PMID: 26263258.

[91] T. C. Berkelbach, M. S. Hybertsen, and D. R. Reichman, "Microscopic theory of singlet exciton fission. III. Crystalline pentacene," *J. Chem. Phys.*, vol. 141, p. 074705, Aug. 2014.

[92] L. Sebastian, G. Weiser, G. Peter, and H. Bässler, "Charge-transfer transitions in crystalline anthracene and their role in photoconductivity," *Chem. Phys.*, vol. 75, pp. 103–114, Feb. 1983.

[93] P. H. Dederichs, S. Blügel, R. Zeller, and H. Akai, "Ground States of Constrained Systems: Application to Cerium Impurities," *Phys. Rev. Lett.*, vol. 53, pp. 2512–2515, Dec. 1984.

[94] Q. Wu and T. Van Voorhis, "Direct optimization method to study constrained systems within density-functional theory," *Phys. Rev. A*, vol. 72, p. 024502, Aug. 2005.

[95] Q. Wu and T. Van Voorhis, "Constrained Density Functional Theory and Its Application in Long-Range Electron Transfer," *J. Chem. Theory*, vol. 2, pp. 765–774, May 2006.

[96] B. Kaduk, T. Kowalczyk, and T. Van Voorhis, "Constrained Density Functional Theory," *Chem. Rev.*, vol. 112, pp. 321–370, Jan. 2012.

[97] J. Řezáč and A. de la Lande, "Robust, Basis-Set Independent Method for the Evaluation of Charge-Transfer Energy in Noncovalent Complexes," *J. Chem. Theory*, vol. 11, pp. 528–537, Feb. 2015.

[98] V. Vaissier, J. M. Frost, P. R. F. Barnes, and J. Nelson, "Influence of Intermolecular Interactions on the Reorganization Energy of Charge Transfer between Surface-Attached Dye Molecules," *J. Phys. Chem. C*, vol. 119, pp. 24337–24341, Oct. 2015.

[99] S. Zheng, H. Phillips, E. Geva, and B. D. Dunietz, "Ab Initio Study of the Emissive Charge-Transfer States of Solvated Chromophore-Functionalized Silsesquioxanes," *J. Am. Chem. Soc.*, vol. 134, pp. 6944–6947, Apr. 2012.

[100] S. Zheng, E. Geva, and B. D. Dunietz, "Solvated Charge Transfer States of Functionalized Anthracene and Tetracyanoethylene Dimers: A Computational Study Based on a Range Separated Hybrid Functional and Charge Constrained Self-Consistent Field with Switching Gaussian Polarized Continuum Models," *J. Chem. Theory*, vol. 9, pp. 1125–1131, Feb. 2013.

[101] A. Kubas, F. Hoffmann, A. Heck, H. Oberhofer, M. Elstner, and J. Blumberger, "Electronic couplings for molecular charge transfer: Benchmarking CDFT, FODFT, and FODFTB against high-level ab initio calculations," *J. Chem. Phys.*, vol. 140, p. 104105, Mar. 2014.

[102] A. Kubas, F. Gajdos, A. Heck, H. Oberhofer, M. Elstner, and J. Blumberger, "Electronic couplings for molecular charge transfer: benchmarking CDFT, FODFT and FODFTB against high-level ab initio calculations. II," *Phys. Chem. Chem. Phys.*, vol. 17, pp. 14342–14354, May 2015.

[103] Y. Si, W. Liang, and Y. Zhao, "Theoretical Prediction of Triplet-Triplet Energy Transfer Rates in a Benzophenone-Fluorene-Naphthalene System," *J. Phys. Chem. C*, vol. 116, pp. 12499–12507, June 2012.

[104] K. Aikawa, M. Sumita, Y. Shimodo, and K. Morihashi, "Theoretical studies of molecular orientation and charge recombination in poly-paraphenylenevinylene light-emitting diodes," *Phys. Chem. Chem. Phys.*, vol. 17, pp. 20923–20931, Aug. 2015.

[105] T. J. Eisenmayer, J. A. Lasave, A. Monti, H. J. M. de Groot, and F. Buda, "Proton Displacements Coupled to Primary Electron Transfer in the Rhodobacter sphaeroides Reaction Center," *J. Phys. Chem. B*, vol. 117, pp. 11162–11168, Sept. 2013.

[106] J. Yu, D. M. Huang, J. G. Shapter, and A. D. Abell, "Electrochemical and Computational Studies on Intramolecular Dissociative Electron Transfer in β-Peptides," *J. Phys. Chem. C*, vol. 116, pp. 26608–26617, Dec. 2012.

[107] K. R. Siefermann, C. D. Pemmaraju, S. Neppl, A. Shavorskiy, A. A. Cordones, J. Vura-Weis, D. S. Slaughter, F. P. Sturm, F. Weise, H. Bluhm, M. L. Strader, H. Cho, M.-F. Lin, C. Bacellar, C. Khurmi, J. Guo, G. Coslovich, J. S. Robinson, R. A. Kaindl, R. W. Schoenlein, A. Belkacem, D. M. Neumark, S. R. Leone, D. Nordlund, H. Ogasawara, O. Krupin, J. J. Turner, W. F. Schlotter, M. R. Holmes, M. Messerschmidt, M. P. Minitti, S. Gul, J. Z. Zhang, N. Huse, D. Prendergast, and O. Gessner, "Atomic-Scale

Perspective of Ultrafast Charge Transfer at a Dye-Semiconductor Interface," *J. Phys. Chem. Letters*, vol. 5, pp. 2753–2759, Aug. 2014.

[108] J. Řezáč, B. Lévy, I. Demachy, and A. de la Lande, "Robust and Efficient Constrained DFT Molecular Dynamics Approach for Biochemical Modeling," *J. Chem. Theory*, vol. 8, pp. 418–427, Feb. 2012.

[109] H. Oberhofer and J. Blumberger, "Charge constrained density functional molecular dynamics for simulation of condensed phase electron transfer reactions," *J. Chem. Phys.*, vol. 131, p. 064101, Aug. 2009.

[110] S. R. Forrest, "The path to ubiquitous and low-cost organic electronic appliances on plastic," *Nature*, vol. 428, pp. 911–918, Apr. 2004.

[111] Y. Zhao, Y. Guo, and Y. Liu, "25th Anniversary Article: Recent Advances in n-Type and Ambipolar Organic Field-Effect Transistors," *Adv. Mater.*, vol. 25, pp. 5372–5391, Oct. 2013.

[112] W. J. M. Naber, S. Faez, and W. G. v. d. Wiel, "Organic spintronics," *J. Phys. D*, vol. 40, no. 12, p. R205, 2007.

[113] L. E. Ratcliff, L. Grisanti, L. Genovese, T. Deutsch, T. Neumann, D. Danilov, W. Wenzel, D. Beljonne, and J. Cornil, "Toward Fast and Accurate Evaluation of Charge On-Site Energies and Transfer Integrals in Supramolecular Architectures Using Linear Constrained Density Functional Theory (CDFT)-Based Methods," *J. Chem. Theory*, vol. 11, pp. 2077–2086, May 2015.

[114] L. E. Ratcliff, L. Genovese, S. Mohr, and T. Deutsch, "Fragment approach to constrained density functional theory calculations using Daubechies wavelets," *J. Chem. Phys.*, vol. 142, p. 234105, June 2015.

[115] S. Baroni, S. de Gironcoli, A. Dal Corso, and P. Giannozzi, "Phonons and related crystal properties from density-functional perturbation theory," *Rev. Mod. Phys.*, vol. 73, pp. 515–562, Jul 2001.

[116] P. B. Coto, S. Sharifzadeh, J. B. Neaton, and M. Thoss, "Low-Lying Electronic Excited States of Pentacene Oligomers: A Comparative Electronic Structure Study in the Context of Singlet Fission," *J. Chem. Theory*, vol. 11, no. 1, pp. 147–156, 2014.

[117] D. D. O'Regan, N. D. M. Hine, M. C. Payne, and A. A. Mostofi, "Projector self-consistent DFT+U using nonorthogonal generalized Wannier functions," *Phys. Rev. B*, vol. 82, p. 081102, Aug. 2010.

[118] E. Artacho and L. Miláns del Bosch, "Nonorthogonal basis sets in quantum mechanics: Representations and second quantization," *Phys. Rev. A*, vol. 43, p. 5770, 1991.

[119] D. D. O'Regan, N. D. M. Hine, M. C. Payne, and A. A. Mostofi, "Linear-scaling DFT+U with full local orbital optimization," *Phys. Rev. B*, vol. 85, p. 085107, Feb. 2012.

[120] T. Ozaki, "Efficient recursion method for inverting an overlap matrix," *Phys. Rev. B*, vol. 64, p. 195110, Oct 2001.

[121] A. Ruiz-Serrano, N. D. M. Hine, and C.-K. Skylaris, "Pulay forces from localized orbitals optimized in situ using a psinc basis set," *J. Chem. Phys.*, vol. 136, p. 234101, June 2012.

[122] S. J. Clark, M. D. Segall, C. J. Pickard, P. J. Hasnip, M. I. J. Probert, K. Refson, and M. C. Payne, "First principles methods using CASTEP," *Z. Kristallogr.*, vol. 220, no. 5/6, pp. 567–570, 2005.

[123] R. B. Campbell, J. M. Robertson, and J. Trotter, "The crystal structure of hexacene, and a revision of the crystallographic data for tetracene," *Acta Crystallogr.*, vol. 15, pp. 289–290, Mar. 1962.

[124] N. D. M. Hine, J. Dziedzic, P. D. Haynes, and C.-K. Skylaris, "Electrostatic interactions in finite systems treated with periodic boundary conditions: Application to linear-scaling density functional theory," *J. Chem. Phys.*, vol. 135, p. 204103, Nov. 2011.

[125] G. Makov and M. C. Payne, "Periodic boundary conditions in ab initio calculations," *Phys. Rev. B*, vol. 51, pp. 4014–4022, Feb. 1995.

[126] M. Leslie and N. J. Gillan, "The energy and elastic dipole tensor of defects in ionic crystals calculated by the supercell method," *J. Phys. C: Solid State Phys.*, vol. 18, no. 5, p. 973, 1985.

[127] K. P. McKenna and J. Blumberger, "Crossover from incoherent to coherent electron tunneling between defects in mgo," *Phys. Rev. B*, vol. 86, p. 245110, Dec 2012.

[128] J. Blumberger and K. P. McKenna, "Constrained density functional theory applied to electron tunnelling between defects in mgo," *Phys. Chem. Chem. Phys.*, vol. 15, pp. 2184–2196, 2013.

[129] S. T. Murphy and N. D. M. Hine, "Anisotropic charge screening and supercell size convergence of defect formation energies," *Phys. Rev. B*, vol. 87, p. 094111, Mar 2013.

[130] L. N. Kantorovich, "Elimination of the long-range dipole interaction in calculations with periodic boundary conditions," *Phys. Rev. B*, vol. 60, pp. 15476–15479, Dec. 1999.

[131] H. Lee and W. Cai, "Ewald summation for coulomb interactions in a periodic supercell," Jan 2009.

[132] G. Fischerauer, "Comments on real-space Green's function of an isolated point-charge in an unbounded anisotropic medium," *IEEE Trans. Ultrason, Ferroelect., Freq. Control*, vol. 44, pp. 1179–1180, Nov. 1997.

[133] G. Lever, D. J. Cole, N. D. M. Hine, P. D. Haynes, and M. C. Payne, "Electrostatic considerations affecting the calculated HOMO-LUMO gap in protein molecules," *J. Phys. Condens. Matter*, vol. 25, no. 15, p. 152101, 2013.

[134] S. Sharifzadeh, P. Darancet, L. Kronik, and J. B. Neaton, "Low-energy charge-transfer excitons in organic solids from first-principles: The case of pentacene," *The Journal of Physical Chemistry Letters*, vol. 4, pp. 2197–2201, July 2013.

[135] M. Valiev, E. J. Bylaska, N. Govind, K. Kowalski, T. P. Straatsma, H. J. J. V. Dam, D. Wang, J. Nieplocha, E. Apra, T. L. Windus, and W. A. de Jong, "NWChem: A comprehensive and scalable open-source solution for large scale molecular simulations," *Computer Physics Communications*, vol. 181, no. 9, pp. 1477–1489, 2010.

[136] B. M. Wong and T. H. Hsieh, "Optoelectronic and Excitonic Properties of Oligoacenes: Substantial Improvements from Range-Separated Time-Dependent Density Functional Theory," *J. Chem. Theory*, vol. 6, pp. 3704–3712, Dec. 2010.

[137] G. A. Worth and L. S. Cederbaum, "BEYOND BORN-OPPENHEIMER: Molecular Dynamics Through a Conical Intersection," *Annual Review of Physical Chemistry*, vol. 55, pp. 127–158, jun 2004.

[138] D. Arthur and S. Vassilvitskii, "K-Means++: the Advantages of Careful Seeding," in *Proceedings of the Eighteenth Annual ACM-SIAM Symposium on Discrete Algorithms*, SODA '07, (Philadelphia, PA, USA), pp. 1027–1025, Society for Industrial and Applied Mathematics, 2007.

[139] A. W. Chin, J. Prior, R. Rosenbach, F. Caycedo-Soler, S. F. Huelga, and M. B. Plenio, "The role of non-equilibrium vibrational structures in electronic coherence and recoherence in pigment-protein complexes," *Nature Physics*, vol. 9, no. 2, pp. 113–118, 2013.

[140] J. Prior, A. W. Chin, S. F. Huelga, and M. B. Plenio, "Efficient Simulation of Strong System-Environment Interactions," *Physical Review Letters*, vol. 105, p. 050404, jul 2010.

[141] F. A. Y. N. Schröder and A. W. Chin, "Simulating open quantum dynamics with time-dependent variational matrix product states: Towards microscopic correlation of environment dynamics and reduced system evolution," *Physical Review B*, vol. 93, p. 075105, feb 2016.

[142] Y.-Y. Shi, L.-M. Duan, and G. Vidal, "Classical simulation of quantum many-body systems with a tree tensor network," *Physical Review A*, vol. 74, p. 022320, aug 2006.

[143] S. Szalay, M. Pfeffer, V. Murg, G. Barcza, F. Verstraete, R. Schneider, and Ö. Legeza, "Tensor product methods and entanglement optimization for ab initio quantum chemistry," *International Journal of Quantum Chemistry*, vol. 115, pp. 1342–1391, oct 2015.

[144] F. Verstraete, J. J. García-Ripoll, and J. I. Cirac, "Matrix Product Density Operators: Simulation of Finite-Temperature and Dissipative Systems," *Physical Review Letters*, vol. 93, p. 207204, nov 2004.

[145] U. Schollwöck, "The density-matrix renormalization group in the age of matrix product states," *Annals of Physics*, vol. 326, pp. 96–192, jan 2011.

[146] G. Vidal, "Entanglement Renormalization," *Physical Review Letters*, vol. 99, p. 220405, nov 2007.

[147] G. Evenbly and G. Vidal, "Algorithms for entanglement renormalization," *Physical Review B*, vol. 79, p. 144108, apr 2009.

[148] J. Haegeman, C. Lubich, I. Oseledets, B. Vandereycken, and F. Verstraete, "Unifying time evolution and optimization with matrix product states," *Physical Review B*, vol. 94, p. 165116, oct 2016.

[149] A. J. Musser, M. Al-Hashimi, M. Maiuri, D. Brida, M. Heeney, G. Cerullo, R. H. Friend, and J. Clark, "Activated singlet exciton fission in a semiconducting polymer," *Journal of the American Chemical Society*, vol. 135, no. 34, pp. 12747–12754, 2013. PMID: 23883167.

[150] A. Petrozza, F. Laquai, I. A. Howard, J.-S. Kim, and R. H. Friend, "Dielectric switching of the nature of excited singlet state in a donor-acceptor-type polyfluorene copolymer," *Phys. Rev. B*, vol. 81, p. 205421, May 2010.

[151] T. J. Zuehlsdorff, P. D. Haynes, F. Hanke, M. C. Payne, and N. D. M. Hine, "Solvent effects on electronic excitations of an organic chromophore," *Journal of Chemical Theory and Computation*, vol. 12, no. 4, pp. 1853–1861, 2016. PMID: 26967019.

[152] T. J. Zuehlsdorff, P. D. Haynes, M. C. Payne, and N. D. M. Hine, "Predicting solvatochromic shifts and colours of a solvated organic dye: The example of nile red," *The Journal of Chemical Physics*, vol. 146, no. 12, p. 124504, 2017.

[153] University of California, San Francisco, *Amber 14*, 2014.

[154] R. J. Loncharich, B. R. Brooks, and R. W. Pastor, "Langevin dynamics of peptides: The frictional dependence of isomerization rates of n-acetylalanyl-n'-methylamide," *Biopolymers*, vol. 32, no. 5, pp. 523–535, 1992.

[155] T. J. Zuehlsdorff, N. D. M. Hine, M. C. Payne, and P. D. Haynes, "Linear-scaling time-dependent density-functional theory beyond the tamm-dancoff approximation: Obtaining efficiency and accuracy with in situ optimised local orbitals," *The Journal of Chemical Physics*, vol. 143, no. 20, p. 204107, 2015.

[156] T. J. Zuehlsdorff and C. M. Isborn, "Combining the Ensemble and Franck-Condon Approaches for Spectral Shapes of Molecules in Solution," *arXiv:1709.07490*.

[157] S. Grimme and M. Parac, "Substantial Errors from Time-Dependent Density Functional Theory for the Calculation of Excited States of Large pi Systems," *ChemPhysChem*, vol. 4, pp. 292–295, Mar. 2003.

[158] A. Klamt and G. Schuurmann, "Cosmo: A new approach to dielectric screening in solvents with explicit expressions for the screening energy and its gradient," *Journal of the Chemical Society, Perkin Transactions 2*, no. 5, pp. 799–805, 1993.

[159] Q. Wu, B. Kaduk, and T. V. Voorhis, "Constrained density functional theory based configuration interaction improves the prediction of reaction barrier heights," *The Journal of Chemical Physics*, vol. 130, p. 034109, Jan. 2009.

[160] J. M. G. Barthel and R. Buchner, "High frequency permittivity and its use in the investigation of solution properties," *Pure and Applied Chemistry*, vol. 63, no. 10, pp. 1473–1482, 2009.

[161] J. Dziedzic, Q. Hill, and C.-K. Skylaris, "Linear-scaling calculation of hartree-fock exchange energy with non-orthogonal generalised wannier functions," vol. 139, p. 214103, 12 2013.

[162] S. Refaely-Abramson, F. H. da Jornada, S. G. Louie, and J. B. Neaton, "Origins of singlet fission in solid pentacene from an ab initio green's-function approach," 06 2017.

[163] S. J. Bennie, M. W. van der Kamp, R. C. R. Pennifold, M. Stella, F. R. Manby, and A. J. Mulholland, "A projector-embedding approach for multiscale coupled-cluster calculations applied to citrate synthase," *Journal of Chemical Theory and Computation*, vol. 12, no. 6, pp. 2689–2697, 2016. PMID: 27159381.

Acknowledgements

I would like to express my very warm and sincere thanks to the following people who contributed crucially to the successful completion of this thesis:

- My supervisor Nicholas Hine for being so generous with his time, knowledge and expertise, as well as being understanding and supportive in difficult times.
- Alex Chin, who stepped into the official supervisor role when Nick left for a position at Warwick. I am particularly grateful for his enthusiastic support of my career development.
- My partner Fiorenza and my family for their unrelenting support and encouragement.
- Joseph Nelson and James Hamp, who shared an office with me. We did not only share the office but also many lunches, coffees and interesting conversations.
- Florian Schröder, Steven Lukman and Andrew Musser for fruitful collaboration.
- All the students and staff members of TCM, past and present, for creating a very positive and stimulating atmosphere. A special thanks goes to Michael Rutter for his very competent technical support.
- My funding bodies, the Winton Programme for the Physics of Sustainability and the Engineering and Physical Sciences Research Council.